



Fakultät für Physik

Laboratorium für Applikationen der Synchrotronstrahlung

Time-resolved studies of the micro-bunching instability at KARA

Zur Erlangung des akademischen Grades eines
DOKTORS DER NATURWISSENSCHAFTEN

von der KIT-Fakultät für Physik des
Karlsruher Instituts für Technologie (KIT)

genehmigte
DISSERTATION

von

Dipl.-Phys. Benjamin Kehrer
aus Rottweil

Datum der mündlichen Prüfung: 19.07.2019

Referent: Prof. Dr. Anke-Susanne Müller
Korreferent: Prof. Dr. Marc Weber

Gewidmet all' jenen,
die mich auf diesem Weg begleitet
und mir ein Lächeln geschenkt haben.

*Dedicated to all those
who joined me on this way
and gave me a smile.*

Contents

1. Introduction	9
2. Accelerator physics	13
2.1. Storage rings	13
2.2. Ultra-relativistic approximation	13
2.3. Synchrotron radiation	14
2.3.1. Incoherent synchrotron radiation	14
2.3.2. Coherent synchrotron radiation	15
2.4. Optics and beam dynamics	16
2.4.1. Transverse beam dynamics	17
2.4.2. Longitudinal beam dynamics	21
2.5. Radiation damping	23
2.6. Energy spread	24
2.7. Horizontal bunch size	25
3. KARA	27
3.1. Accelerator chain	27
3.2. Short-bunch operation mode	30
3.3. The visible light diagnostics port	30
4. Interaction of the bunch with its environment	33
4.1. Wake fields and impedances	33
4.1.1. Resistive wall	34
4.1.2. CSR impedances	35
4.2. Impedance effects	38
4.2.1. Synchronous phase shift	38
4.2.2. Incoherent synchrotron frequency shift	40
4.3. Potential well distortion	41
4.4. Micro-bunching instability	42
4.5. Bursting threshold	45

5. Optical diagnostics	47
5.1. Time-correlated single photon counting	47
5.1.1. Experimental setup	47
5.1.2. Dead-time correction	49
5.1.3. Data analysis	52
5.2. Fast-gated intensified camera	58
5.2.1. Experimental setup	58
5.2.2. From the energy spread to the spot size	61
5.2.3. Data analysis	62
5.3. Turn-by-turn horizontal bunch size measurements	68
5.3.1. Experimental setup	68
5.3.2. Data analysis	69
6. Synchronisation of the FGC setup	75
6.1. Overview	75
6.2. FGC setup hardware delays	76
6.3. Hardware synchronisation scheme	78
6.4. Calibration of the synchronisation	78
7. Modeling the short-bunch mode accelerator optics	81
7.1. The AT model	81
7.2. LOCO fits	82
7.3. Tracking studies	83
7.3.1. Imaging the transverse bunch profile	85
7.3.2. Diffusion blow-up	87
7.4. Benchmarking the AT model	90
8. Potential for studies of horizontal bunch size and arrival time	93
8.1. Synchronous studies of energy spread and CSR	93
8.1.1. Bursting behaviour of energy spread and CSR	94
8.1.2. Onset of a CSR burst	96
8.1.3. Turn-by-turn studies of the bursting behaviour	98
8.2. Radiation damping and bursting frequency	102
8.3. Impedance studies	107
8.3.1. Incoherent synchrotron frequency shift	107
8.3.2. Synchronous phase shift	110
8.4. Short bunch-length bursting	115
8.5. Outlook	116
9. Summary	117

Acronyms	122
Bibliography	131
Acknowledgements	133
A. Appendix	137
A.1. Time-correlated single photon counting	137
A.1.1. Dead time determination	137
A.1.2. Estimation of the SPAD dead time effects	139
A.2. Fast-gated camera: control and readout	140
A.3. Streak camera: data analysis	142

1. Introduction

One of the basic principles of physics is the fact that an electric charge is radiating when it is exposed to an acceleration. This is intensively used in dedicated accelerators where this radiation was observed the first time in 1947 [1]. As this observation took place at a synchrotron, this radiation is called *synchrotron radiation*. Synchrotron radiation offers some unique features like a high brilliance and a broad spectrum. Depending on the particle energy, its spectrum ranges from infrared up to hard X-rays. By pushing the energy of the accelerated particles to higher values, the frequency of the emitted radiation increases as well. As the wavelength is decreasing hereby, this allows e.g. structural analysis in unprecedented detail as the achievable resolution is defined by the radiation wavelength.

Since 1968 synchrotron radiation is used as scientific tool, when the first dedicated storage ring for synchrotron radiation experiments (Tantalus I [2]) was built. In the following, the number of these light sources increased rapidly, a development that is still on-going with new synchrotron light sources being built around the world.

Already in the early time of accelerator physics, first predictions were made concerning the coherence of this radiation: For wavelengths above the length of the emitting structure, the radiation from the single particles interfere constructively leading to a strong increase of the emitted radiation power [3]. The bunches in a synchrotron typically have a length in the range of tens of picoseconds, this coherent radiation would be in the Gigahertz range. The drawback hereby is the fact that the vacuum pipe, the particles are moving in, damps or even suppresses the transmission of this radiation.

When the bunches are longitudinally compressed strong enough, the emission of this coherent synchrotron radiation (CSR) is pushed into the Terahertz range and is no longer damped due to shielding effects. In parallel to this short-bunch operation, several accelerators reported on an unstable behaviour of the bunches during the emission of CSR (e.g. NSLS VUV [4], SURF II [5], ALS [6], BESSY-II [7], [8], Diamond [9], SOLEIL [10]). This behaviour is due to the formation of sub-structures on the bunch that occur when the bunch starts to interact with its previously emitted CSR in a bent section of the storage ring [11, 12]. As the CSR self-interaction of the bunch can lead to quick changes in the amplitude of these sub-structures, the radiation is often emitted in short and intense bursts. Thus, this instability is referred to as *micro-bunching instability* with a *bursting* behaviour of the bunch.

The energy spread of the particles inside a bunch is a very important parameter to describe and analyse the micro-bunching instability. In the past, energy spread studies have been done based on measurements as well as simulations. Measurements of the energy spread at the SLC damping ring showed that the energy spread is constant below the bursting threshold and starts to increase for bunch currents above [13]. In addition, measurements at the Synchrotron Ultraviolet Radiation Facility (SURF III) showed that the energy spread and the radiation are modulated with the same period length [14]. In this case, the energy spread was accessed via pinhole measurements of the horizontal beam size in a dispersive section. It is noteworthy that both measurements were not time-resolved. Time-resolved measurements of the horizontal bunch size during the micro-bunching instability at SPEAR3 showed a sawtooth-like modulation of the energy spread [15, Fig. 6]. There, a fast-gated intensified camera (FGC) was used. At such a camera, an image intensifier is mounted in front of the sensor. It can be switched on and off within a very short time resulting in the illumination of just a single bunch. Using this *gating* function, the camera acts as a pulse picker which allows single-turn images of the bunch. This principle is used at different accelerators since many years (e.g. SLC damping ring [16], KEK-B [17]).

Numerical simulations of the longitudinal phase space showed, that the bunch size (given by the bunch length) and the bursting CSR emission have the same modulation period length [18].

One step further towards a better understanding of the dynamics of an electron bunch during the micro-bunching instability are *time-resolved* measurements of the different bunch parameters. Time-resolved means that the different parameters can be measured on a single-turn basis, in the ideal case also turn-by-turn or even bunch-by-bunch. Hereby, the relevant time scales are defined by the accelerator and its radio frequency (RF) systems. In the case of the Karlsruhe research accelerator (KARA), where the experimental studies of this thesis have been done, the bunch spacing is 2 ns and the revolution time is 368 ns. This sets stringent requirements as for bunch-by-bunch measurements a time range of only 2 ns can be used for the detection, readout, digitizing and data storage. Thus, the detector systems must be sufficiently sensitive and fast enough to fulfill these requirements.

One feasible way for energy spread studies is the investigation of the horizontal bunch size as it is coupled to the energy spread in dispersive sections of an accelerator. Ideally, the horizontal bunch size should be measured for every turn and for a sufficiently long time (at least for several milliseconds) to resolve the bursting characteristics. At KARA, this would require a camera with a frame rate of at least 2.7 MHz. This is very difficult to achieve and thus those cameras are still not commercially available. To overcome this limitation, an FGC can be used. In order to cover more than only one turn per image a fast rotating mirror is mounted in front of the camera. This mirror sweeps the

incoming light over the entrance aperture of the camera. During this sweep, the gate is opened and closed several times. Thus, many single turn images of the bunch are placed beside each other on the camera sensor before it is read out. This technique was first used at PEP-II [19], later also at SPEAR3 [20].

Within the framework of this thesis, such an FGC setup was successfully installed at KARA. It allows time-resolved energy spread studies with a single-turn resolution. The system is embedded into a hardware synchronisation system that enables the simultaneous detection of different bunch parameters. To determine the horizontal bunch size from the FGC images, a dedicated data analysis scheme was developed, which takes the particularities of the imaging process into account, as the bunch is moving in the same plane as its size is intended to be measured. As the micro-bunching instability is a bunch-current dependent effect, a precise measurement of the filling pattern is required. This is achieved by using the principle of time-correlated single photon counting (TCSPC), the corresponding setup was upgraded concerning the resolution and the reduction of dead-time induced distortions. An additional important aspect for accelerator studies is a proper representation of the accelerator in simulation programs. Within the scope of this thesis, the Accelerator Toolbox for MATLAB (AT) has been used to model the accelerator and study beam dynamics in the short-bunch mode.

This thesis is structured in the following way: In Chapter 2, a brief introduction into accelerator physics is given, while in Chapter 3, KARA and the visible light diagnostics (VLD) port are presented. Chapter 4 introduces and discusses different aspects of the (self-)interaction of the bunch with its environment, including the micro-bunching instability. The experimental setups using visible light are presented in Chapter 5. These setups are embedded into a synchronisation scheme, which is introduced in Chapter 6. In Chapter 7, the accelerator simulation studies using AT are discussed. The setups and data analysis framework allow time-resolved experimental studies of the bunch arrival time and during the micro-bunching instability, those are discussed in Chapter 8. As further detector developments are very promising and first tests already show their potential, an outlook is given in Chapter 8.5, before the thesis is summarized in Chapter 9.

2. Accelerator physics

This chapter introduces the basics of accelerator physics, with focus on the relevant aspects for the topics covered by this thesis. First, storage rings are introduced followed by the incoherent and coherent synchrotron radiation. The fundamentals of the transverse as well as the longitudinal beam dynamics are presented. As the emission of synchrotron radiation leads to damping effects and the formation of an equilibrium energy spread, both topics are discussed.

2.1. Storage rings

Storage rings are particle accelerators that are able to keep a particle beam at constant energy in their ultra-high vacuum beam pipe for a long time (several hours). Besides their use for particle collision experiments, they are used as synchrotron radiation sources. This radiation is emitted when highly-relativistic charged particles (usually electrons) are deflected. It has some unique features like a high intensity and a broad spectrum ranging from infrared (IR) up to hard X-rays. If the electron bunches are shortened by changing some accelerator parameters, the emission in the THz range can become coherent.

2.2. Ultra-relativistic approximation

The accelerated particles in the context of this thesis are always electrons. They have a rest mass of $m_0 = 511 \text{ keV}/c^2$ [21]. The energy-momentum relation

$$E = \sqrt{E_{\text{kin}}^2 + E_0^2} = \sqrt{p^2 c^2 + m_0^2 c^4} \quad (2.1)$$

relates the total energy E to the kinetic energy E_{kin} and the rest energy E_0 . For kinetic energies far above 511 keV this leads to $E_0 \ll E_{\text{kin}}$ and thus

$$E \approx pc \quad (2.2)$$

which is used in the following.

2.3. Synchrotron radiation

The acceleration of a charged particle leads to the emission of electro-magnetic radiation. In storage rings that are specially designed as light sources, this effect is exploited to produce synchrotron radiation used for various experiments. This radiation is either emitted in the dipole magnets or in the so called insertion devices, where the beam is exposed to a sequence of short dipole fields that let it oscillate and thus radiate stronger. The synchrotron radiation has some unique features that makes it an important tool for material science and also for diagnostic purposes. Synchrotron radiation has a continuous spectrum (from IR up to hard X-rays) and is also emitted collimated.

2.3.1. Incoherent synchrotron radiation

For a transverse deflection of a relativistic particle in a dipole field, the total emitted power P_0 can be calculated to [22, Eq. (2.15)]:

$$P_0 = \frac{e^2 c}{6\pi\epsilon_0} \frac{1}{(m_0 c^2)^4} \frac{E^4}{R^2} \quad (2.3)$$

with E as its energy and R as the bending radius in the magnet. ϵ_0 is the vacuum permittivity which is $8.85 \cdot 10^{-12} \frac{\text{A s}}{\text{V m}}$ [23].

Two facts are particularly important:

1. The power scales with $1/m_0^4$, so electrons are preferred over heavier particles like e.g. protons.
2. The power scales with $\frac{E^4}{R^2}$, so already a small increase of the energy leads to a strong increase of the radiated power and is (usually) easier to achieve than reducing the bending radius R .

The energy loss per turn U_0 for a single particle can be determined by integrating the radiation power from Eq. (2.3) along the bent section of one turn:

$$U_0 = \oint P_0 dt = P_0 \frac{2\pi R}{c} = \frac{e^2}{3\epsilon_0} \frac{1}{(m_0 c^2)^4} \frac{E^4}{R}. \quad (2.4)$$

For electrons, this leads to [22, Eq. (2.19)]

$$U_0[\text{keV}] = 88.5 \frac{E^4[\text{GeV}^4]}{R[\text{m}]}. \quad (2.5)$$

In the rest frame of the particles, the emission is the one of a Hertz dipole, while in the lab frame – after applying a Lorentz transformation – the photons are emitted into a cone with an opening angle Θ that can be approximated by [22, Eq. (2.23)]:

$$\tan \Theta \approx \frac{1}{\gamma}, \quad (2.6)$$

with γ as relativistic gamma factor.

As γ is large for highly relativistic particles, Θ is small and one can set $\tan \Theta \approx \Theta$. For a stationary observer the light pulse of a single electron in the far-field has the length [22, Eq. (2.25)]

$$\Delta t \approx \frac{4R}{3c\gamma^3} \quad (2.7)$$

with R as bending radius. For highly relativistic electrons ($\gamma \geq 10^3$) and a bending radius of typically some meters (for KARA $R = 5.559$ m), the light pulses have a length of several attoseconds (10^{-18} s).

The temporal profile of the synchrotron radiation pulse of an electron bunch is the convolution of the longitudinal bunch profile with the single electron pulse. As the single electron pulse is very short compared to the electron bunch length, it can be assumed to be a delta pulse and thus the intensity profile of the synchrotron radiation pulse perfectly represents the profile of the electron bunch. This fact is the base for different techniques of non-invasive beam diagnostics based on detecting the incoherent synchrotron radiation.

2.3.2. Coherent synchrotron radiation

For an electron bunch coherent amplification of the emitted synchrotron radiation can occur. The starting point for that is the radiation field \mathcal{E}_j of a single electron j within a bunch at a frequency ω [24, Sec. 24.7]

$$\mathcal{E}_j \propto e^{i(\omega t + \phi_j)}. \quad (2.8)$$

The phase ϕ_j describes the position of this electron relative to the bunch center. The total radiation power is given by the square of the radiation field for all electrons:

$$P(\omega) \propto \sum_{j,l}^N \mathcal{E}_j \mathcal{E}_l^* \propto N + \sum_{j \neq l}^N e^{i(\phi_j - \phi_l)}. \quad (2.9)$$

This finally leads to

$$P(\omega) = p_0(\omega) N (1 + (N-1)\mathcal{F}) \approx p_0(\omega) \cdot \left(\underbrace{N}_{\text{incoherent}} + \underbrace{N^2 \mathcal{F}}_{\text{coherent}} \right) \quad (2.10)$$

with the single electron radiation power $p_0(\omega)$ and the so-called form factor \mathcal{F} . The form factor is given by

$$\mathcal{F}(\omega) = \left| \frac{1}{Ne} \int_{-\infty}^{\infty} \rho(t) e^{-i\omega t} dt \right|^2 \quad (2.11)$$

and is the absolute squared of the Fourier transform of the normalized charge distribution. For a Gaussian shaped bunch with length σ_t this leads to

$$\mathcal{F}(\omega) = e^{-(\sigma_t \omega)^2}. \quad (2.12)$$

So for wavelengths above the bunch length, \mathcal{F} becomes close to 1 and due to the square of the number of electrons a strong amplification in radiation power is achieved for this coherent radiation referred to as coherent synchrotron radiation (CSR). To make use of this coherent radiation in an accelerator, the bunch length has to be tuned down to get a coherent emission for wavelength below the cut off wave length, which is given by [18]

$$\lambda_{\text{cut-off}} = 2\sqrt{\frac{h^3}{R}}, \quad (2.13)$$

with the height of the beam pipe h and R as the bending radius. For KARA with a 32 mm high beam pipe and a bending radius of 5.6 m, $\lambda_{\text{cut-off}} = 4.8$ mm.

2.4. Optics and beam dynamics

To reach a stable orbit for an electron beam, magnetic and electrical fields are used. While magnetic fields are used for deflecting the particles, electric fields are used for longitudinal acceleration and to compensate the energy losses due to the emission of synchrotron radiation. The following basic introduction into the terminus and the underlying physics is based on the book of Wille [22].

The usage of electric and magnetic fields for guiding an electron through an accelerator is due to the Lorentz force

$$\vec{F}_L = e \left(\vec{E} + \vec{v} \times \vec{B} \right) \quad (2.14)$$

with \vec{E} as the electric and \vec{B} as the magnetic field acting on an electron with the charge e and the velocity \vec{v} . If \vec{v} is large – as it is the case for relativistic particles in a storage ring with $v \approx c$ – (static) magnetic fields are more suitable for deflecting the particles. In addition, those fields do not change the particle energy due to $\vec{F}_L \perp \vec{B}$. Thus, changing the particle energy is achieved using longitudinal electric fields.

A convenient way to describe ring accelerators is the usage of a co-moving coordinate system. This coordinate system follows the trajectory of a reference particle with the reference energy $E = E_0$. It is illustrated in Figure 2.1.

The reference particle follows the reference path while x , y and z describe the position of the particle with momentum p relative to this *reference* orbit. Together with the corresponding momenta $x' = \frac{dx}{ds}$, $y' = \frac{dy}{ds}$ and $\delta = \frac{E-E_0}{E_0} = \frac{\Delta E}{E_0}$, the six-dimensional phase space of the particles is defined.

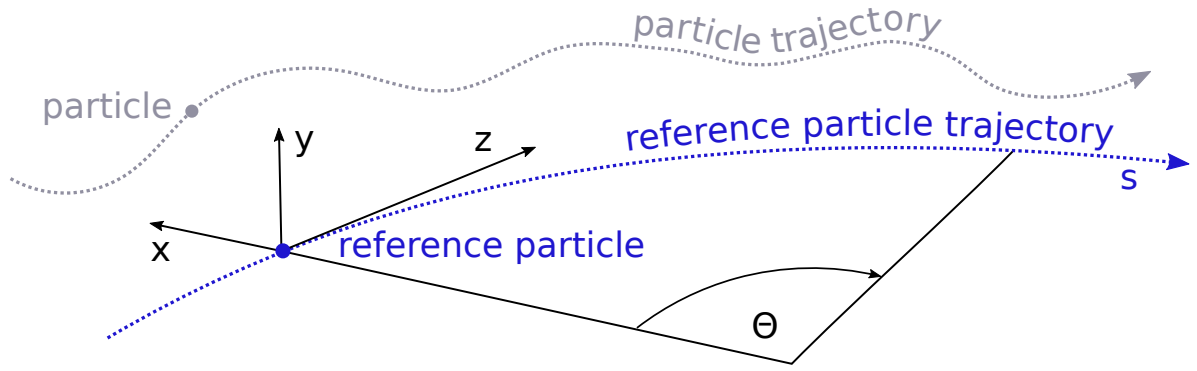


Figure 2.1.: Co-moving coordinate system with the two transverse components x and y , and the longitudinal component z pointing tangentially away from the reference particle trajectory (adapted from [24, Fig. 4.2.]).

2.4.1. Transverse beam dynamics

As magnetic fields are used for deflecting the particles (with charge e and energy E), the equality of Lorentz and centripetal force can be used as starting point for a mathematical description leading to

$$\frac{1}{R(x, y, s)} = \frac{ec}{E} B_y(x, y, s). \quad (2.15)$$

The bending radius R is large compared to the dimensions of the beam and thus a Taylor-expansion of the magnetic field is useful:

$$\begin{aligned} \frac{ec}{E} B_y(x, y, s) &= \frac{ec}{E} \cdot B_{y0} + \frac{ec}{E} \frac{dB_y}{dx} x + \frac{ec}{E} \frac{1}{2!} \frac{d^2 B_y}{dx^2} x^2 + \dots \\ &= \underbrace{\frac{1}{R}}_{\text{Dipole}} + \underbrace{kx}_{\text{Quadrupole}} + \underbrace{\frac{1}{2!} m x^2}_{\text{Sextupole}} + \dots \end{aligned}$$

The different magnetic multipoles are responsible for different effects:

1. Dipole: Bending

To get a circular shaped trajectory, it has to be bent. At KARA, this is achieved using 16 dipole magnets in total.

2. Quadrupole: Focussing

To prevent the electron bunches from becoming too large (the vacuum pipe has a finite size), focussing elements – similar to those used in light optics – are required. To get a focussing, a magnetic field is needed having a strength that increases with the distance from the center. This is achieved using quadrupole magnets, a scheme of such a magnet is shown in Fig. 2.2. It also shows one drawback of these quadrupole magnets: they only focus in one direction, in the other one they lead

to defocussing. To achieve a net focussing, those quadrupole magnets have to be arranged in dedicated patterns.

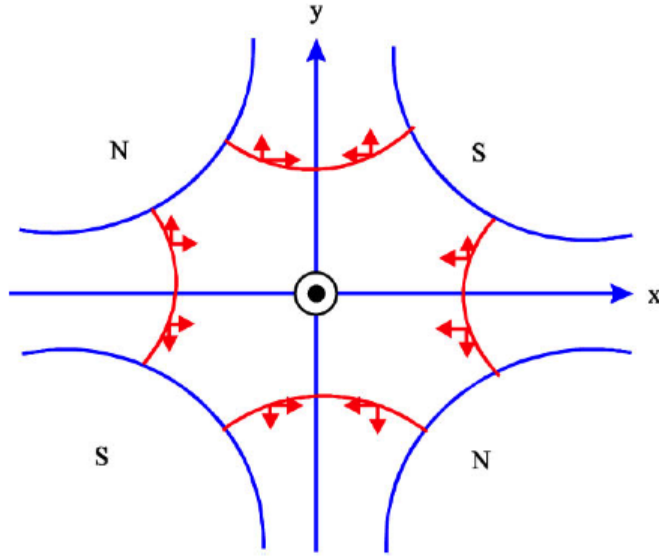


Figure 2.2.: Principle scheme of a quadrupole magnet. The red arrows indicate the forces on the particles, in this example the quadrupole is focussing horizontally while defocussing vertically [25, Fig. 2].

3. Sextupole: Correct chromatic effects

Quadrupole magnets act as lenses for the particle beam. Analogue to light optics, also at these magnetic lenses chromatic effects occur as the focal length of the quadrupole magnets depends on the particle energy. Thus, a finite energy spread leads to a spread of the corresponding focus points. This effect is also called chromaticity and is compensated using sextupole magnets.

Considering only the first two orders and assuming that the horizontal and vertical plane are not coupled, the following equations of motions can be derived with the dipole strength $\frac{1}{R^2(s)}$ and the quadrupole strength $k(s)$ [22, Eq. (3.21)]:

$$x''(s) + \left(\frac{1}{R^2(s)} - k(s) \right) x(s) = \frac{1}{R(s)} \frac{\Delta E}{E_0} \quad (2.16a)$$

$$y''(s) + k(s)y(s) = 0. \quad (2.16b)$$

They can be shortened by neglecting dispersive effects ($\frac{\Delta E}{E_0} = 0$) and one obtains a set of differential equations:

$$u''(s) + K(s)u(s) = 0 \quad K(s) = \begin{cases} \frac{1}{R^2(s)} - k(s) & \text{if } u(s) = x(s) \\ k(x) & \text{if } u(s) = y(s). \end{cases} \quad (2.17)$$

For a solution to these equations, one has to keep in mind the periodic structure of a circular accelerator with an orbit length L_0 . This leads to $K(s + L_0) = K(s)$ and thus a general solution for the equations is

$$u(s) = A(x) \cos(\Psi_u(s) + \phi). \quad (2.18)$$

The amplitude $A(s)$ as well as the phase $\Psi_u(s)$ depend on the longitudinal position s and are periodic with L_0 . The corresponding oscillation is called betatron oscillation with the betatron frequencies f_x and f_y for oscillations in the horizontal and vertical plane, respectively. The amplitude $A(s)$ can be written as

$$A(s) = \sqrt{\epsilon\beta(s)} \quad (2.19)$$

with $\beta(s)$ as the so-called beta function and ϵ as emittance.

To derive the equations of motion, dispersive effects were ignored by setting $\frac{\Delta E}{E}$ to zero. But especially for dipole magnets – used for bending the trajectory to get a closed orbit – this is no longer possible. Going back to equation (2.16b) and defining a special *dispersion orbit* $D(s)$ with $\Delta E/E_0 = 1$ leads to an inhomogeneous differential equation

$$D''(s) + \frac{1}{R^2}D(x) = \frac{1}{R}. \quad (2.20)$$

The solution of such an equation is the sum of the general solution for the homogeneous part ($1/R = 0$) and one particular solution D_p for the inhomogeneous case. The ansatz $D_p = \text{const.}$ eventually leads to the solution for the dispersive case:

$$x(s) = x_{\Delta E/E_0=0}(s) + D(s) \frac{\Delta E}{E_0}. \quad (2.21)$$

Thus, the orbit $x(s)$ is the sum of the orbit of a particle with reference energy ($\Delta E/E_0 = 0$) and the part due to the finite energy deviation. This energy deviation leads to a slightly different bending radius in the dipole magnets. As the horizontal dispersion $D_x(s)$ is usually much larger than the vertical dispersion D_y , the latter one is usually ignored and thus $D(s) = D_x(s)$ is used in the following.

The dispersion function $D(s)$, the beta functions $\beta_x(s)$ and $\beta_y(s)$ are called optics functions. All three are defined by the different magnetic elements of an accelerator. In Fig. 2.3, the beta function as well as the dispersion of KARA are plotted. The symmetry of the lattice is fourfold, with four sectors whereby each sector consists of

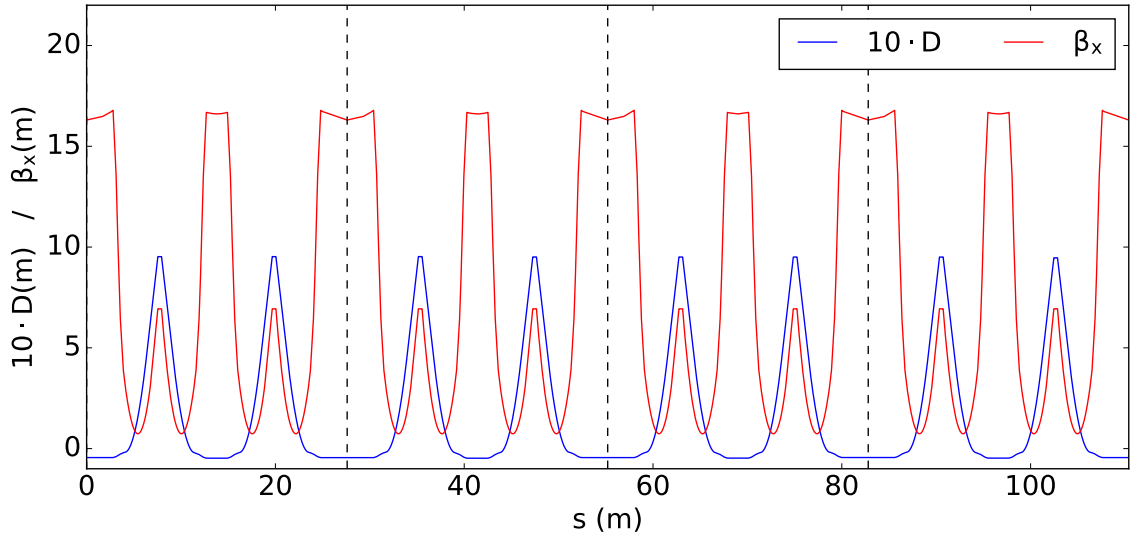


Figure 2.3.: Optics function (horizontal dispersion and beta function) for the KARA storage ring. The dashed lines indicate the fourfold symmetry of the lattice. The curves were calculated using the Accelerator Toolbox for MATLAB (AT) [26]. To enhance the visibility, the dispersion is scaled by a factor of 10 to achieve a similar magnitude as the beta function.

two mirror-symmetric parts. As the typical values of the dispersion are low compared to the ones of the beta functions, it is usual to plot them together and scale the dispersion by a factor of 10.

As the dispersion shifts the orbit in cases of an energy deviation, also the resulting length L of the closed orbit and thus also the revolution time T changes. The so-called *momentum compaction factor* α_c relates this orbit length deviation and the energy deviation:

$$\alpha_c = \frac{\Delta L/L_0}{\Delta E/E_0} \approx \frac{1}{L_0} \oint \frac{D(s)}{R(s)} ds. \quad (2.22)$$

The last equality holds true if only linear optics (dipoles and quadrupoles) are considered. Equation (2.22) states, that the momentum compaction factor α_c depends on the magnet lattice. The momentum compaction factor α_c connects the transverse and the longitudinal motion, therefore the longitudinal beam dynamics are briefly sketched in the following.

2.4.2. Longitudinal beam dynamics

While the transverse motion of the beam is affected by magnetic fields, longitudinal electric fields are used to influence the longitudinal motion. As the particles lose energy due to the emission of synchrotron radiation, this energy loss has to be compensated. Otherwise, the beam will be lost as the particles would travel on orbits with decreasing radius until they hit the inner wall of the beam pipe.

This longitudinal acceleration is achieved in resonators that are called radio frequency (RF) cavities. Fed by microwave emitters (in case of KARA: two klystrons [27, 28]), a standing electromagnetic wave is excited inside the cavities. The geometry of the cavities is designed to achieve a purely electric field in the longitudinal direction at the particle trajectory [24].

The fundamental frequency f_{RF} is mostly defined by the geometry of the cavity, in case of KARA it is 500 MHz ¹.

The energy gain ΔE of an electron with charge e that passes a cavity depends on the peak voltage V_{RF} and the phase ϕ of the electric field:

$$\Delta E = eV_{\text{RF}} \sin \phi. \quad (2.23)$$

The ratio of the RF frequency f_{RF} and the revolution frequency f_0 is referred to as harmonic number h , in case of KARA h is 184.

$$f_{\text{RF}} = h \cdot f_0 \quad (2.24)$$

The harmonic number h gives the number of the buckets of a storage ring, being the stable areas in phase space that can be filled with electrons [22, Sec. 5.7]. Thus, the electrons do not travel arbitrarily distributed (coasting beam), but are grouped into packages called *bunches*.

The sinusoidal shape of the electric fields leads to a longitudinal focusing of the particles called *phase focusing*. Particles with an energy below the reference energy are deflected stronger in the dipole magnets resulting in a shorter orbit. This shorter orbit leads to an earlier arrival in the RF cavity at the next turn. Thus, those particles are exposed to a higher voltage than the reference particle and gain more energy, which results in a slightly longer orbit on the following turn. As a consequence, the particles arrive slightly later the next turn, see Fig. 2.4 for a schematic principle. This holds true if the momentum compaction factor α_c is kept positive, which was the case within the scope of this thesis. As a consequence, the particles oscillate around the synchronous phase ϕ_s . This oscillation is referred to as *synchrotron oscillation*.

¹The frequency is not exactly 500 MHz, but typically around 499.7 MHz. Nevertheless, it is referred to as '500 MHz-RF'.

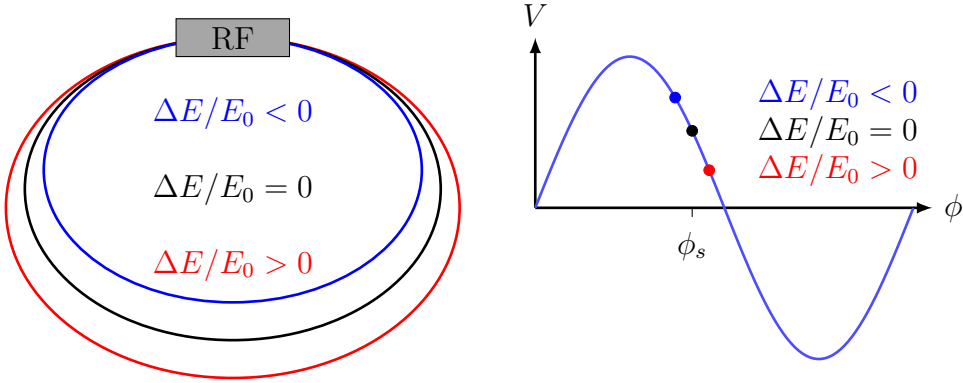


Figure 2.4.: Principle of phase focussing: particles with an energy below the reference energy E_0 (blue curve) have a shorter revolution time, arrive earlier in the cavities and are exposed to a higher voltage. Thus, they get a slightly higher energy gain leading to a slightly longer revolution time (red curve) and vice versa. This results in a longitudinal oscillation of the particle around the stable phase ϕ_s and is known as phase focussing.

The following introduction is based on [29, pp. 146 ff.]. For this analytical description, a particle inside a bunch is considered. Due to synchrotron radiation, it loses a certain amount of energy per turn U . Depending on its arrival time τ relative to the synchronous particle at t_s , it gains or loses the energy amount ΔE :

$$\Delta E = eV_{\text{RF}} \sin(2\pi f_{\text{RF}}(t_s + \tau)) - U. \quad (2.25)$$

With the synchronous phase $\phi_s = 2\pi f_{\text{RF}} t_s$ and assuming $\tau \ll T_0$ with T_0 as revolution time, the sinusoidal part can be simplified:

$$\Delta E = eV_{\text{RF}} \sin(\phi_s) + \frac{2\pi h V_{\text{RF}} \cos(\phi_s)}{T_0} \tau - U. \quad (2.26)$$

As the energy gain per turn is usually very small, one can set $\Delta \dot{E} = \frac{\Delta E}{T_0}$ and thus

$$\Delta \dot{E} = \frac{eV_{\text{RF}} \sin(\phi_s)}{T_0} + \frac{2\pi h e V_{\text{RF}} \cos(\phi_s)}{T_0^2} \tau - \frac{1}{T_0} U. \quad (2.27)$$

Expanding the energy loss as a function of ΔE and τ as

$$U(\Delta E, \tau) \approx U_0 + \frac{dU}{dE} \Delta E + \frac{dU}{dt} \tau \quad (2.28)$$

leads to

$$\Delta \dot{E} = \frac{eV_{\text{RF}} \sin(\phi_s)}{T_0} + \frac{2\pi h e V_{\text{RF}} \cos(\phi_s)}{T_0^2} \tau - \frac{1}{T_0} U_0 - \frac{1}{T_0} \frac{dU}{dE} \Delta E - \frac{1}{T_0} \frac{dU}{dt} \tau. \quad (2.29)$$

With the condition for the synchronous particle $U_0 = eV_{\text{RF}} \sin(\phi_s)$, this leads to

$$\Delta \dot{E} = \frac{2\pi h e V_{\text{RF}} \cos(\phi_s)}{T_0^2} \tau - \frac{1}{T_0} \frac{dU}{dE} \Delta E - \frac{1}{T_0} \frac{dU}{dt} \tau. \quad (2.30)$$

Using $\dot{\tau} = \frac{\tau}{T_0} = \alpha_c \Delta E / E_0$ this finally leads to the second order differential equation:

$$\Delta \ddot{E} + \underbrace{\frac{1}{T_0} \frac{dU}{dE}}_{\text{damping}} \Delta \dot{E} - \underbrace{\frac{2\pi h \alpha_c e V_{\text{RF}} \cos(\phi_s)}{T_0^2 E_0}}_{\omega_{s,0}^2 = (2\pi f_s)^2} \Delta E + \underbrace{\frac{\alpha_c}{T_0 E} \frac{dU}{dt}}_{\text{neglected here}} \Delta E = 0. \quad (2.31)$$

This is the differential equation for a damped harmonic oscillator. Initially, the last term is neglected and the *synchrotron* frequency f_s is introduced here with

$$f_s = \frac{1}{T_0} \cdot \sqrt{-\frac{h e V_{\text{RF}} \cos \phi_s}{2\pi E_0}} \alpha_c. \quad (2.32)$$

This frequency depends on the energy of the reference particle E_0 and the momentum compaction factor α_c and thus also on the magnet lattice. Equation (2.32) can also be used to determine the momentum compaction factor α_c from the synchrotron frequency and the RF voltage.

Normally, the number of particles per bunch is in the order of 10^6 and higher. A convenient way to treat this is to describe the particles as an ensemble with the root mean square (RMS) widths $\sigma_x, \sigma_{x'}, \sigma_y, \sigma_{y'}, \sigma_z, \sigma_\delta$. By neglecting interactions between the particles, one can deduce the motion of the center of mass of the distributions directly from the single particle ansatz. For highly relativistic beams (as it is normally the case for electron machines) the bunch length is given by [24, Eq. (9.70) and (9.71)]

$$\sigma_z = \frac{c \sigma_\delta |\alpha_c|}{2\pi f_s} = \frac{c}{\sqrt{2\pi} f_{\text{rev}}} \sqrt{\frac{\alpha_c E_0}{h e V_{\text{RF}}}} \sigma_\delta. \quad (2.33)$$

To decrease the bunch length, the momentum compaction factor α_c should be lowered as the bunch length scales with $\sqrt{\alpha_c}$.

2.5. Radiation damping

The emission of synchrotron radiation is coupled to an energy loss which damps the synchrotron oscillation. In Eq. (2.31), this is contained in the second summand. Together with the synchrotron frequency f_s , this equation can be written as

$$\Delta \ddot{E} + \frac{2}{\tau_z} \Delta \dot{E} + \omega_{s,0}^2 \Delta E = 0 \quad (2.34)$$

with $\omega_{s,0} = 2\pi f_s$. τ_z is the the longitudinal damping time which is defined as

$$\frac{1}{\tau_z} = \frac{1}{2T_0} \frac{dU}{dE}. \quad (2.35)$$

The analytical treatment finally leads to an expression for τ_z (for details, see [22, pp. 211 ff.]):

$$\frac{1}{\tau_z} = \frac{U}{2T_0E} \cdot (2 + \mathcal{D}) \quad (2.36)$$

$$\mathcal{D} = \frac{\oint \left[\frac{D}{R} \left(2k + \frac{1}{R^2} \right) \right] ds}{\oint \frac{ds}{R^2}} \quad (2.37)$$

with U as energy loss per turn calculated according to Eq. (2.5).

The longitudinal damping time is defined by the energy E and the magnet lattice as \mathcal{D} is a function of the dispersion D , the quadrupole strength k and the bending radius R . A similar treatment for the horizontal and vertical plane finally gives the three damping times:

$$\frac{1}{\tau_z} = \frac{U_0}{2T_0E} \cdot (2 + \mathcal{D}) = \frac{U_0}{2T_0E} \cdot J_z \quad (2.38a)$$

$$\frac{1}{\tau_x} = \frac{U_0}{2T_0E} \cdot (1 - \mathcal{D}) = \frac{U_0}{2T_0E} \cdot J_x \quad (2.38b)$$

$$\frac{1}{\tau_y} = \frac{U_0}{2T_0E} = \frac{U_0}{2T_0E} \cdot J_y. \quad (2.38c)$$

The sum of the *damping partition numbers* J_i is – according to the Robinson theorem [30] – equal to 4:

$$J_z + J_x + J_y = 4. \quad (2.39)$$

For storage rings with separated magnets for bending and focussing (as it is the case for KARA), \mathcal{D} is usually very small and thus damping occurs in all three planes with $J_z = 2, J_x = 1, J_y = 1$. While the Robinson theorem states, that the overall radiation damping is constant, the amount of damping can be distributed between the different planes [31].

2.6. Energy spread

The particles of a beam do not all have the same energy as the stochastic emission of photons leads to a spread of their energies. This spread is referred to as *energy spread* and is determined by different processes like damping and quantum excitation due to the emission of synchrotron radiation.

After a certain transient time, the energy spread reaches an equilibrium limit, the so-called *natural energy spread* that can be derived according to [24, Sec. 11.3.1].

A particle with a certain energy deviation ΔE_0 at the time t_0 is undergoing a synchrotron oscillation with the frequency f_s :

$$\Delta E(t) = \Delta E_0 e^{i2\pi f_s(t-t_0)}. \quad (2.40)$$

After the emission of a photon with the energy ϵ_γ at the time t_1 , the oscillation of the energy deviation has changed to

$$\Delta E_1 = \Delta E_0 e^{i\Omega_s(t-t_0)} - \epsilon_\gamma e^{i\Omega_s(t-t_1)}. \quad (2.41)$$

The transition from a single particle to a Gaussian distribution finally leads to an expression for the *natural energy spread* [24, Eq. (11.45)]

$$\delta_0^2 = C_q \frac{\gamma^2 \langle 1/R^3 \rangle}{J_z \langle 1/R^2 \rangle} = C_q \frac{\gamma^2}{J_z R} \quad (2.42)$$

where for the last step an isomagnetic lattice was assumed with all dipole magnets having the same bending radius. The constant C_q

$$C_q = \frac{55}{32\sqrt{3}} \frac{\hbar c}{m_0 c^2}. \quad (2.43)$$

is $3.84 \cdot 10^{-13}$ m for electrons.

Thus, the natural energy spread only depends on the beam energy (via γ) and the bending radius R . For KARA, the natural energy spread for a beam energy of 1.3 GeV is $4.7 \cdot 10^{-4}$.

For the equilibrium case, the energy spread and the bunch length are related by

$$\sigma_{t,0} = \frac{c\alpha_c}{2\pi f_s \beta} \delta_0. \quad (2.44)$$

The bunch length $\sigma_{t,0}$ is referred to as *zero-current* or *natural* bunch length.

2.7. Horizontal bunch size

If a particle beam has a finite energy spread, the effect of the dispersion leads to a change of the bunch size as it is summarized here according to [24, Sec. 11.4.4].

In Eq. (2.19), the oscillation amplitude for the betatron oscillation of a single particle was defined based on the beta function β and the emittance ϵ . This holds for a particle having the same energy as the reference particle. In case of a slight deviation σ_δ from this value, the oscillation amplitude becomes

$$A = \sqrt{\epsilon\beta(s)} + D(s)\sigma_\delta. \quad (2.45)$$

As stated above, this is the case for the horizontal plane as for most storage rings the vertical dispersion can be neglected. Going one step further to a particle distribution, the horizontal RMS beam size at the longitudinal position s along the storage ring is given by

$$\sigma_x(s) = \sqrt{\epsilon_x \cdot \beta_x(s) + (D(s) \cdot \sigma_\delta)^2}. \quad (2.46)$$

Equation (2.46) shows, that the beam size at a certain point is defined by the beta function β_x and the dispersion D , being both lattice parameters as well as the emittance ϵ . This is consequently used to investigate the energy spread as it can be accessed by (time-resolved) measurements of the horizontal bunch size in a dispersive section of a storage ring (Sec. 5.2).

3. KARA

The experimental studies of the micro-bunching instability within the scope of this thesis were done at the Karlsruhe research accelerator (KARA). This chapter briefly introduces the storage ring and its pre-accelerators. Afterwards, the regularly offered short-bunch operation mode is discussed.

3.1. Accelerator chain

The KIT synchrotron KARA is operated as synchrotron light source. The synchrotron radiation is used for different purposes like tomography, diffraction analysis or lithography [32]. Besides the 23 dedicated beam lines for these studies, also diagnostics ports exist, where the incoherent synchrotron radiation is coupled out to serve as diagnostics tool. KARA uses electrons with beam energies up to 2.5 GeV. To achieve this high energy, a chain of pre-accelerators is used. Figure 3.1 shows a picture of the KARA pre-accelerator chain.

1. Electron gun

The KARA electron gun is a thermionic gun accelerating the electrons to an energy of 90 keV [33]. From its working principle, this electron gun allows the injection of single bunches into the accelerator.

2. Racetrack microtron

The next accelerator is the racetrack-microtron. It consists of two dipole magnets deflecting the beam by 180° , with one linear accelerator (Linac) in-between. The electrons pass this Linac ten times until they have the final energy of 53 MeV. As the energy increases from turn to turn, the bending radius inside the two dipoles increases linearly with the energy and thus the trajectory moves towards the outer side of the microtron [34].

3. Booster synchrotron

This is the last of the pre-accelerators. The booster is a synchrotron meaning that the energy and the magnetic field in the dipole magnets is increased synchronously to keep the beam always on the same trajectory. In the booster, the bunches are accelerated up to 500 MeV. One booster cycle, which is the sequence of injection



Figure 3.1.: Overview of the KARA pre-accelerator chain. The electron-gun is located at the right hand side, from there the electrons are transferred to the racetrack-microtron, its two dipole magnets can be seen in the middle. Afterwards, they are transported through the transfer line to the booster synchrotron that spans along the outer walls.

into the booster, energy ramp, extraction and down-ramping of the magnets, lasts for one second.

4. The KARA storage ring

After the bunches have passed the pre-accelerator chain, they are injected into the main storage ring. The layout of the accelerator is illustrated in Fig. 3.2.

For bending the electron beam path 16 dipole magnets are used (yellow), while a focussing is achieved by the 40 quadrupole magnets (red). Those magnets are grouped in five *families*, which means that the magnets of one family are all fed by the same power supply. To correct chromatic effects 24 sextupole magnets are used. They are grouped in two families. The magnetic lattice has a fourfold symmetry as it was also illustrated by the lattice functions D and β_x in Fig. 2.3.

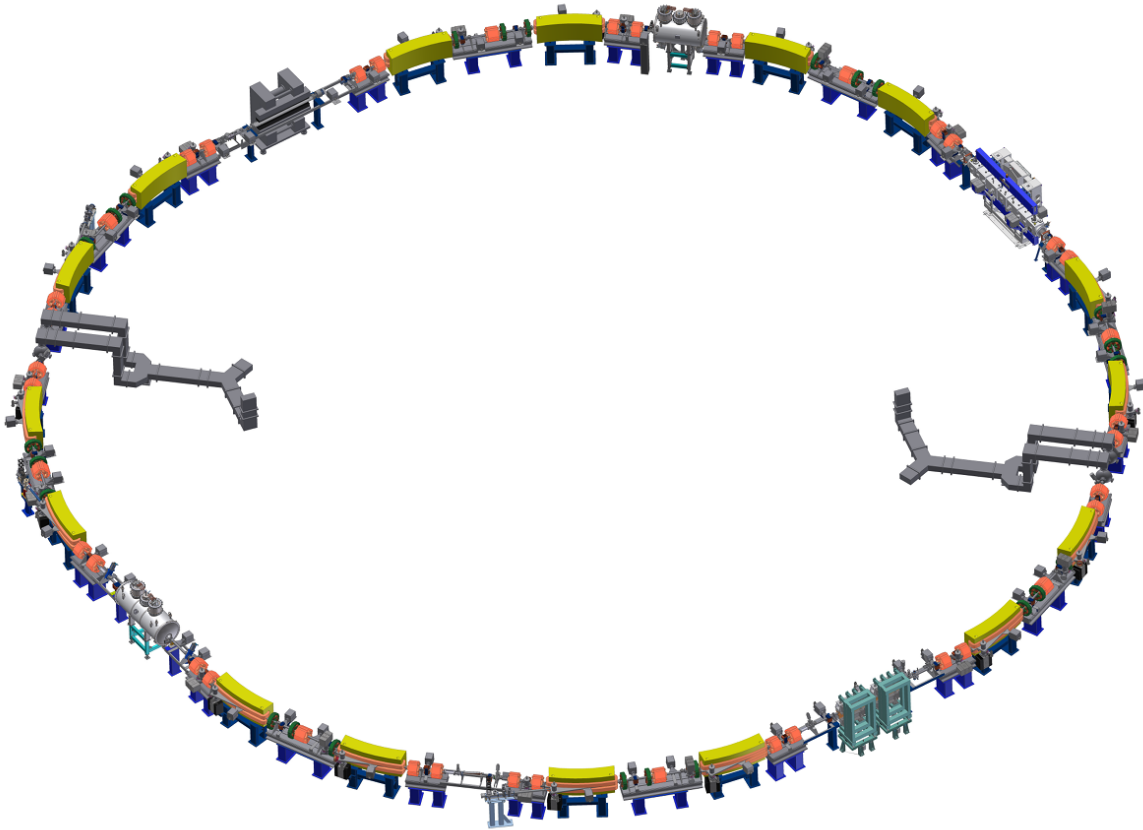


Figure 3.2.: Layout of the KARA storage ring consisting of 16 dipole magnets (yellow) and 40 quadrupole magnets (red). Two of the straight sections contain the radio frequency (RF) cavities. Each cavity pair is waveguide-coupled to a klystron inside of the storage ring (not shown here). The other straight sections are used for insertion devices [35].

Two of the straight sections are used for the RF system and contain two RF cavities each. In these cavities, the electrons are accelerated longitudinally by a standing electro-magnetic wave with a frequency of 500 MHz. The other straight sections are used for the insertion devices. These devices consist of a sequence of short dipole magnets with alternating field orientation. They lead to an oscillatory motion of the electrons and for each bending movement synchrotron radiation is emitted. The individual pulses from each bending superimpose to increase the photon flux [24, Sec. 24.1.4 - 24.1.5].

Some key parameters of the storage ring are listed in Table 3.1.

Table 3.1.: KARA key parameters

Circumference	110.4 m
Beam energy	0.5 GeV to 2.5 GeV
Beam current	up to 200 mA
RF frequency	499.7 MHz
Harmonic number	184
Revolution time	368.2 ns

3.2. Short-bunch operation mode

To study the occurrence of the micro-bunching instability, the bunches have to be compressed longitudinally by reducing the momentum compaction factor α_c [36]. This operation mode is referred to as *short-bunch* or *low- α_c mode* and is offered regularly at KARA. As stated in Eq. (2.22), α_c is given by the integral over the dispersion. To reduce the integral, the dispersion is locally pushed to negative values by changing the currents in the quadrupole magnets [8, 37]. As the bunches are getting shorter, this process is referred to as *squeezing*. This is illustrated in Fig. 3.3, where the horizontal dispersion for one sector of KARA is plotted for different optics.

The blue line corresponds to an optic with a high α_c of $7.7 \cdot 10^{-3}$, while the green and the red one correspond to a reduced α_c . It can be seen that the dispersion has to be stretched in order to reduce α_c (see Eq. (2.22)). It is also noteworthy, that the dispersion at the imaging source point of the VLD port is barely changing during the squeeze. This is shown in detail in Fig. 3.4. As the VLD port (see Sec. 3.3) covers a path length of approximately 0.08 m, the dispersion changes along this trajectory with up to 13 percent. This is illustrated by the grey lines above and below the blue line.

3.3. The visible light diagnostics port

Besides the 23 beam lines used for experiments with synchrotron radiation, also diagnostics ports exist where the synchrotron radiation is used as diagnostics tool for the accelerator. One of these ports is the visible light diagnostics (VLD) port, where the experimental setups described in Chapter 5 are located [38]. The port uses the incoherent synchrotron radiation in the visible wavelength range from the 5° port of a dipole magnet. It was originally designed for longitudinal bunch diagnostics using a streak camera (SC) [39]. Therefore, its optics consists of a set of planar and off-axis paraboloid mirrors. To separate the visible radiation from the X-rays, the first mirror is a cooled

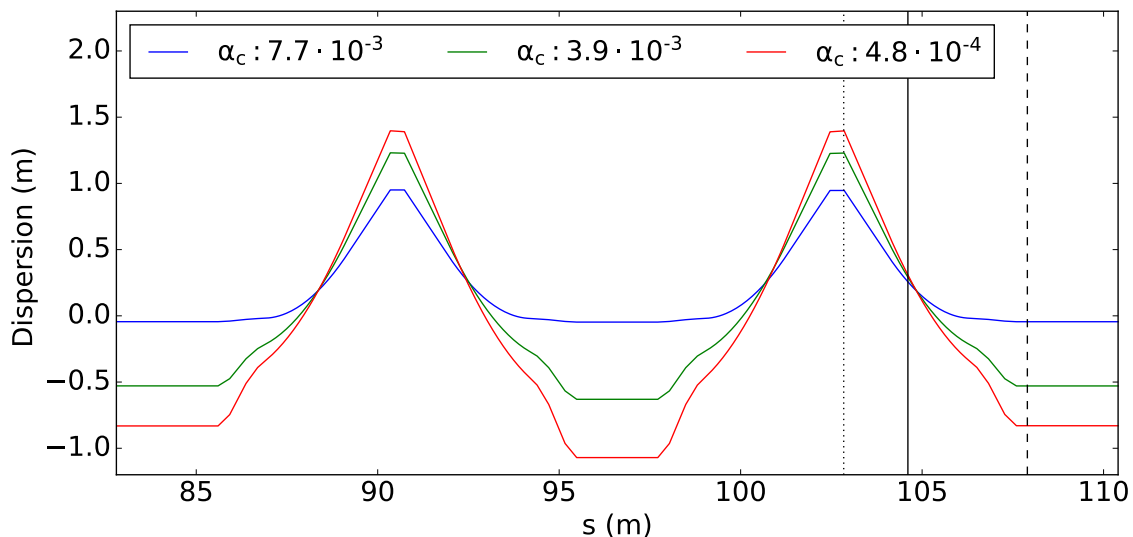


Figure 3.3.: Dispersion for different optics used for reducing the momentum compaction factor α_c calculated by using the Accelerator Toolbox for MATLAB (AT) [26]. The vertical lines depict the position of maximum dispersion (dotted), the visible light diagnostics (VLD) port (solid) and the position of minimum dispersion (dashed).

aluminium mirror with an angle of 45° that absorbs X-rays and reflects the visible light upwards. After it has left the vacuum beam pipe through a quartz window, the light is focussed by the first off-axis paraboloid mirror ($f = 1200$ mm) that also guides the light through the radiation safety wall into the lab.

To allow a simultaneous operation of the different setups, the incoming light is divided into wavelength regions. This is achieved by a set of two shortpass filters as it is illustrated in Fig. 3.5.

The first shortpass filter reflects the light with wavelengths above 400 nm. The wavelengths below are transmitted and sent to the time-correlated single photon counting (TCSPC) setup used for filling-pattern measurements (see Sec. 5.1) while the remaining light is reflected onto the second shortpass filter. It has a cut-off wavelength of 500 nm, consequently, the light that is transmitted through this filter has wavelengths between 400 nm and 500 nm and is sent to the fast-gated intensified camera (FGC) (see Sec 5.2), while the wavelengths above 500 nm are reflected towards the streak camera (SC) [39, 40]. The wavelengths of the two shortpass filters were chosen with respect to an optimal efficiency of the detectors of the different setups. In addition, it has to be ensured that the beam path to the SC does not contain any dispersive elements. As this setup is used for studies of the bunch length, dispersive effects would lead to a lengthening of the light pulses otherwise.

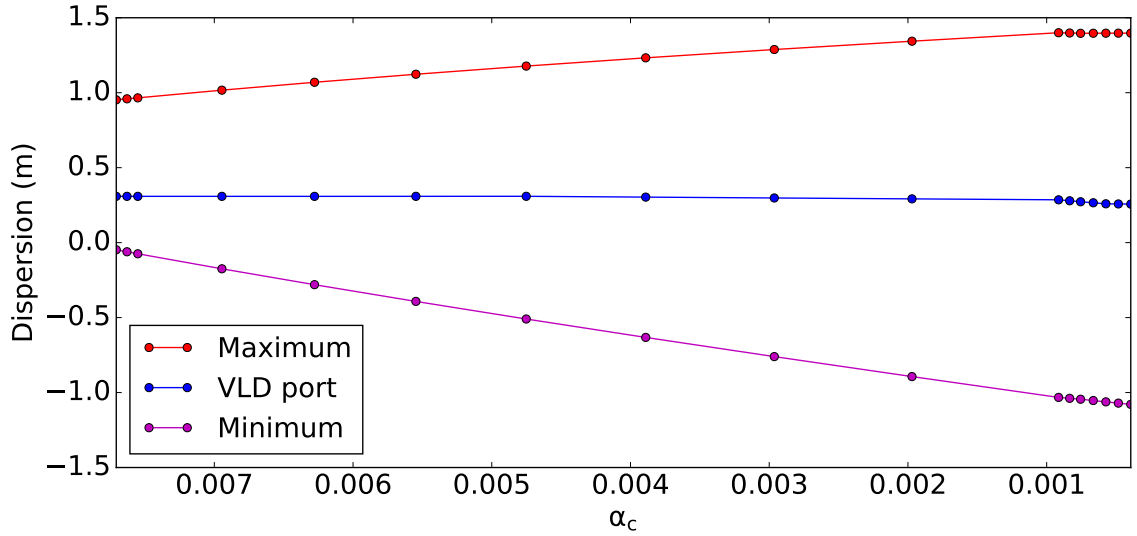


Figure 3.4.: Dispersion at the VLD port (blue) as well as at the position of the maximum (red) and minimum dispersion (purple) plotted over α_c . While it remains almost constant at the VLD port, the maximum value is increasing while the minimum value is decreasing. As this decrease is stronger than the maximums increase, the integral over the dispersion becomes smaller.

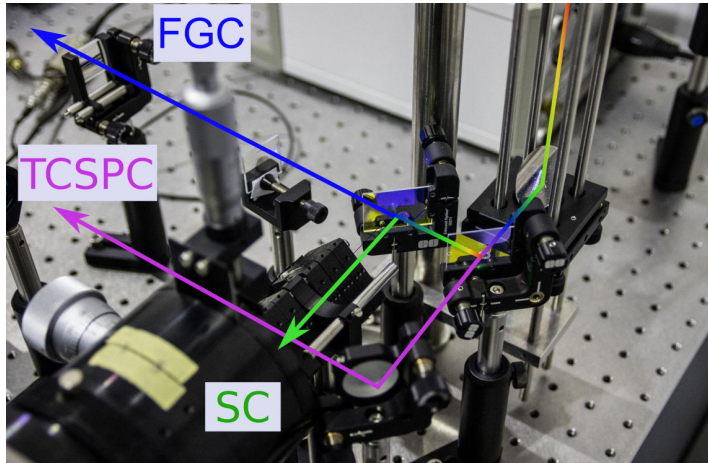


Figure 3.5.: Wavelength separation setup at the VLD port. Coming from the top the light is reflected by an off-axis paraboloid mirror towards a set of two shortpass filters that separates the light for the time-correlated single photon counting (TCSPC), the streak camera (SC) as well as the fast-gated intensified camera (FGC) (published in [38, Fig. 1]).

4. Interaction of the bunch with its environment

When travelling along the beam trajectory, a bunch is undergoing an interaction with its environment. A convenient way to describe this phenomenon is the impedance approach. While an exhaustive description of the accelerator impedance is not feasible, several models exist that can be used to describe different aspects of the interaction. Some of these impedance models are discussed here, followed by the effects the impedance can have on the bunch: A shift of the synchronous phase and of the incoherent synchrotron frequency. When the bunch interacts with its own radiation field, sub-structures can occur that lead to the emission of coherent synchrotron radiation (CSR), which again acts back on the bunch. This micro-bunching instability is discussed in this chapter as well.

4.1. Wake fields and impedances

Assuming a perfectly conducting beam pipe wall with a uniform shape, a bunch will travel without any losses and free of external forces. This changes for a finite resistance of the wall or in case of a change of geometry. In both cases, electromagnetic fields are induced that are dragged behind the bunch which are called wake fields. The following introduction is based on [41, pp. 1-1 ff.].

Those electro-magnetic fields can act back on the bunch and thus the total field seen by the particles can be described as

$$\left(\vec{E}, \vec{B}\right)_{\text{total}} = \left(\vec{E}, \vec{B}\right)_{\text{external fields (RF, magnets)}} + \left(\vec{E}, \vec{B}\right)_{\text{wake fields}}. \quad (4.1)$$

The effect of such a wake field $E(\tau)$ on the charge distribution $\rho(\tau)$ during one turn is given by the *wake potential* $V_w(\tau)$

$$V_w(\tau) = \int_0^L E(\tau, s) ds = \int_{-\infty}^{\infty} W(\tau - \tau') \rho(\tau') d\tau'. \quad (4.2)$$

It is the convolution of the *wake function* $W(\tau)$ with the charge distribution $\rho(\tau)$.

Analogous to conventional circuits, the impedance terminus can be used. The longitudinal impedance Z can be expressed as Fourier transform of the longitudinal wake function:

$$Z(\omega) = \int_{-\infty}^{\infty} W(\tau) e^{-i\omega\tau} d\tau. \quad (4.3)$$

Among the different properties of impedances (see e.g. [41, Eq. (1.31)-(1.35)]), two are of greater interest in the following:

1. The real part of the impedance is even, while the imaginary part is odd:

$$Z^*(\omega) = Z(-\omega). \quad (4.4)$$

When integrating over ω this leads to

$$\int_{-\infty}^{\infty} Z(\omega) d\omega = \int_{-\infty}^{\infty} \text{Re}[Z(\omega)] d\omega = 2 \int_0^{\infty} \text{Re}[Z(\omega)] d\omega. \quad (4.5)$$

2. In case the cross-section of the beam pipe at the entrance as well as at the exit are the same, the real part of the impedance is positive:

$$\text{Re}[Z(\omega)] \geq 0. \quad (4.6)$$

Within the scope of this thesis, only longitudinal impedances are treated.

The effects of the real and imaginary part of an impedance on an ultra-relativistic electron bunch can be described as follows: A purely capacitive impedance ($\text{Im}(Z) < 0$) leads to a shortening of the bunch, while a purely inductive one ($\text{Im}(Z) > 0$) will lengthen it. The resistive part of the impedance ($\text{Re}(Z)$) leads to energy losses of the bunch while passing the structure [41].

In accelerator physics, impedances are responsible for beam instabilities. While a closed formulation of the overall impedance of a storage ring is not feasible, different models exist to describe at least specific parts of the storage ring (radio frequency (RF) cavities, tapers, collimator, ...) or certain interaction effects.

4.1.1. Resistive wall

This impedance describes the effect of a cylindrical beampipe with a finite conductivity [42, p. 204]:

$$Z(\omega) = \frac{Z_0 c L}{\pi} \cdot \frac{1}{[1 + \text{sgn}(\omega)i] bc \sqrt{\frac{\sigma_c Z_0 c}{2|\omega|} - ib^2 \omega}}. \quad (4.7)$$

It is characterized by the beam pipe length L and radius b as well as the conductivity of its material σ_c . Z_0 is the free-space impedance with $Z_0 \approx 377 \Omega$. The beam pipe

at the Karlsruhe research accelerator (KARA) does not have a cylindrical shape (see Fig. 4.1), thus its resistive wall contribution to the impedance can only be estimated using Eq. (4.7). As the impedance increases for smaller values of b , b is set to 16 mm to estimate the maximum impedance effect. The beam pipe is made of Remanit, therefore the conductivity is set to $1.33 \cdot 10^6$ S/m.

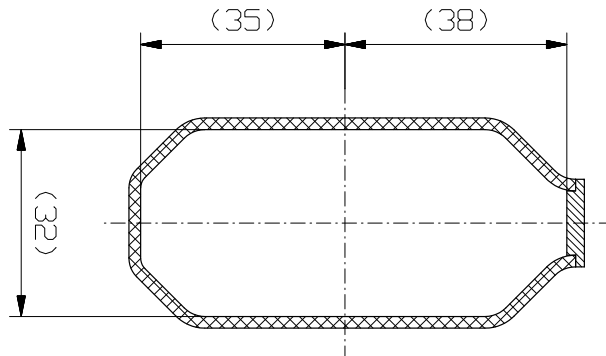


Figure 4.1.: Cross-section of the KARA beam-pipe, the dimensions are given in units of millimetres [43].

In Fig. 4.2, the resistive wall impedance for one turn as well as two form factors for different root mean square (RMS) bunch lengths are plotted.

One can see that there is only a small overlap between the bunch spectrum and the resistive wall impedance if only Gaussian bunches are assumed, even if they have a relatively low bunch length of 1 ps.

4.1.2. CSR impedances

In a bent section of the storage ring, the head of the bunch can interact with the previously emitted radiation from the tail [44]. This interaction is described by the so-called CSR impedance. There are several models for this impedance, two of them are discussed in the following:

- **Free space (FS)**

The most-simple case neglects the effect of the vacuum beam pipe. This free-space CSR impedance scales with $\omega^{1/3}$. A good approximation of this impedance for ultra-relativistic particles ($\gamma \rightarrow \infty$) is given by Agoh [45, Eq. (79)]:

$$Z_{\text{FS}} = Z_0 L \frac{\Gamma(2/3)}{2\pi} \left(i \frac{\omega}{3cR^2} \right)^{1/3} \quad (4.8)$$

with R as (local) bending radius (at KARA: $R = 5.559$ m) and L as length of the structure.

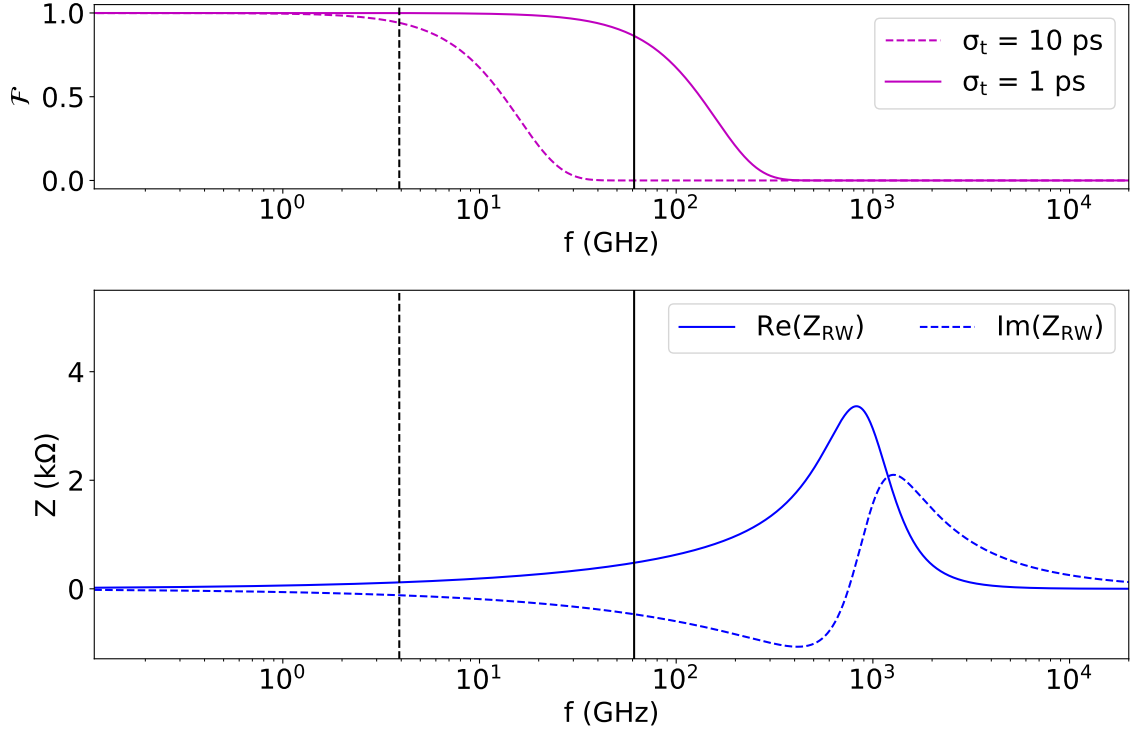


Figure 4.2.: Top: Form factor \mathcal{F} of two Gaussian bunches with 10 ps and 1 ps bunch length, the vertical black lines depict the 3 dB bandwidth. Bottom: Resistive wall (RW) impedance calculated for the KARA beam pipe and one turn. The vertical black lines depict the 3 dB bandwidth of the form factors.

- **Parallel plates (PP)**

A different ansatz is the parallel plates CSR impedance, which takes the shielding by the vacuum pipe into account. The vacuum pipe is approximated by two infinitely large metal plates [46]. Even if the horizontal limits of the beam pipes are not taken into account, this impedance describes the dynamics of the micro-bunching instability at KARA quite well [47]. For ultra-relativistic particles ($\gamma \rightarrow \infty$) in a constant magnetic field it can be written as [45, Eq. (76)]:

$$\begin{aligned}
 Z_{\text{PP}} &= Z_0 L \frac{2\pi}{h_c} \left(\frac{2c}{\omega R} \right)^{1/3} \sum_{p=0}^{\infty} F_0(\beta_p) \\
 F_0(\beta_p) &= Ai'(\beta_p^2) Ci'(\beta_p^2) + \beta_p^2 Ai(\beta_p^2) Ci(\beta_p^2) \\
 \beta_p &= \frac{\pi}{h_c} (2 \cdot p + 1) \left(\frac{2\omega^2}{c^2 R} \right)^{-1/3}.
 \end{aligned} \tag{4.9}$$

It is characterized by the distance of the parallel plates h_c and the bending radius

R (at KARA: $h_c = 32$ mm and $R = 5.559$ m). A_i , C_i and the corresponding derivatives are the Airy functions with $C_i = A_i - iB_i$.

Both impedances are illustrated in Fig. 4.3. For frequencies above 400 GHz, the two impedances are nearly identical as for higher frequencies the shielding effect from the parallel plates vanishes. It is noteworthy that the parallel plates impedance is capacitive for frequencies below 100 GHz, while it is inductive for frequencies above. Also, both impedances have a significantly higher magnitude for frequencies above 40 GHz than the resistive wall impedance. Thus, for this frequency range the contribution of the CSR impedance is expected to be dominant.

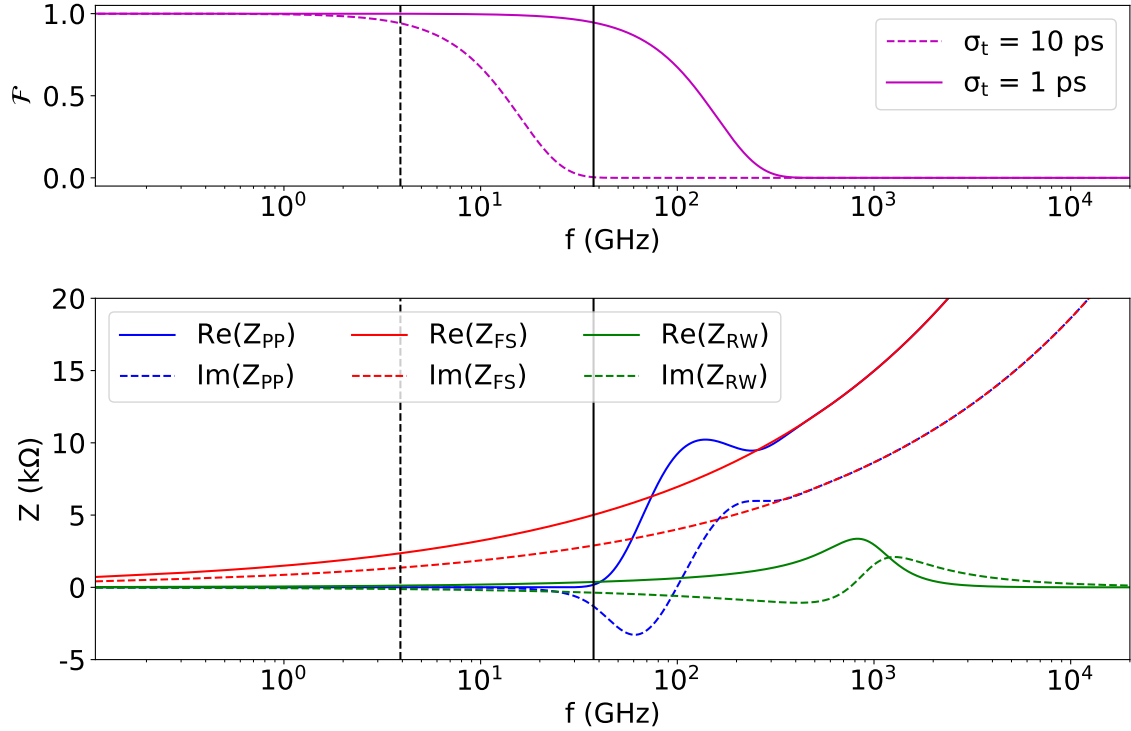


Figure 4.3.: Top: Form factor \mathcal{F} of two Gaussian bunches with 10 ps and 1 ps bunch length, the vertical black lines depict the 3 dB bandwidth. Bottom: Real and imaginary part of the parallel plates (PP), the free-space (FS) CSR impedance and the resistive wall impedance (RW) calculated for KARA. The vertical black lines depict the 3 dB bandwidth of the form factors.

4.2. Impedance effects

In general, an impedance leads to a distortion of the potential well. Thus, the knowledge of the impedance is crucial to understand, predict and even prevent beam instabilities. As it cannot be measured directly, indirect measurements have to be used to allow estimations of the impedance. Two possible ways to probe impedance related effects are the measurement of the synchronous phase shift and the incoherent synchrotron frequency shift.

4.2.1. Synchronous phase shift

Due to the emission of synchrotron radiation, an electron loses energy, which is compensated by the RF cavities. The energy loss due to synchrotron radiation consists of two components: The first is due to incoherent losses that do not depend on the bunch current, while the second – coherent – part depends on the bunch current and shape, the latter one is given by the form factor. These losses lead to a current-dependent shift of the synchronous phase as it is derived from Eq. (2.23) in the following.

Due to the two components of the energy loss, the synchronous phase has to be separated in two parts: $\tilde{\phi}_s = \phi_s + \Delta\phi$ and, Eq. (2.23) becomes

$$NeV_{\text{RF}} \sin(\phi_s + \Delta\phi) = NU, \quad (4.10)$$

with N as number of electrons per bunch and U as energy loss per electron and turn. The energy loss per bunch and turn (NU) due to the coherent and incoherent synchrotron radiation can be calculated with the radiation power from Eq. (2.10):

$$\begin{aligned} NU &= \int_{-\infty}^{\infty} P(\omega) d\omega = \int_{-\infty}^{\infty} e^2 Z(\omega) \cdot (N + N^2 \mathcal{F}) d\omega \\ &= \underbrace{Ne^2 2 \int_0^{\infty} \text{Re}[Z(\omega)] d\omega}_{\text{Incoherent}} + \underbrace{N^2 e^2 2 \int_0^{\infty} \text{Re}[Z(\omega)] \mathcal{F}(\omega) d\omega}_{\text{Coherent}}. \end{aligned} \quad (4.11)$$

Here, $p_0(\omega) = e^2 \text{Re}[Z(\omega)]$ was used with $Z(\omega)$ as impedance for one turn and the impedance property from Eq. (4.5). Finally, Eq. (4.10) can be written as

$$NeV_{\text{RF}} \sin(\phi_s + \Delta\phi) = Ne^2 2 \int_0^{\infty} \text{Re}[Z(\omega)] d\omega + N^2 e^2 2 \int_0^{\infty} \text{Re}[Z(\omega)] \mathcal{F}(\omega) d\omega. \quad (4.12)$$

Using addition theorems at the left side leads to

$$\begin{aligned} &NeV_{\text{RF}} \sin(\phi_s) \cos(\Delta\phi) + NeV_{\text{RF}} \cos(\phi_s) \sin(\Delta\phi) \\ &= 2Ne^2 \int_0^{\infty} \text{Re}[Z(\omega)] d\omega + 2N^2 e^2 \int_0^{\infty} \text{Re}[Z(\omega)] \mathcal{F}(\omega) d\omega. \end{aligned} \quad (4.13)$$

As $\Delta\phi$ is assumed to be small, one can set $\cos(\Delta\phi) = 1$ and $\sin(\Delta\phi) = \Delta\phi$. Thus, the equation simplifies to

$$\begin{aligned} & NeV_{\text{RF}} \sin(\phi_s) + NeV_{\text{RF}} \Delta\phi \cos(\phi_s) \\ &= 2Ne^2 \int_0^\infty \text{Re}[Z(\omega)] d\omega + 2N^2 e^2 \int_0^\infty \text{Re}[Z(\omega)] \mathcal{F}(\omega) d\omega. \end{aligned} \quad (4.14)$$

The first terms on both sides are the incoherent terms, while the second ones describe the coherent losses that depend on the bunch shape given by the form factor $\mathcal{F}(\omega)$. As the synchronous phase ϕ_s is the phase where the incoherent losses are compensated, the coherent losses lead to a – bunch current dependent – phase shift $\Delta\phi$:

$$NeV_{\text{RF}} \Delta\phi \cos(\phi_s) = N^2 e^2 2 \int_0^\infty \text{Re}[Z(\omega)] \mathcal{F}(\omega) d\omega. \quad (4.15)$$

With $Ne = T_0 I_b$, this can be written as

$$\Delta\phi = \frac{2T_0 I_b}{V_{\text{RF}} \cos(\phi_s)} \int_0^\infty \text{Re}[Z(\omega)] \mathcal{F}(\omega) d\omega. \quad (4.16)$$

The integral part is often referred to as *loss factor* k [24, Eq. (22.17)]:

$$k = 2 \int_0^\infty \text{Re}[Z(\omega)] \mathcal{F}(\omega) d\omega. \quad (4.17)$$

The synchronous phase shift in Eq. (4.16) is given in units of radians. Taking the RF period length into account, the synchronous phase can be written in time units as

$$\Delta\phi_\tau = \frac{2T_0^2}{2\pi \cdot h \cdot V_{\text{RF}} \cos(\phi_s)} I_b \int_0^\infty \text{Re}[Z(\omega)] \mathcal{F}(\omega) d\omega. \quad (4.18)$$

To measure the synchronous phase shift, a precise determination of the arrival time of the bunches is required. To cover the required bunch current range, two different approaches can be used. The first is to track the arrival time of a single bunch over the decay of the bunch current, while the second one uses a dedicated filling pattern where each bunch has a different current. This approach requires a machine with a large harmonic number to prevent beam loading effects [48]. With a harmonic number h of 184, this approach is not seen as suitable for KARA, therefore the method using the bunch current decay is used here. As such a measurement takes a long time (up to several hours), this requires a good long-term stability of the detectors and the timing system.

As it will be discussed in Sec. 8.3.2, the synchronous phase shift can be measured by different methods. Regardless which one of them is used, it *only* gives the convolution of the real part of the impedance with the bunch spectrum. With knowledge of the longitudinal bunch profile (e.g. from electro-optical spectral decoding (EOSD) measurements) it would be possible to calculate the bunch spectra and to do a deconvolution to reveal the real part of the impedance.

4.2.2. Incoherent synchrotron frequency shift

In Eq. (2.31), the last summand has been neglected so far. Taking this term into account as well, the differential equation becomes

$$\Delta\ddot{E} + \frac{1}{T_0} \frac{dU}{dE} \Delta\dot{E} + \underbrace{\left[-\frac{2\pi h \alpha_c e V_{\text{RF}} \cos(\phi_s)}{T_0^2 E_0} + \frac{\alpha_c}{T_0 E} \frac{dU}{dt} \right]}_{\omega_s^2} \Delta E = 0. \quad (4.19)$$

The energy loss U can be expressed as a voltage V induced by the electron and thus $U = eV$. This voltage – that corresponds to the wake potential – is given by the spectrum of the bunch current $\tilde{I}(\omega)$ and the impedance

$$V = \int_{-\infty}^{\infty} \tilde{I}(\omega) Z(\omega) e^{i\omega t} d\omega. \quad (4.20)$$

It changes with time as

$$\frac{dV}{dt} = i\omega \int_{-\infty}^{\infty} \tilde{I}(\omega) Z(\omega) e^{i\omega t} d\omega. \quad (4.21)$$

Averaging over the whole bunch finally gives

$$\left\langle \frac{dV}{dt} \right\rangle = I_b \int_{-\infty}^{\infty} \text{Im} [Z(\omega)] \omega \mathcal{F}(\omega) d\omega. \quad (4.22)$$

Thus, Eq. (4.19) can be written as

$$\Delta\ddot{E} + \frac{1}{T_0} \frac{dU}{dE} \Delta\dot{E} + \underbrace{\left[-\frac{2\pi h \alpha_c e V_{\text{RF}} \cos(\phi_s)}{T_0^2 E_0} + \frac{\alpha_c}{T_0 E} e I_b \int_{-\infty}^{\infty} \text{Im} [Z(\omega)] \omega \mathcal{F}(\omega) d\omega \right]}_{\omega_s^2} \Delta E = 0. \quad (4.23)$$

Compared to the unperturbed case in Eq. (2.31), the impedance leads to a shift of the frequency with

$$\begin{aligned} \omega_s^2 = 4\pi^2 f_s^2 &= -\frac{2\pi h \alpha_c e V_{\text{RF}} \cos(\phi_s)}{T_0^2 E_0} + \frac{\alpha_c}{T_0 E} e I_b \int_{-\infty}^{\infty} \text{Im} [Z(\omega)] \omega \mathcal{F}(\omega) d\omega \\ &= \omega_{s,0}^2 \left[1 - \frac{T_0}{2\pi V_{\text{RF}} \cos \phi_s} I_b \int_{-\infty}^{\infty} \text{Im} [Z(\omega)] \omega \mathcal{F}(\omega) d\omega \right] \end{aligned} \quad (4.24)$$

For small effects, the frequency shift Δf_s – which is the difference between the coherent motion with the frequency f_s^{coh} (see Eq. (2.32) and the incoherent motion with the frequency f_s^{inc} – can be written as:

$$\Delta f = \frac{T_0}{4\pi V_{\text{RF}} \cos \phi_s} I_b \int_{-\infty}^{\infty} \text{Im} [Z(\omega)] \omega \mathcal{F}(\omega) d\omega. \quad (4.25)$$

4.3. Potential well distortion

A more general – and also more elegant – way to describe physical systems and phenomena is to use the Hamiltonian formalism. For the two effects discussed before (phase and frequency shift) a more *intuitive* approach was used. In general, the additional voltage induced by the bunch current via the impedance leads to a deformation of the potential well.

For a single particle within a bunch, the Hamiltonian can then be written as [24, Eq. (22.122)]

$$\begin{aligned}\mathcal{H} &= -\frac{1}{2}\alpha_c \left(\frac{\Delta E}{E_0}\right)^2 - \frac{1}{2}\frac{\omega_{s,0}^2}{\alpha_c}\tau^2 - \frac{e}{E_0 T_0} \int_0^\tau V_w(\tau') d\tau' \\ &= \underbrace{-\frac{1}{2}\alpha_c \left(\frac{\Delta E}{E_0}\right)^2 - \frac{1}{2}\frac{\omega_{s,0}^2}{\alpha_c}\tau^2}_{\mathcal{H}_0} + \frac{e}{E_0 T_0} \int_0^\tau \int_{-\infty}^\infty Z(\omega) \tilde{I}(\omega) e^{i\omega\tau'} d\omega d\tau'.\end{aligned}\quad (4.26)$$

The relative energy deviation $\Delta E/E_0$ and the arrival time offset from the center of the bunch τ span the longitudinal phase space. The term \mathcal{H}_0 is the Hamiltonian for the unperturbed case, where the synchrotron oscillation with the angular frequencies $\omega_{s,0} = 2\pi f_{s,0}$ (see Eq. (2.32)) corresponds to a rotation in the phase space.

Strictly speaking, the Hamilton formalism cannot be used here due to dissipative forces like radiation damping. Nevertheless – as the radiation damping time is longer than one synchrotron period – damping can be neglected on small time scales and thus the formalism can still be used.

The perturbation due to the wake fields is added as an additional term to \mathcal{H}_0 and leads to a distortion of the parabolic potential well from the RF.

Due to random quantum excitation and radiation damping, the stationary phase space distribution factorizes into a Gaussian distribution along the energy axis $\Delta E/E_0$ and the longitudinal distribution $\rho(\tau)$ [24, Eq. (22.136)]:

$$\psi(\Delta E/E_0, \tau) = C \exp\left(-\frac{\Delta E^2}{2\sigma_\delta^2}\right) \cdot \rho(\tau). \quad (4.27)$$

In the longitudinal phase space, the potential well distortion will only be visible as deformation of the temporal distribution $\rho(t)$, while the energy distribution still has a Gaussian shape with the energy spread σ_δ as width. This is shown in Fig. 4.4, where a simulated energy profile and a longitudinal bunch profile are plotted. Both are simulated using the software Inovesa, which simulates the longitudinal phase space [49]. For these simulations, the parallel plates CSR impedance was used.

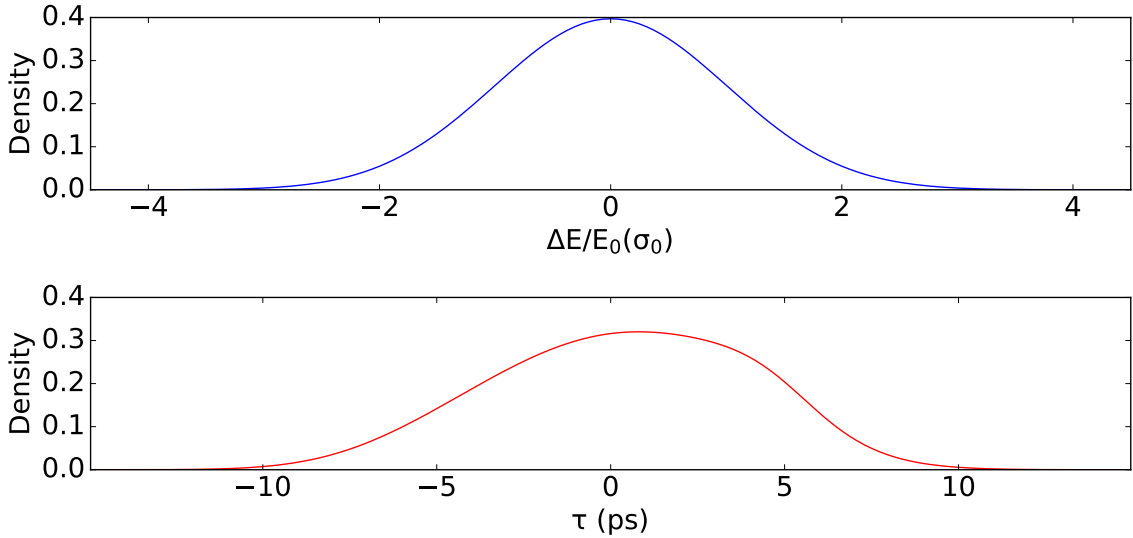


Figure 4.4.: Simulated energy and longitudinal bunch profile for potential well distortion due to the parallel plates CSR impedance. Top: Energy profile with Gaussian shape, the x-axis is given in units of the natural energy spread σ_0 , Bottom: Longitudinal bunch profile.

Simulation parameter: $E_0 = 1.3$ GeV, $I_b = 0.15$ mA, $\sigma_0 = 4.7 \times 10^{-4}$, $f_s = 11.2$ kHz, parallel plates distance $h_c = 32$ mm.

While the energy profile follows a Gaussian distribution, the longitudinal bunch profile is distorted and follows a Haüssinski distribution. As long as there is no additional instability, the energy spread remains constant at the value of the natural energy spread σ_0 according to Eq. (2.42).

4.4. Micro-bunching instability

If the electron density exceeds a certain threshold, the distortion of the potential well due to the interaction with the CSR can be so strong, that there is no longer a stationary distribution possible. In this case, small perturbations are not damped away but grow in intensity [12]. They occur as sub-structures on the bunch profile and the self-interaction of the bunch with its own radiation leads to a rapid increase of their amplitudes. As the growth time of this instability is much shorter than the damping period, this is visible as a sawtooth-like modulation on the the energy spread [50]. The rapid growth of the sub-structures leads to an increase of the bunch size. At a certain point, radiation damping becomes dominant and the bunch size starts to shrink. When a certain critical value for the charge density is reached, the sub-structures start to grow again and the next cycle sets in. Figure 4.5 shows an Inovesa simulation for this case.

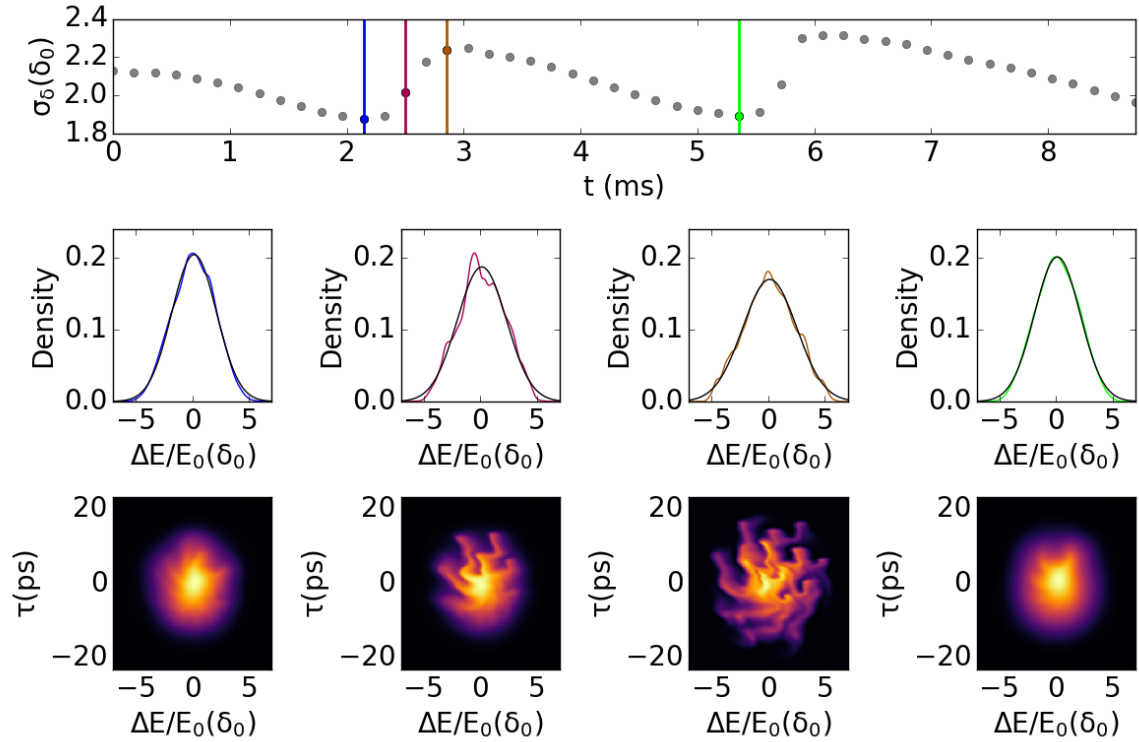


Figure 4.5.: Inovesa simulations of the bursting behaviour of the bunch during the micro-bunching instability. The top row shows the energy spread undergoing a sawtooth like modulation. For four time steps, the corresponding energy profiles are plotted in the middle row, where the black lines depict Gaussian fits. The corresponding longitudinal phase spaces are plotted in the bottom row. Simulation parameters: $E_0 = 1.3$ GeV, $I_b = 1.28$ mA, $\sigma_0 = 4.7 \cdot 10^{-4}$, $f_s = 11.2$ kHz, parallel plates distance $h_c = 32$ mm.

The top panel shows the energy spread which is undergoing a sawtooth modulation. For four time steps, the corresponding energy profiles as well as the longitudinal phase spaces are plotted in the middle and bottom panel, respectively. While the energy profile is rather smooth at the onset of the burst, it is distorted as sub-structures occur on the profile. They quickly rise in amplitude, before radiation damping starts to dominate leading to a shrinking of the energy spread and to a smoothing of the energy profile. As the CSR emission depends on the sub-structures, that arise quickly and are damped down afterwards, the CSR also shows a sawtooth pattern. This is illustrated in Fig. 4.6, where the CSR signal detected by a Schottky diode (which measures the incoming radiation power [51]) is plotted over time. This behaviour of the bunch is often referred to as *bursting*.

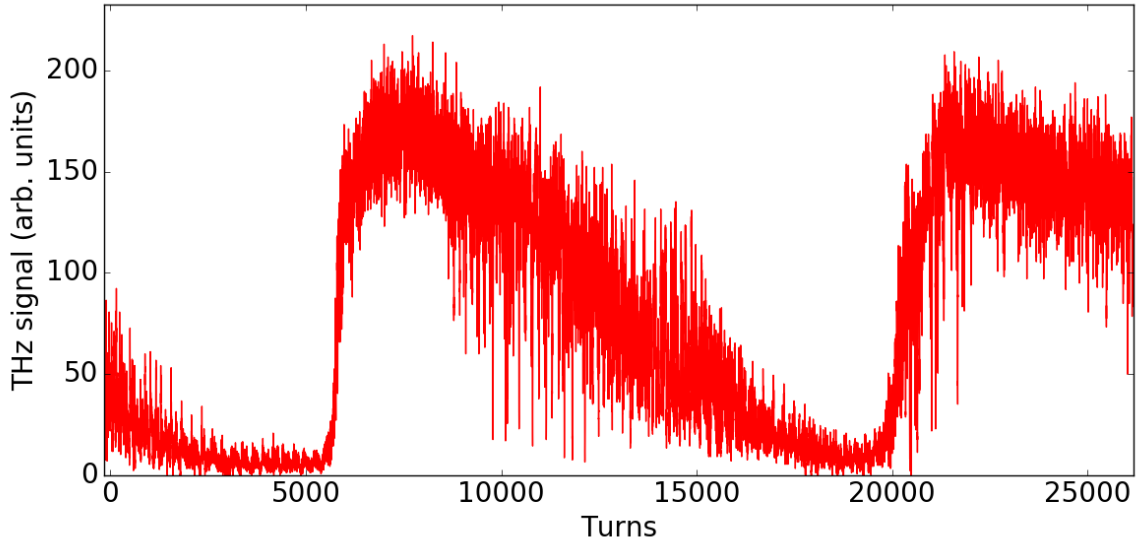


Figure 4.6.: Typical sawtooth-like CSR intensity recorded using a Schottky diode and KAPTURE [52, 53]. The curve is not the detector response, but the amplitude of the detectors peak signal sampled once per turn (Data taken by Miriam Brosi).

Chao and Gareyte derived a scaling law for the bunch length during this instability [54]: If the impedance depends on the frequency like

$$Z \propto \omega^a, \quad (4.28)$$

the bunch length as well as the energy spread both scale with

$$\sigma_\delta \propto \sigma_z \propto I_b^{\frac{1}{2+a}}. \quad (4.29)$$

This scaling law has been verified at other storage rings, e.g. SPEAR II and PEP [54]. While the frequency dependence of the parallel plates CSR impedance is sophisticated, the one for the free-space CSR impedance is simpler: It scales with $\omega^{\frac{1}{3}}$ (Eq. (4.8), see also Fig. 4.3). For high frequencies, the parallel plates impedance can be approximated by the free-space CSR impedance. Hence, this simplification will lead to a scaling of the bunch length as $\sigma_z \propto (I_b)^{3/7}$.

This gives an additional estimation on the behaviour of the energy spread during the micro-bunching instability. It is also noteworthy, that the sawtooth-like modulation of the bunch shape and the CSR discussed above, are only occurring for certain bunch current ranges. In addition, other so-called *bursting regimes* exist for other bunch currents [55]. The different regimes are characterized by the temporal profile of the CSR emission, but they all have the existence of sub-structures on the bunch in common. For the onset of the micro-bunching instability, a lower threshold current can be derived.

4.5. Bursting threshold

The micro-bunching instability only occurs for bunch currents above a certain threshold current, this threshold is referred to as *bursting threshold* [55]. The onset of the micro-bunching instability is usually defined as the current, at which the energy spread starts to increase. For the parallel plates CSR impedance, numerical simulations of the longitudinal phase led to the following relation for the bunch current I_b at this threshold [56]:

$$I_b = I_A \gamma \delta_0^2 \alpha_c R^{-\frac{1}{3}} \sigma_{z,0}^{\frac{1}{3}} \left(0.5 + 0.34 R^{\frac{1}{2}} \sigma_{z,0} (h_c/2)^{-\frac{2}{3}} \right) \quad (4.30)$$

$$\sigma_{z,0} = \frac{c \alpha_c}{2\pi f_s} \delta_0 \quad (4.31)$$

$$= \sqrt{-\frac{\alpha_c c^2 T_0^2 E_0}{2\pi h e V_{RF} \cos \phi_s}} \delta_0. \quad (4.32)$$

with the parameters according to Table 4.1.

To change the bursting threshold, the beam energy E_0 , the RF voltage V_{RF} and the momentum compaction factor α_c (e.g. by changing the magnet current in the dipole and sextupole magnets) can be varied. The scaling law of the bursting threshold calculated by Eq. (4.32) was successfully confirmed by measurements at KARA [47].

Table 4.1.: Parameters for the scaling law for the bursting threshold

Parameter		Typical values for KARA
I_A	Alfven current	17045 A
γ	Relativistic gamma factor	2500 - 4900
δ_0	Natural energy spread	$4.7 \cdot 10^{-4}$ - $9.2 \cdot 10^{-4}$
α_c	Momentum compaction factor	$1.6 \cdot 10^{-4}$ - $9.4 \cdot 10^{-3}$
R	Bending radius	5.559 m
$\sigma_{z,0}$	Natural bunch length	1.9 - 38.2 ps
h_c	Vacuum chamber height	32 mm

5. Optical diagnostics

Incoherent synchrotron radiation is a versatile diagnostics tool for accelerator physics as the light pulse directly represents the charge distribution of the bunch. In this chapter, the diagnostics setups using this feature are presented: The filling pattern monitor based on time-correlated single photon counting (TCSPC), the FGC as well as the KALYPSO system. The latter two are used to measure the horizontal bunch profile and thus the energy spread. All setups are located at the visible light diagnostics (VLD) port (see Sec. 3.3).

5.1. Time-correlated single photon counting

The distribution of the beam current on the individual bunches is called *filling pattern*. As the micro-bunching instability crucially depends on the bunch current, a precise measurement of the filling pattern is required. At the KARA, the technique of TCSPC is used [57]. It is based on the measurement of the arrival time distribution of single photons from the incoherent synchrotron radiation relative to the revolution clock. This distribution directly represents the relative filling pattern and in combination with the measurement of the total beam current by a DC current transformer (DCCT) [22, pp. 301 ff.], this allows precise measurements of the bunch charges. Compared to the *classical* approach of sampling in the time-domain by using a fast photo-detector (e.g. an avalanche photodiode) and a dedicated DAQ system (e.g. a fast oscilloscope), TCSPC has the advantage of being cost-efficient and it provides a high dynamic range. Apart from a precise determination of the filling pattern, the system can also be used for studies of the synchronous phase shift. In this case, the arrival times of the bunches relative to a reference signal is studied during a bunch current decay.

5.1.1. Experimental setup

The setup used at KARA consists of a single photon avalanche diode (SPAD) [58] that is sensitive to single photons in the visible wavelength range and a PicoHarp 300 as histogramming device which offers 65536 histogram time bins [59]. In case of KARA with a revolution time of 368 ns, their width is set to 8 ps to cover one complete revolution. The optical setup is depicted in Fig. 5.1 and consists of a 400 nm

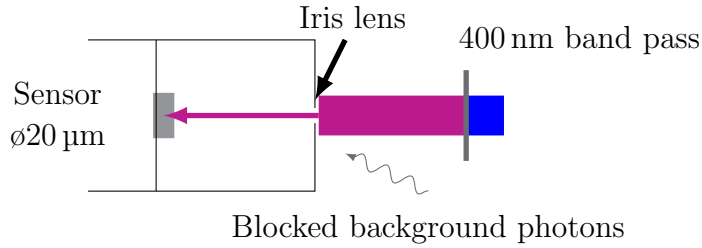


Figure 5.1.: Principle scheme of the optical setup for TCSPC.

bandpass filter and an iris lens mounted directly in front of the SPAD sensor. The combination of the small iris lens and the sensor with a diameter of $20\ \mu\text{m}$ acts as an optical discriminator blocking photons from background radiation. Thus the setup can be operated without any additional background light shielding [38].

The bandpass filter (center wavelength $400\ \text{nm}$, FWHM $\pm 10\ \text{nm}$) suppresses the formation of the *diffusion tail* in the arrival time histogram, as for short wavelengths the penetration depth of light in silicon is reduced [60]. This reduces the probability to create electron-hole pairs outside of the depletion zone which then diffuse into the depletion zone where they trigger an avalanche after a statistically fluctuating delay [61].

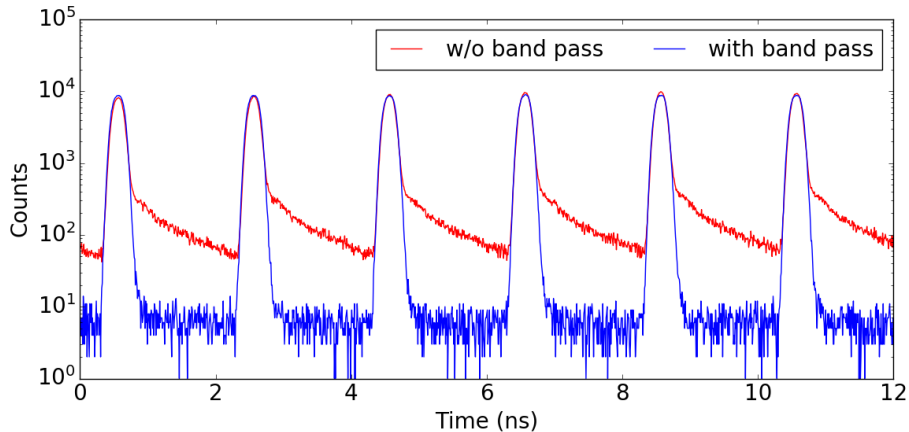


Figure 5.2.: Raw data histogram without (red) and with a $400\ \text{nm}$ bandpass filter (blue) mounted in front of the SPAD (published in [38, Fig. 2]).

The effect of this filter is illustrated in Fig. 5.2, where two raw data histograms recorded with and without the band pass filter are plotted. The band pass filter significantly reduces the exponential decay which follows each peak, this also increases the dynamic range.

The wavelength of $400\ \text{nm}$ is a trade-off between a short wavelength and a sufficient quantum efficiency of the detector.

5.1.2. Dead-time correction

To get a high dynamic range, a large number of photons per bin is required. To increase this number, a long integration time and a high count rate can be used, but both suffer from some drawbacks:

While a longer integration time leads to a higher number of photons, the beam current is simultaneously decaying which eventually reduces the resolution again. If the count rate becomes too high, dead-time effects start to play a role as the probability for a photon not to be detected increases. Both the SPAD and the PicoHarp have a certain dead-time where they cannot handle incoming events. When a photon hits the SPAD and an avalanche has been triggered and detected, the bias voltage of the pn-junction is reversed to quench the avalanche before the bias voltage is restored and the next photon can be detected. This quenching takes a certain time in which the detector is blind to additional incoming photons. The dead-time of the PicoHarp, in which the device cannot handle incoming logical pulses from the SPAD, is defined by the electronics.

Both dead times have been measured with $\tau_{d, \text{PH}} = (86.8 \pm 0.2)$ ns for the PicoHarp and $\tau_{d, \text{SPAD}} = (37 \pm 1)$ ns for the SPAD (see Sec. A.1.1).

The probability of a photon not to be recorded as it is falling into the dead-time is increasing with photon rate. As a consequence, the histogram is distorted. To estimate and prevent this distortion, a dead-time correction scheme has been implemented. It is based on the ansatz presented in [62] which was adjusted according to the needs of a synchrotron acting as light source. It allows for each bin i the calculation of the *real* number of photon ν_i from the recorded number of photons n_i :

$$\nu_i = \frac{n_i}{\prod_{j=i-n\tau_{d, \text{PH}}}^{i-b} \left(1 - \frac{n_j}{N}\right)} \approx \frac{n_i}{1 - \sum_{j=i-n\tau_{d, \text{PH}}}^{i-b} \frac{n_j}{N}} \quad (5.1)$$

The different parameters are summarised in Table 5.1.

This dead-time correction scheme is based on the following assumptions:

- The dead-time of the PicoHarp dominates, the one of the SPAD is a second order effect which can be neglected (see Sec. A.1.2 in the appendix).
- The probability $p_i = n_i/N$ for an event to be detected in bin i is small (typically $1 \cdot 10^{-4}$), allowing to replace the product in the nominator by a sum. In addition, this provides a higher numerical stability as higher order terms are neglected.
- There is only one photon emitted per bunch and turn and thus the correction scheme only takes the photons from the previous bunches into account (sum ends at $i - 50$).

Table 5.1.: Parameters for the PicoHarp dead-time correction.

Variable	Meaning	Value
ν_i	<i>Real</i> number of photons / bin	
n_i, n_j	Measured counts / bin	
$\tau_{d, \text{PH}}$	PicoHarp dead-time	86.8 ns
$n_{\tau_{d, \text{PH}}}$	Bins per PicoHarp dead-time	10850
b	Bins per bunch	50
T_{Acq}	Acquisition time	Typically 30 s
T_{Rev}	Revolution time	368 ns
N	Number of excitation cycles	$T_{\text{Acq}}/T_{\text{Rev}}$

To test the dead-time correction scheme, two histograms are taken with different photon rates. From the one with the lower rate ($1.9 \cdot 10^4$ counts/s), the reference filling pattern is calculated. In the histogram with the high count rate ($1.2 \cdot 10^6$ counts/s), dead-time effects induce a distortion which is corrected using the correction scheme discussed above. From the distorted as well as the corrected histograms, filling patterns are determined, which are finally compared to the reference pattern. This comparison is illustrated in Fig. 5.3.

As the effect of the distortion and the dead-time correction are *relatively* small, they are illustrated in the bottom panel in more detail. There, the blue curve shows the difference between the reference filling pattern and the one distorted by the dead-time, while the green one shows the difference between the reference filling pattern and the dead-time corrected one. The dead-time leads to bunch current differences of up to $\pm 50 \mu\text{A}$. The dead-time correction scheme reduces this difference to values of below $\pm 10 \mu\text{A}$. Finally, the corrected and the reference filling pattern coincide mostly within the uncertainty of the reference filling pattern which is indicated by the grey area. This uncertainty is determined using Monte-Carlo studies.

This shows that the dead-time correction scheme is adequate to reduce the distortion induced by the PicoHarp dead-time significantly which allows precise studies of possible multi-bunch effects in the emission of coherent synchrotron radiation (CSR) [64].

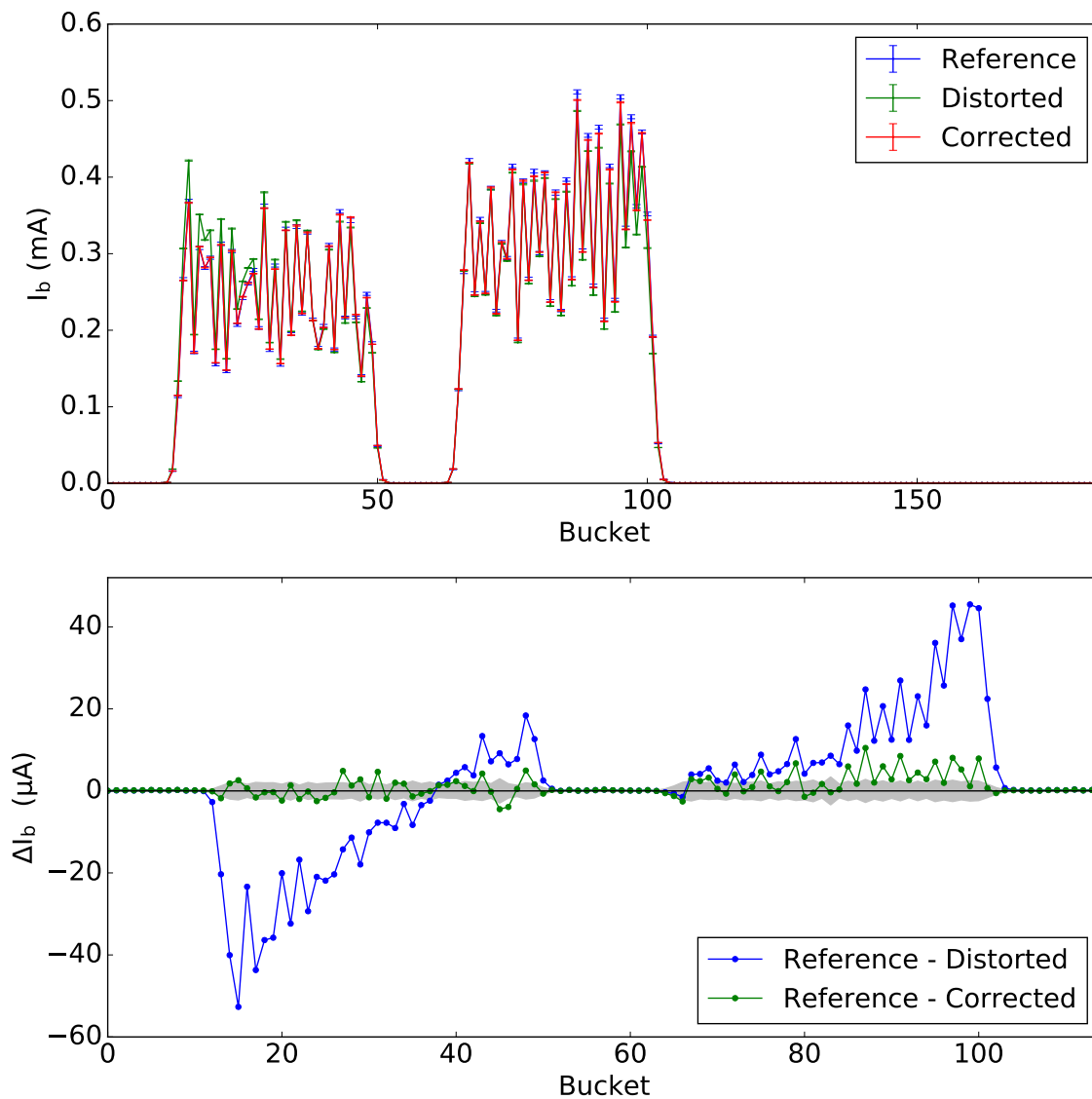


Figure 5.3.: Top panel: Reference, distorted and dead-time corrected filling pattern. Bottom panel: Difference between the reference and the distorted (blue) and corrected (green) filling pattern. The grey area depicts the uncertainty of the reference filling pattern (published in [63, Fig. 3]).

5.1.3. Data analysis

The TCSPC is primarily used for precise measurements of the filling pattern, but also allows studies of the synchronous phase shift by tracking the bunch arrival times. Both measurement techniques require dedicated data analysis schemes, which are discussed in the following.

Filling pattern determination

To determine the distribution of the current on the 184 radio frequency (RF) buckets from the raw data histogram with 65536 bins, three steps are required:

1. Group the first 368 ns of the histogram in 184 intervals with 2 ns width.
2. Determine the local maximum for each interval and sum over the adjacent bins. Monte-Carlo studies showed, that the best performance is achieved, if the 25 preceding and the 25 successive bins are taken into account.
3. Normalise these 184 values to a sum of 1 to get the relative filling pattern.

This is illustrated in Fig. 5.4.

For the error on the bunch currents, two contributions are assumed and taken into account:

- **Counting error per bin σ_i :** Assuming Poisson's statistics, it is calculated from the number of counts per bin n_i by $\sigma_i = \sqrt{n_i}$.
- **Beam current error:** As the beam current decays during the acquisition time, it is measured at the beginning and at the end of each measurement. As uncertainty for the mean value the standard deviation is taken, which corresponds to half of the difference between the two values. In addition, the DCCT has a measurement error of 0.5 μA [65]. These two contribution are added quadratically to get the beam current error.

The resulting bunch current errors are determined by a Monte-Carlo error propagation. There, the data analysis is repeated many times and the input parameters (raw data histogram and beam current) are varied according to their error as standard deviation. Finally, the mean and the standard deviation of the result is calculated. This allows to study the influence of the different uncertainties on the resulting values. Usually, the contribution from the counting statistics dominates, as it is also illustrated in Fig. 5.5. There, two consecutive measurements with different photon rates are compared. To lower the photon rate, a neutral density (ND) filter with an optical density of 0.01 is

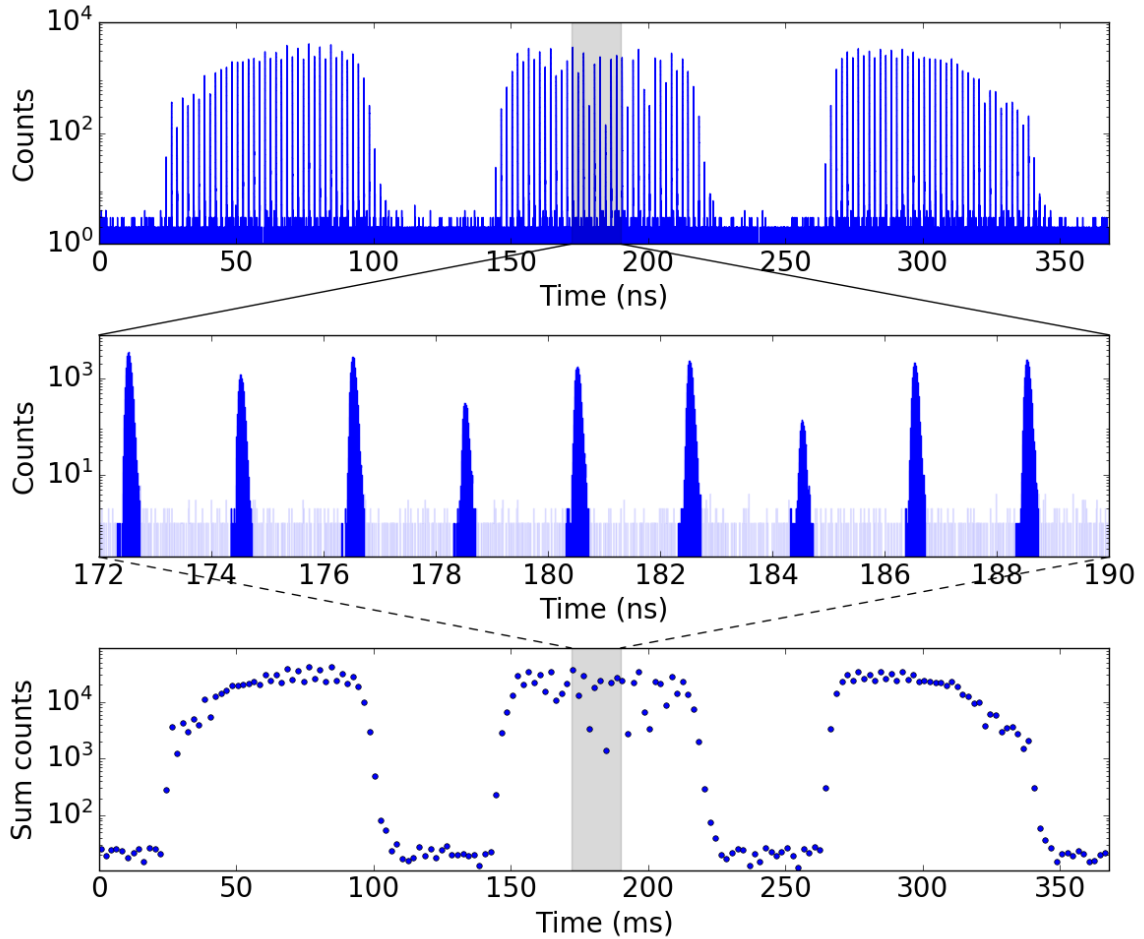


Figure 5.4.: Raw data histogram and zoom-in, the dark blue areas indicate the bins used for integrating the counts to calculate the filling pattern (top and center panel, respectively). The bottom panel shows the integrated counts for the 184 RF buckets (data published in [63, Fig. 1]).

used which leads to the reduction of the photon flux by approximately two orders of magnitude.

While Fig. 5.5a shows a case for a high count rate and thus *good* statistics, Fig. 5.5b shows the same fill (data taken three minutes later) for a count rate which is two orders of magnitude lower due to the usage of a ND filter. For the higher count rate, the histogram and thus the filling pattern has a smoother shape and also the error on the bunch current is one order of magnitude lower.

For the measurements with the fast-gated intensified camera (FGC) discussed in Sec. 8, single bunch fills have been used. There, the TCSPC based filling pattern measurements are important to ensure that there is only one bunch in the storage ring. In Fig. 5.6, a zoom into a TCSPC raw histogram for such a single bunch fill is plotted.

Calculating the ratio of the counts for the bunch at 306 ns and the counts for the

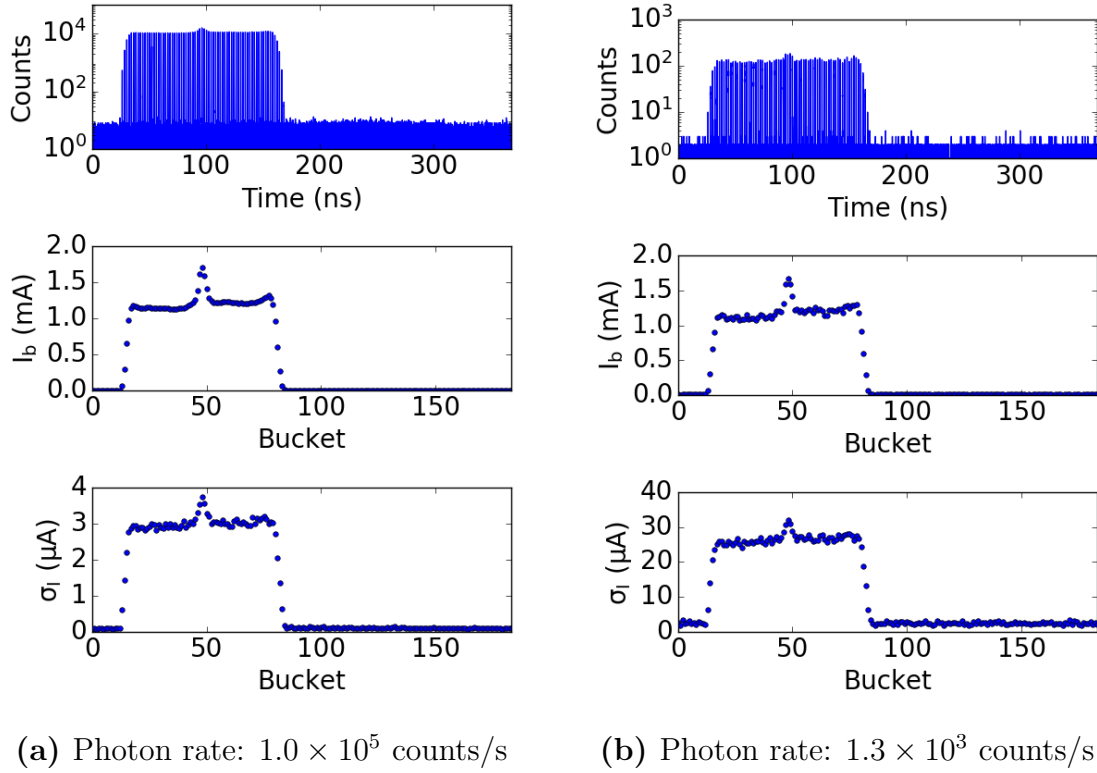


Figure 5.5.: TCSPC histograms, the corresponding bunch currents I_b and their measurement errors σ_I for the same fill with two different photon count rates (published in [63, Fig. 2]).

adjacent bucket leads to $2.3 \cdot 10^4$, which illustrates also the high dynamic range of the setup. This ratio is referred to as *bunch purity* [66]. It is a measure for the quality of a single bunch fill as it gives the ratio between the charge in the *wanted* and the *unwanted* buckets.

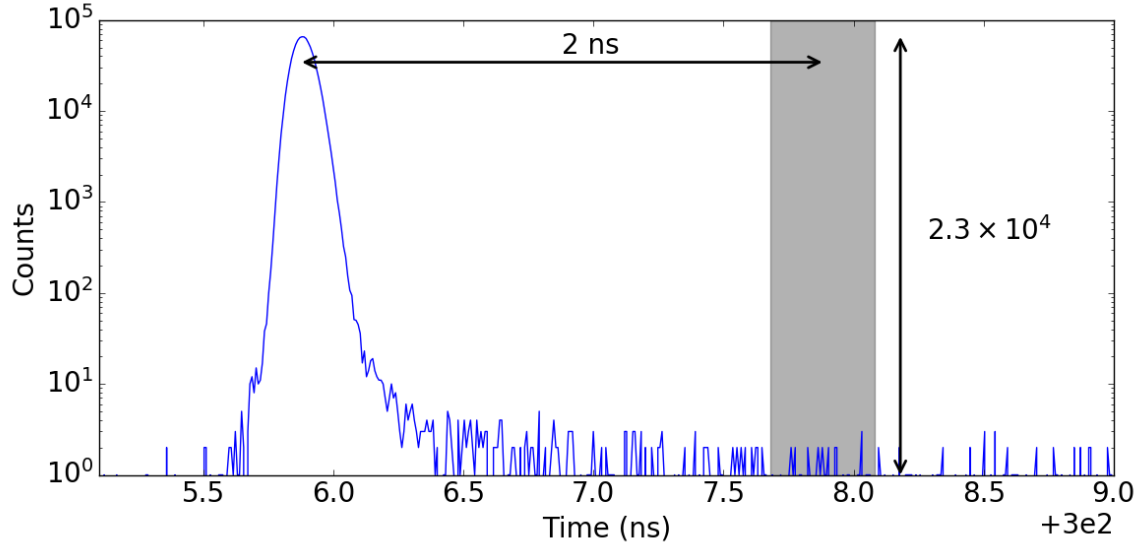


Figure 5.6.: TCSPC raw data histogram. The peak at 306 ns is the signature of a bunch while at the position of the adjacent bucket 2 ns later no signal can be seen. In this case, the bunch purity is $2.3 \cdot 10^4$.

Synchronous phase shift studies

To study the synchronous phase shift of a bunch, its arrival time relative to the RF is determined. Usually, this is done using a streak camera (SC) which allows a precise measurement of the longitudinal bunch profile and its arrival time [67]. As the TCSPC histogram represents the arrival time distribution of single photons, this technique can be used as well to study the arrival times [48].

For the determination of the arrival time, usually Gaussian curves are fitted to the peaks in the histogram. Even if the diffusion effects inside of the SPAD are suppressed by the 400 nm band pass filter, the peaks deviate significantly from a purely Gaussian shape. As the diffusion effects inside of the detector lead to an approximately exponential decay, an exponentially modified Gaussian distribution is used for the fits. Its probability density function (PDF) is the convolution of the PDF of a Gaussian distribution and the PDF of an exponential distribution.

Mostly used in chemistry for the analysis of asymmetric chromatographic peaks [68], such a distribution is characterized by the mean $\tilde{\mu}$ and width $\tilde{\sigma}$ of the precursor Gaussian and the time constant $\tilde{\tau}$ of the precursor exponential. Its PDF can be written as [68, Eq. (2)]

$$f_{\text{EMG}}(x, \tilde{\mu}, \tilde{\sigma}, \tilde{\tau}) = \frac{1}{2\tilde{\tau}} e^{\left[\frac{1}{2}\left(\frac{\tilde{\sigma}}{\tilde{\tau}}\right)^2 - \frac{x - \tilde{\mu}}{\tilde{\tau}}\right]} \cdot \operatorname{erfc}\left(\frac{1}{\sqrt{2}}\left(\frac{\tilde{\sigma}}{\tilde{\tau}} - \frac{x - \tilde{\mu}}{\tilde{\sigma}}\right)\right) \quad (5.2)$$

with erfc as the complementary error function [69, Eq. (6.2.9)]

$$\operatorname{erfc}(x) = 1 - \frac{2}{\sqrt{\pi}} \int_x^{\infty} e^{-t^2} dt. \quad (5.3)$$

As this function cannot be determined analytically, a numerical approximation is required. In the scope of this thesis, the approximation proposed in [69, p. 221] is used. For the fit, the PDF is rescaled and a constant is added for the background level. The bunch arrival time τ is determined from the first statistical moment which is given by the sum of the Gaussian mean value $\tilde{\mu}$ and the exponential time constant $\tilde{\tau}$:

$$\tau = \tilde{\mu} + \tilde{\tau}. \quad (5.4)$$

Compared to a pure Gaussian, fitting such a function leads to better results. This is illustrated in Fig. 5.7.

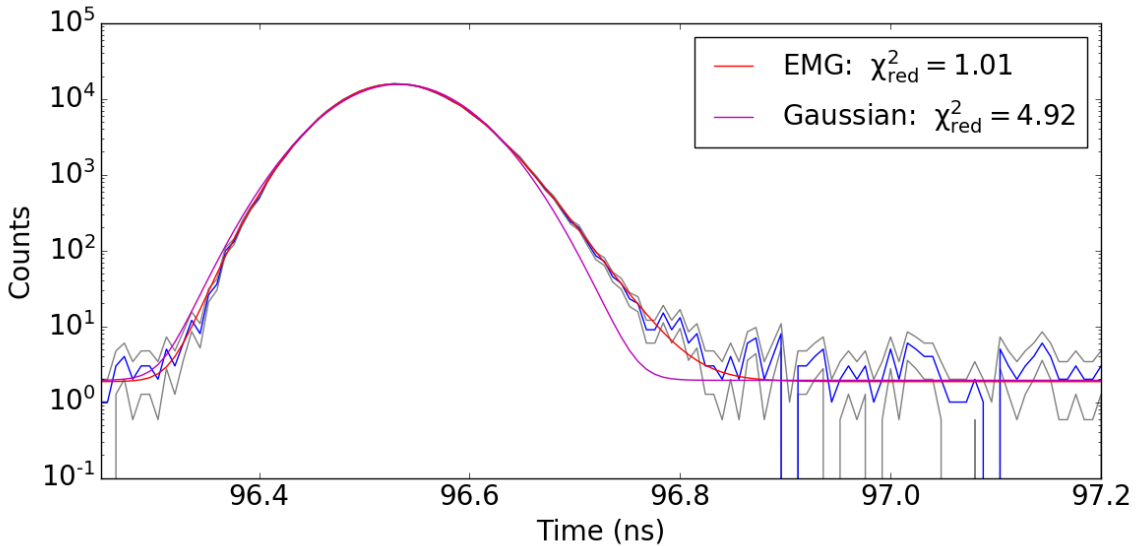


Figure 5.7.: Peak of a raw data histogram (blue) and the corresponding fits using an exponentially modified Gaussian (EMG, red) and a pure Gaussian curve (blue) (published in [70, Fig. 2]).

The better performance is quantified by the value for the reduced chi-squared χ_{red}^2 (1.01 for the exponentially modified Gaussian, while it is 4.92 for the purely Gaussian), but also a comparison by eye shows, that the exponentially modified Gaussian reproduces the shape of the peaks better.

As alternative to such a fit, the statistical moments can be calculated to determine the arrival times. Nevertheless which method is used (fitting or statistical moments), the uncertainties are depending on the the statistics. As higher the photon rate and thus the counts per bin, as lower is the measurement error on the arrival time determination. For the bunch illustrated in Fig. 5.7, this is summarised in Table 5.2.

Table 5.2.: Arrival time error σ_τ for one bunch and different photon count rates.

Photon rate	(counts/s)	$1.0 \cdot 10^5$	$1.3 \cdot 10^3$
Fit	σ_τ (ps)	0.45	2.65
Statistical moments	σ_τ (ps)	0.49	1.14

There, the comparison of the arrival times shows, that the higher photon flux and thus the better statistics clearly reduces the error on the arrival time determination. While fitting leads to slightly better results for high count rates, the statistical analysis seems to be more suitable for low count rates. This has the following reasons:

- For the fit empty bins are problematic as their errors are – according to Poisson’s statistics – zero. If the measurement errors are taken into account for the fit, these empty bins will be weighted zero. In addition, they will lead to infinite contributions to the reduced chi-squared χ_{red}^2 :

$$\chi_{\text{red}}^2 = \frac{1}{N_{\text{DOF}}} \sum_{i=1}^N \left(\frac{y_i - f(x_i)}{\sigma_i} \right)^2. \quad (5.5)$$

It is calculated from the difference between the measurement data y_i and the fit $f(x_i)$ with σ_i as measurement error.

As a consequence, the error for empty bins is set to 1 and thus overestimated. For high count rates with only a few empty bins, this is not an issue, but for low count rates with a relatively large number of empty bins this leads to an underestimation of χ_{red}^2 . As the error on the fit parameters scales with $1/\chi_{\text{red}}^2$, this lead to an overestimation of the measurement error.

Figure 5.8 shows the data set for the low count rate in Tab. 5.2 and the corresponding fit. While the reduced chi-squared is *too* small, the fit still gives a reasonably good description of the data.

- For the statistical moments, empty bins besides the peak regions are not a problem. For an increasing noise level, the contributions from these background bins increase as well. As a consequence, the analysis range has to be chosen very carefully to prevent a distortion of the mean value.

In the following, the method based on fitting an exponentially modified Gaussian distribution is used. This allows the tracking of the arrival time τ with respect to the bunch current to determine the synchronous phase shift. This can be used to study the resistive part of the longitudinal impedance (see Sec. 4.2.1).

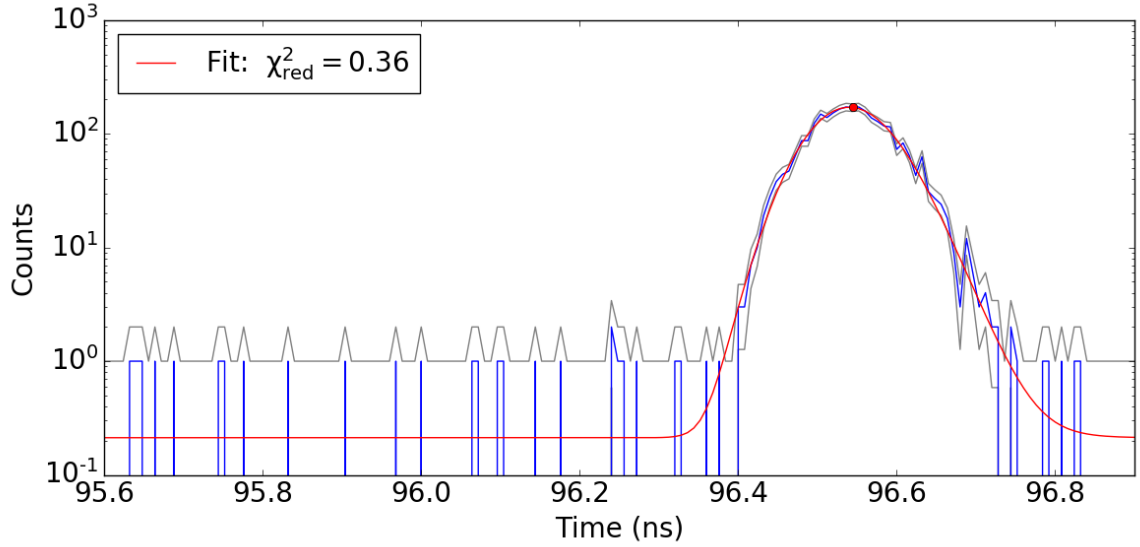


Figure 5.8.: Bunch peak recorded using TCSPC and an exponentially modified Gaussian curve fitted to the data (red). The grey lines depict the error on Poisson's statistics, for the empty bins it is set to 1 which also leads to an underestimation of χ_{red}^2 .

5.2. Fast-gated intensified camera

The energy spread is an important parameter for the investigation and understanding of the micro-bunching instability. While it cannot be directly measured, it can be studied by measurements of the horizontal bunch size in a dispersive section of the accelerator. There, the horizontal bunch size σ_x and the energy spread σ_δ are related by Eq. (2.46)

$$\sigma_x = \sqrt{\beta_x \epsilon_x + (D\sigma_\delta)^2} \quad (2.46)$$

with the dispersion D , the horizontal emittance ϵ_x and the horizontal beta function β_x at the radiation source point. At the KARA VLD port, an FGC is used to measure the horizontal bunch profile with a single turn resolution.

5.2.1. Experimental setup

The experimental setup was designed and commissioned as the scope of a Master's thesis [71]. The design is based on previous works [19, 20] and consists of a commercially available camera (Andor iStar 340T [72]) with effectively 1200 x 512 pixels and a fast rotating mirror with a galvanometric drive. For focussing and shaping the light beam, a sequence of two off-axis paraboloid mirrors and two cylindrical lenses is used, see Fig. 5.9.

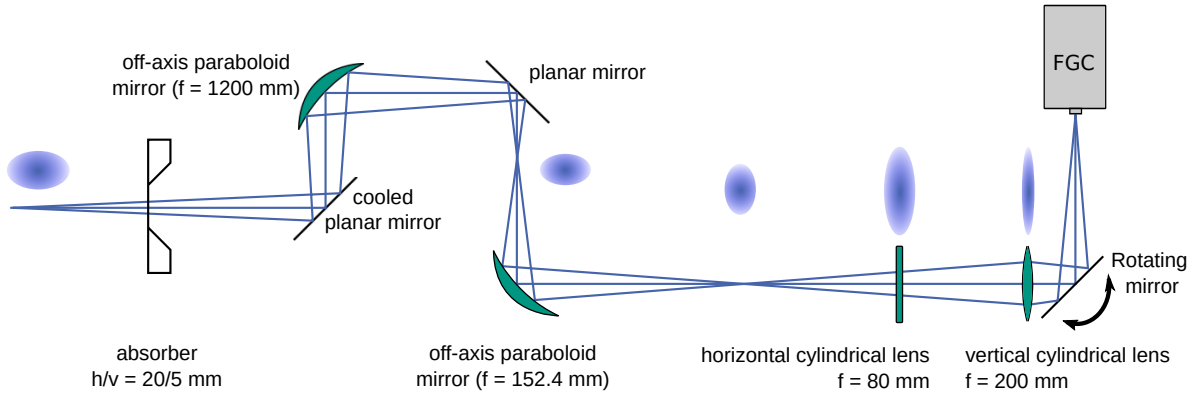


Figure 5.9.: Scheme of the optical setup at the FGC: The light from the source point passes through a rectangular absorber, is reflected upwards at the first planar mirror and then focussed using the first off-axis paraboloid mirror. After the second planar mirror it hits the second off-axis paraboloid mirror before it passes a sequence of two cylindrical lenses and hits the rotating mirror reflecting the light onto the camera (adapted from [73, Fig. 1]).

In addition to the focussing, the light beam is rotated by 90° and thus the y-axis on the camera corresponds to the horizontal plane of the electron beam and vice versa. In the following, the terminus *horizontal* and *vertical* always refers to the coordinate system of the electron beam. The nominal magnification (for a static source at the image source point) in the horizontal plane is 2.6, while for the vertical plane it is 0.3. In the vertical plane, the resolution Δ_y is defined by the absorber [74, Eq. (24)]

$$\Delta_y = L \frac{\lambda}{a}. \quad (5.6)$$

With the distance L between source and absorber (1600 mm), its width a (5 mm) and the wavelength λ (400 nm), the vertical resolution becomes $\Delta_y = 126 \mu\text{m}$. As a consequence, studies of the vertical beam size are not possible as typical vertical beam sizes are below this value. To overcome the diffraction limit in the vertical plane, an additional double slit would be required to apply interferometric measurement techniques as demonstrated in [75].

In the horizontal plane, the resolution is limited by the *depth of field* effect [74], which also later taken into account for the optical simulation of the imaging process (see Sec. 5.2.3). According to [74, Eq. (37)], the horizontal resolution Δ_x can be calculated as

$$\Delta_x = \left(\frac{3}{4\pi} \right)^{2/3} \lambda^{2/3} R^{1/3}. \quad (5.7)$$

Here, the data for the VLD port lead to $\Delta_x = 37 \mu\text{m}$.

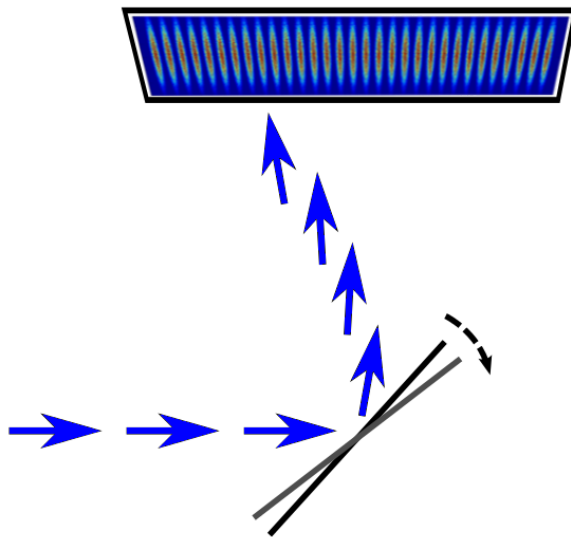


Figure 5.10.: Principle scheme of the rotating mirror. It sweeps the incoming light over the sensor of the camera and due to the gating during this rotation single turn images of the bunch are placed on the sensor [73, Fig. 3].

With the ability to switch the image intensifier of the camera on and off within 2 ns (*gating*), the camera can be used to pick one bunch out of a multi-bunch fill. The rotating mirror sweeps the incoming light over the sensor and in combination with the gating, this enables the tracking of the horizontal bunch profile for a certain number of turns, see Fig. 5.10.

With the KARA revolution frequency of 2.7 MHz, the maximum repetition rate of the gate allows to resolve every 6th turn. Such a very fast gating also requires a fast mirror sweep to resolve the single *spots* on the sensor, where each of these spots is a single turn image of the bunch. The saturation speed of the mirror driver further reduces this number and therefore, a minimum gate separation of 10 turns is reasonable. The sensor size is sufficient to place up to 80 spots on it. The limited number of data points is a drawback as one has to choose between a good temporal resolution covering only a small time range or a large time range at the expense of reduced temporal resolution. One raw image acquired using the FGC is plotted in Fig. 5.11. In this particular case, 55 spots were recorded, each separated by 24 turns ($\approx 8 \mu\text{s}$). To get the horizontal bunch size and thus the energy spread for each spot, a dedicated data analysis scheme was developed and tested successfully as it is discussed in the following.

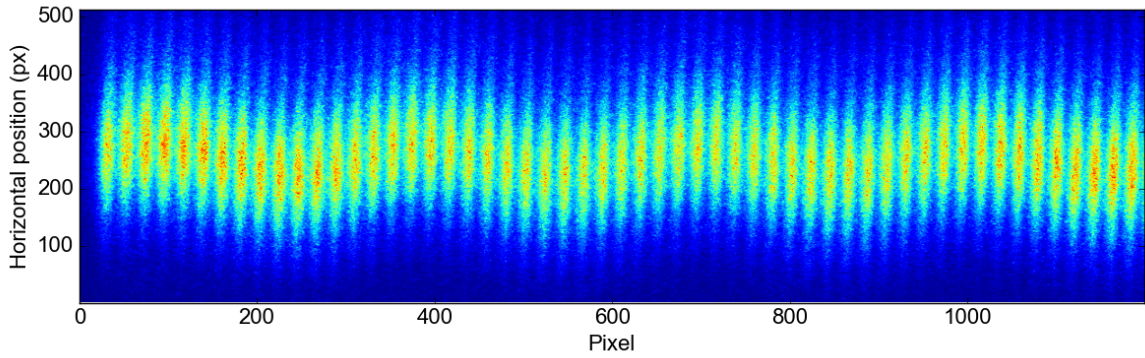


Figure 5.11.: FGC raw image showing horizontal images of the same bunch for every 24th turn. The sinusoidal modulation of the spots is due to the synchrotron oscillation.

5.2.2. From the energy spread to the spot size

As stated above, the FGC setup is intended for studies of the energy spread. While Eq. (2.46) describes the coupling between the energy spread and the horizontal bunch size σ_x using the optics parameters D , β_x and ϵ_x , the characteristics of the imaging system are described by the so-called filament beam spread function (FBSF) and the horizontal magnification m_{hor} . The FBSF can be seen as an equivalent to the point spread function (PSF) that has been extended to a moving point-like source [76]. Thus, the final image is the convolution of the FBSF with the charge distribution.

The resulting work-flow from the energy spread to the FGC spot size is illustrated in Fig. 5.12.

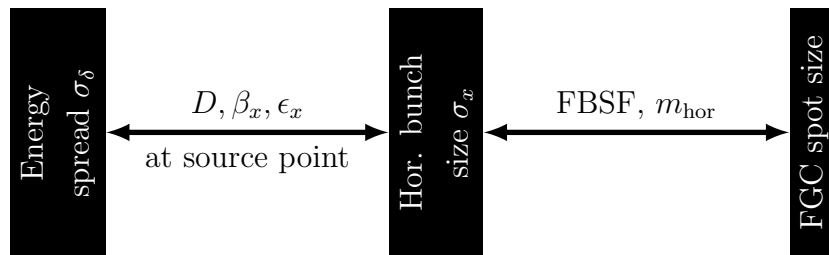


Figure 5.12.: Illustration of the relation between the energy spread and the spot size on the FGC.

For quantitative studies of the energy spread, D, β_x, ϵ_x at the imaging source point as well as the FBSF and the magnification m_{hor} are required. To get the optics parameters at the imaging source point, a simulation model of the accelerator that is based on measurements is used (see Sec. 7). For the FBSF, the imaging system has to be investigated using simulations.

5.2.3. Data analysis

The imaging system for the FGC consists of a set of two planar and two off-axis paraboloid mirrors as well as two cylindrical lenses (see Fig. 5.9). Off-axis paraboloid mirrors are used since the VLD port was originally designed for longitudinal bunch diagnostics using a streak camera (SC) [39]. For transverse imaging, which is the case here, off-axis paraboloid mirrors are not perfectly suited because they induce image distortions for a divergent light source. In addition, it has to be taken into account, that the bunch is moving during the acquisition process in the same plane its profile is determined. Thus, the profile seen by the observer is the superposition of many profiles. This effect – also referred to as *depth of field* – is a common problem for horizontal beam size measurements using synchrotron radiation [77]. For an optical system based on lenses, this can be treated analytically [74, 78]. This distortion can be seen as kind of a motion blur that also occurs in photography if the object moves during the image acquisition. The normal solution to solve this would be to reduce the exposure time. At the FGC, this is not possible since the 1.55 ns FWHM used for the measurements are the technical minimum. Another possibility to reduce the *effective* exposure time would be to decrease the horizontal width of the absorber (currently: 20 mm). Apart from the fact that this requires a completely new dipole chamber, it would also decrease the resolution limit because for a smaller aperture diffraction effects will start to play a role.

For the FGC setup with its two off-axis paraboloid mirrors, the imaging process is studied by (numerical) simulations using the software OpTaliX [79]. In this simulation, the different optical elements are represented by optical planes with the corresponding surface curvatures, diffraction indices and reflection coefficients. Ray-tracing allows illumination studies using extended sources with e.g. a Gaussian shape. The movement of the bunch in the horizontal plane during the imaging process can be studied as well. For this, a sequence of images from a source moving on a circular trajectory through the imaging source point is simulated with the single image summed up to form the final image. For three time steps during the acquisition process, this is illustrated in Fig. 5.13.

This superposition is described by the FBSF which takes the particularities of the optical setup and its moving source into account.

To determine the FBSF, a point-like source that moves stepwise on a circular trajectory is imaged. As OpTaliX cannot handle such an infinitely small source, a finitely small Gaussian source is used. The second important parameter for the source is the divergence of the emitted radiation. For synchrotron radiation, the angle of maximum

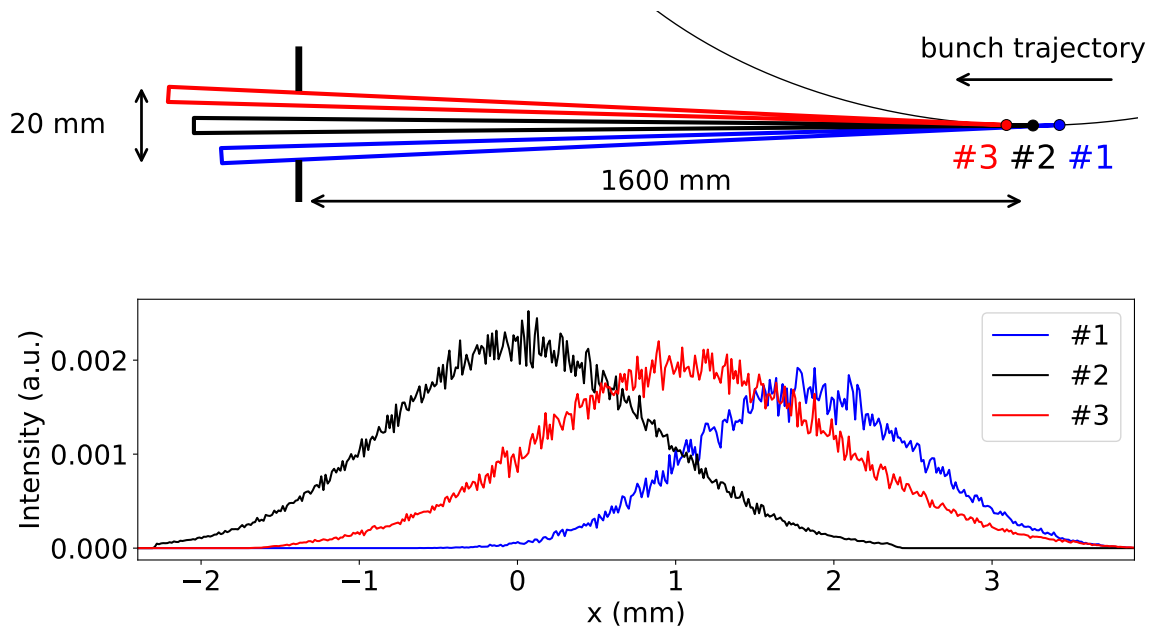


Figure 5.13.: Principle scheme of the profile superposition at the VLD port: The Gaussian shaped bunch is moving on a circular trajectory and radiating, the vertical black lines depict the absorber. For three time steps, the radiation cones are illustrated in blue, black and red. The three corresponding profiles are plotted in the bottom panel.

intensity at a given wavelength can be approximated by [80, Eq. (24)]:

$$\Theta [rad] = 1.66 \cdot \left(\frac{\lambda}{\rho}\right)^{1/3}. \quad (5.8)$$

Assuming a wavelength of 450 nm for the FGC, this leads to $\Theta \approx 0.4^\circ$ which is used for the horizontal divergence. In the vertical plane, the absorber with the height of 5 mm limits the vertical acceptance to 0.2° .

The source parameters that are used for the FBSF studies are summarized in Table 5.3, for the focal lengths and element positions in the OpTaliX simulation model the nominal values are used.

Since the VLD port is diffraction limited in the vertical plane, only the horizontal plane is taken into account. Therefore, for each simulation step, the horizontal profile in the image plane is determined by histogramming the positions of the rays at the image surface, the bin width is set to the pixel size of $13.5 \mu\text{m}$.

Finally, all histograms are summed up and normalized to get the FBSF. Systematic studies showed, that the shape of the FBSF is very sensitive to an angular deviation between the electron orbit and the optical axis when passing the imaging source plane.

Table 5.3.: Source parameters for the OpTaliX FBSF studies.

Wavelength	450 nm
Source size $\sigma_{x,y}$	1 pm
Horizontal divergence	0.4°
Vertical divergence	0.2°
Number of steps	101
Bending angle	$\pm 1.0^\circ$

This deviation is parameterised by the angle β , for three different values this is illustrated in Fig. 5.13.

To get the horizontal bunch profile from the profile of the individual spots of an FGC image, it has to be deconvolved with the FBSF. In the frequency domain, the deconvolution corresponds to the division of the two Fourier transforms. This can lead to a numerically unstable behaviour due to zero-value components in the denominator and additional noise components. There exist different methods for this inverse filtering (e.g. Wiener deconvolution), but they are relatively slow and require iterative processes and/or additional estimates of the signal-to-noise ratio (SNR). Therefore, a work-around is used to get the horizontal bunch size σ_x : It is based on the assumption that the horizontal bunch profile has a Gaussian shape or at least that a Gaussian fit can be used to get a measure for its size. To achieve this, a Gaussian curve convolved with the FBSF is fitted to the data. Thus, the fit function reads as

$$f(x, C, A, \mu_x, \sigma_{\text{spot}}) = f_{\text{FBSF}} * \left[C + A \cdot e^{-\frac{1}{2} \left(\frac{x - \mu_x}{\sigma_{\text{spot}}} \right)^2} \right], \quad (5.9)$$

where the operator $*$ denotes the convolution. Amongst the amplitude A , the horizontal position μ_x and an additional offset C , the fit gives a measure for the spot size σ_{spot} . The offset C covers the non-vanishing background counts on the FGC sensor. This ansatz was preferred to the subtraction of dedicated background images as it is robust against changes of the image intensifier settings and (thermal) long-time drifts of the pixel noise.

For the fit, also the errors on the data points are taken into account. Two contributions are considered:

1. **Pixel noise:** As the diameter of the micro-channel plate (MCP) channels is approximately twice the pixel size, a certain correlation between neighbouring pixels is expected. As an estimation of this noise contribution, the standard deviation

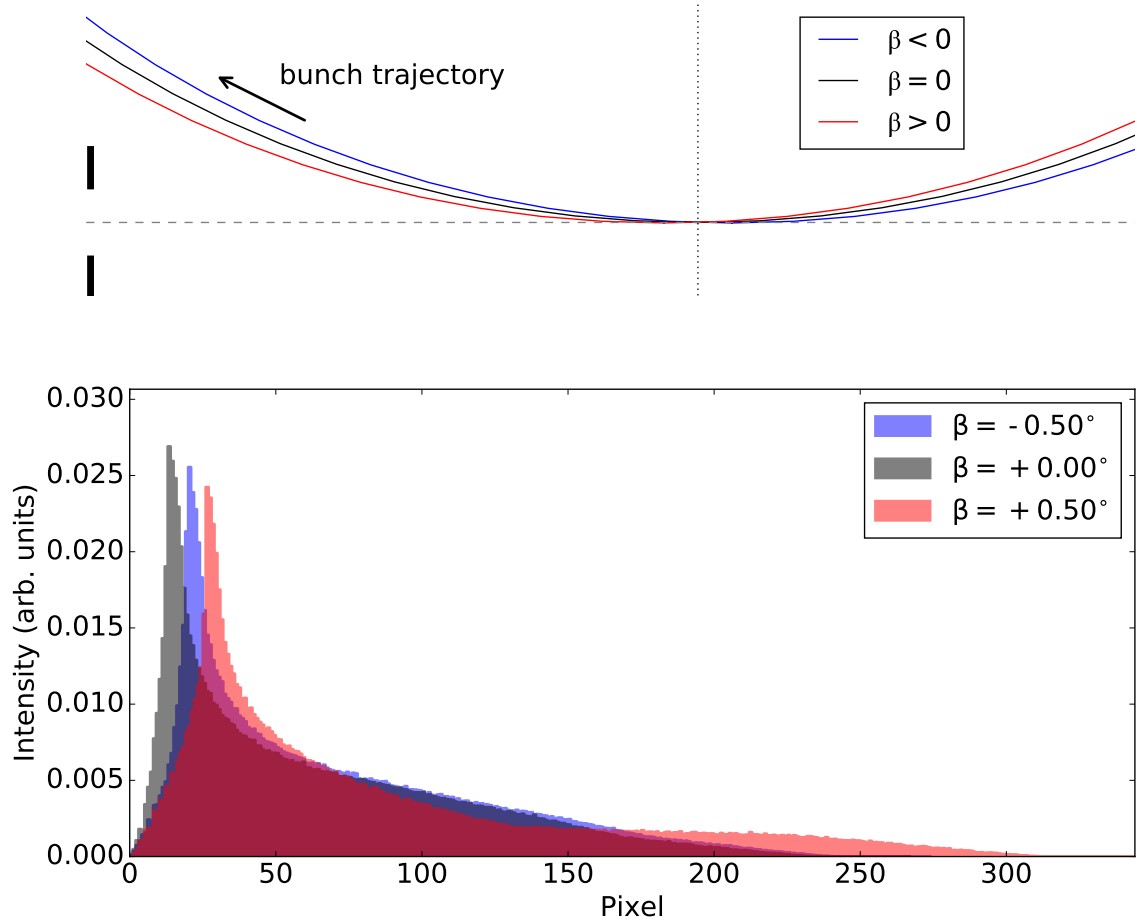


Figure 5.14.: Top panel: Illustration of the simulated electron trajectories for different angles β between the electron orbit and the optical axis, which is depicted by the horizontal dashed line. The dotted line is the imaging source plane. Bottom panel: Three FBSF determined from OpTaliX simulations for different β .

σ_{Pixel} over the four neighbouring pixels (two in each direction) is calculated for each pixel. In addition, also a possible electric cross-talk between the pixels is covered.

2. **Poisson statistics:** The counting error per pixel is given by

$$\sigma_{i_{\text{Poisson}}} = \sqrt{n_i}.$$

Thus, for each pixel the error σ_i can be calculated as

$$\sigma_i = \sqrt{\sigma_{i_{\text{Pixel}}}^2 + \sigma_{i_{\text{Poisson}}}^2}. \quad (5.10)$$

The error on the resulting fit parameters is calculated from the covariance matrix U^{-1}

and the reduced chi-squared χ_{red}^2 [81]:

$$\sigma_{p_i} = \sqrt{\frac{U_{ii}^{-1}}{\chi_{\text{red}}^2}}. \quad (5.11)$$

To benchmark the performance of the data analysis, only measurements below the bursting threshold can be taken as reference as only there the energy spread follows a Gaussian distribution (see Eq. (4.27) in Sec. 4.3). The drawback is, that for these bunch currents the signal intensity is relatively low, however there is no (better) reference for this benchmarking.

Concerning the choice of the FBSF, the best performance is achieved by setting β to 0.5° . This seems to take the relevant deviations from the design parameters (tilts, offsets, orbit deviations) into account. It is noteworthy, that for different machine settings and beam orbits, an adjustment of this value could be required.

One example for such a fit with $\beta = 0.5^\circ$ is illustrated in Fig. 5.15.

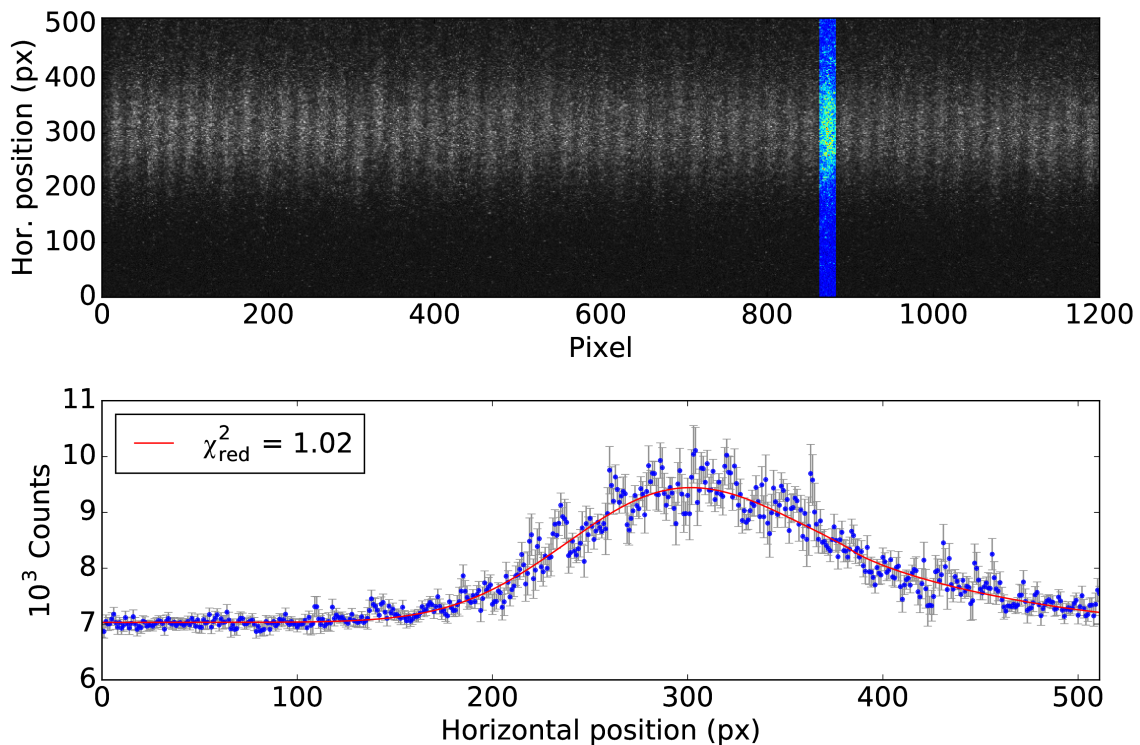


Figure 5.15.: FGC raw image in grey scale with the analysis range for one spot highlighted in color, the corresponding profile and the fit is plotted in the bottom panel.

It shows that the fit reproduces the spot profile very well, which is also supported by the reasonably good value of the reduced chi-squared.

Based on the assumptions and estimations discussed above, the fit shows an excellent performance. For four different machine optics, this is illustrated in Fig. 5.16.

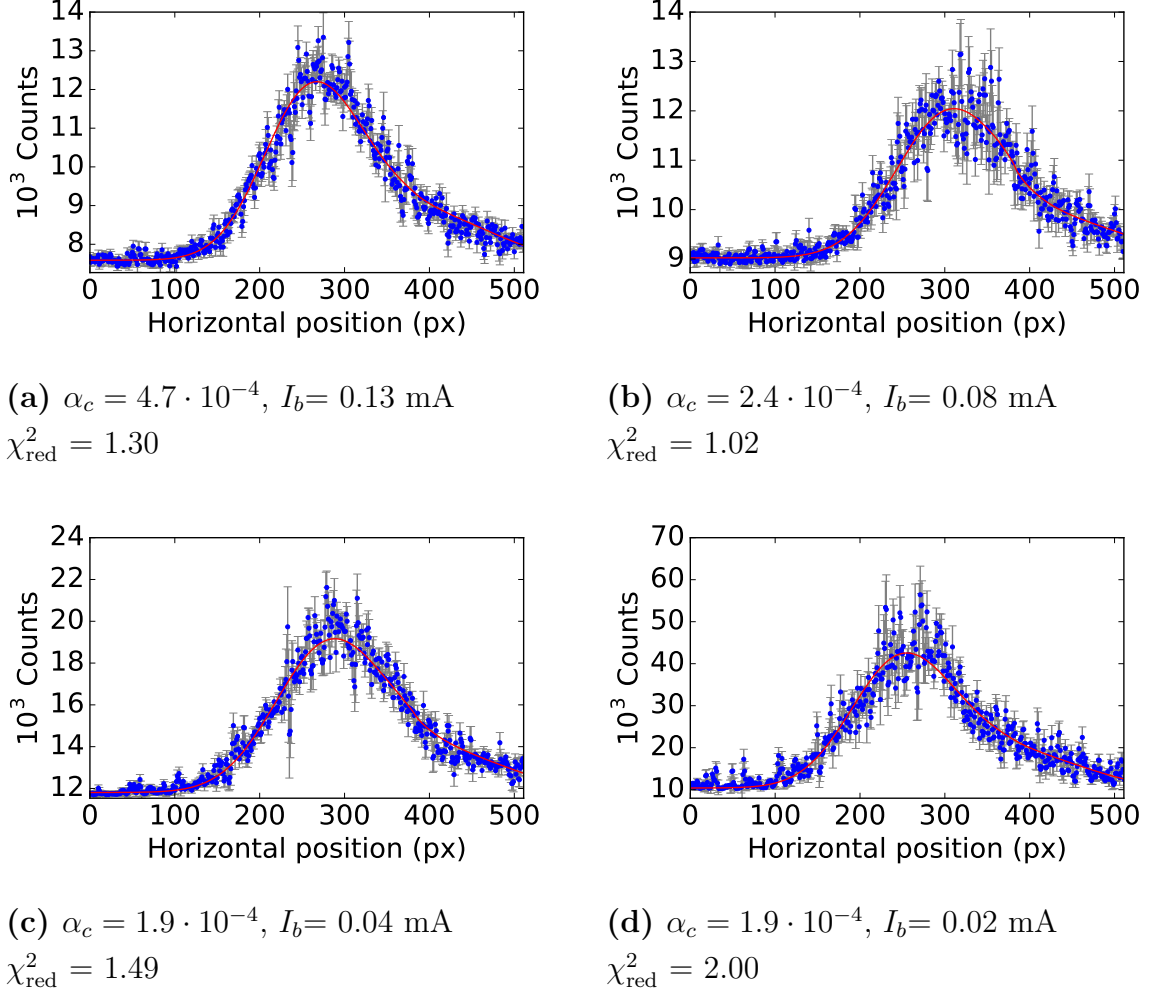


Figure 5.16.: Comparison of horizontal spot profiles with the corresponding fits for different machine optics.

In all cases, the reduced chi-squared χ_{red}^2 has a reasonable magnitude showing that the model used for the fit agrees quite well with the data and the assumed errors on the data points.

The last step in the data analysis chain is the conversion from the spot size σ_{spot} , which is given in units of pixel, to the horizontal bunch size σ_x . To do so, the pixel size σ_{pixel} as well as the horizontal magnification m_{hor} have to be taken into account:

$$\sigma_x = \frac{\sigma_{\text{spot}} \cdot \sigma_{\text{pixel}}}{m_{\text{hor}}}. \quad (5.12)$$

According to the data sheet, the FGC has a pixel size of $13.5 \mu\text{m}$. The horizontal magnification is given by the optical setup and is defined by the positions of the three focussing elements: the two off-axis paraboloid mirrors ($f = 1200$ mm and 152.4 mm) and the horizontal cylindrical lens ($f = 80$ mm). A precise determination of the exact positions of the elements is difficult as parts of the setup are on the inner side of the

radiation safety wall and completely shielded against background light. This uncertainty on the element position induces a relatively large uncertainty on the horizontal magnification as it is very sensitive to misalignments. As a consequence, the error on the horizontal magnification is estimated from the setup to be 0.10.

The time between two consecutive gates is a camera parameter given as integer number of turns. As discussed in [71], this value is used to assign a time separation between two consecutive spots, the absolute calibration for the synchronisation with other detector systems is discussed in Chapter 6.

This toolset now allows to determine the horizontal bunch size σ_x with a single turn resolution and a high dynamic range. Thus, it serves as a versatile tool to study the beam dynamics during the micro-bunching instability. Before these systematic studies are discussed in chapter 8, another setup for horizontal beam diagnostics is presented that has been tested successfully.

5.3. Turn-by-turn horizontal bunch size measurements

As mentioned in the previous section, the FGC has intrinsic limits due to the limited number of data points per image. This requires a trade-off between temporal resolution and acquisition time, which has to be chosen in advance to any measurement. To overcome this limitation, the KALYPSO system [82, 83] was tested at the VLD port to measure the horizontal bunch size. Such a system is foreseen as successor of the FGC.

5.3.1. Experimental setup

KALYPSO is an ultra-fast 1D line camera with 256 pixels and a maximum frame rate of 2.7 MHz. This allows turn-by-turn studies in the single bunch operation. Due to its modular design, it can be equipped with different types of sensors. For the measurements discussed in the following, a silicon detector was used. As the system was designed with focus on a high data throughput, it can operate continuously as the only limiting factors are the data transfer speed to the readout computer and its memory.

To use the system, the optical system of the FGC was adjusted: By using a flip mirror the light was coupled out before the last focussing lens. To achieve good focussing in the vertical plane, another cylindrical lens ($f = 70$ mm) was used. Fig. 5.17 shows the setup at the VLD port.

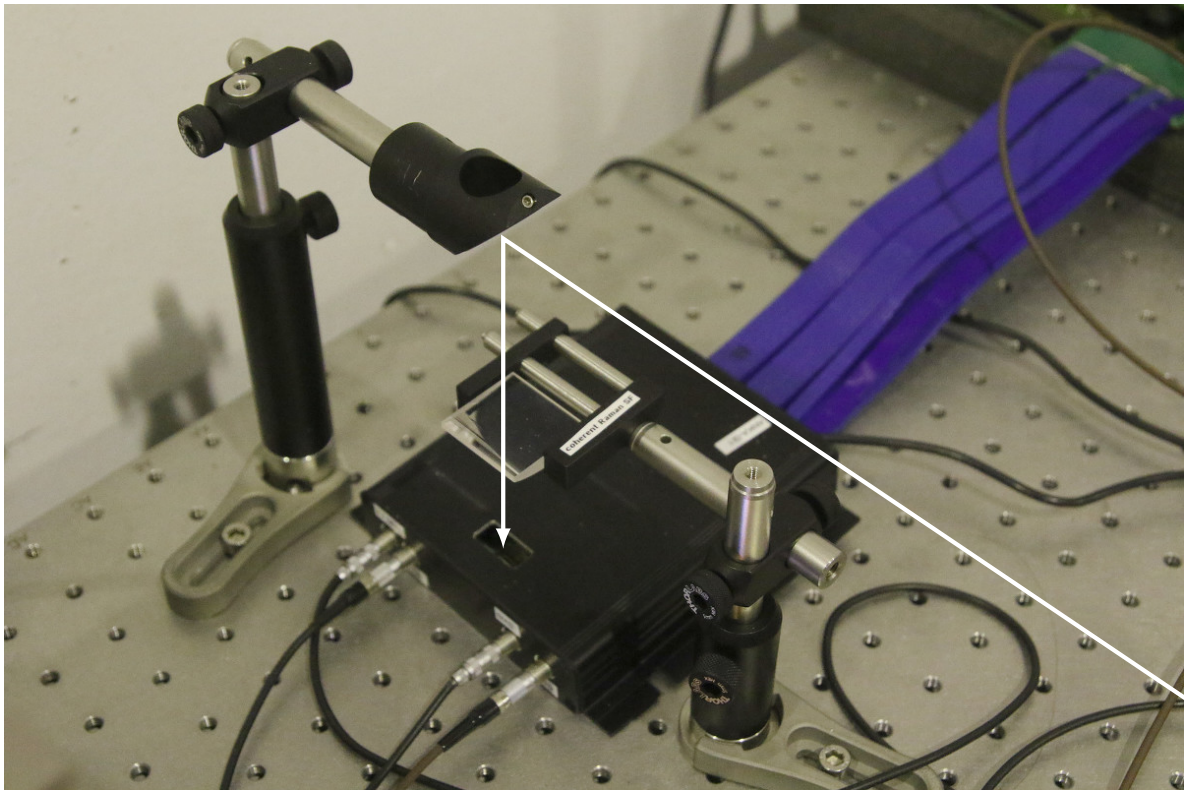


Figure 5.17.: Image of the KALYPSO setup at the VLD port. The incoherent synchrotron radiation – depicted by the white arrow – is deflected by a mirror and focussed onto the sensor by a cylindrical lens. The KALYPSO system is housed in the black metal box.

5.3.2. Data analysis

To determine the horizontal bunch size, a dedicated data analysis scheme has been developed which takes the FBSF of the setup into account. It consists of the following steps:

1. Background subtraction

At certain time stamps, background images are taken where the light from the electron beam is blocked and images for 10^5 turns are recorded. Afterwards, for each pixel the average background is calculated and subtracted from the images recorded with synchrotron radiation. Pixels where the background subtraction would lead to negative counts are set to zero.

2. Error estimation

Two contributions are assumed for the measurement error of the individual pixels:

- a) **Pixel noise:** To account for an eventual cross-talk between neighbouring

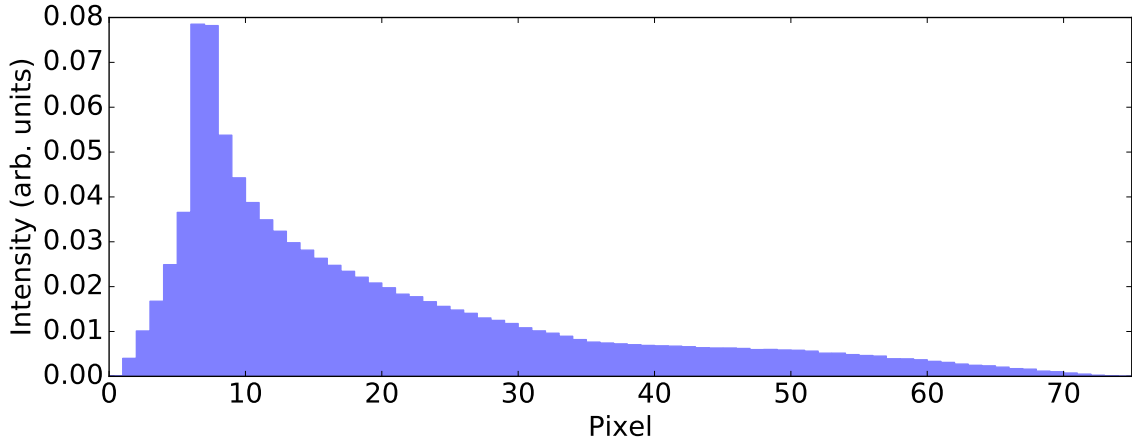


Figure 5.18.: FBSF for the KALYPSO setup simulated using the software OpTaliX.

pixels, the standard deviation σ_{Pixel} over the nearest neighbour pixels is calculated for each pixel.

b) **Poisson statistics:** The absolute counting error per pixel is given by

$$\sigma_{i\text{Poisson}} = \sqrt{n_i}.$$

Thus, for each pixel the error σ_i can be calculated as

$$\sigma_i = \sqrt{\sigma_{i\text{Pixel}}^2 + \sigma_{i\text{Poisson}}^2}. \quad (5.13)$$

As discussed for the data analysis for the TCSPC based synchronous phase shift studies, the pixel error is set to 1 for pixels with zero value errors as they would be ignored in the fitting process otherwise due to their zero weights.

3. Fitting a convolution of the FBSF with a Gaussian

As for the FGC, also here a convolution of a Gaussian with the FBSF is fitted to the horizontal profile. The FBSF is determined using OpTaliX with the same simulation input parameters concerning the source characteristics as for the FGC. Here, the bin width is set to $50 \mu\text{m}$ which corresponds to the KALYPSO pixel pitch. The resulting FBSF is plotted in Fig. 5.18.

Due to the background subtraction, the fitting function does not contain a dedicated background offset. Again, the error on the fit parameters is calculated from the scaling of the diagonal elements of the covariance matrix with the reduced chi-squared.

In Fig. 5.19, one horizontal profile is plotted together with the corresponding fit.

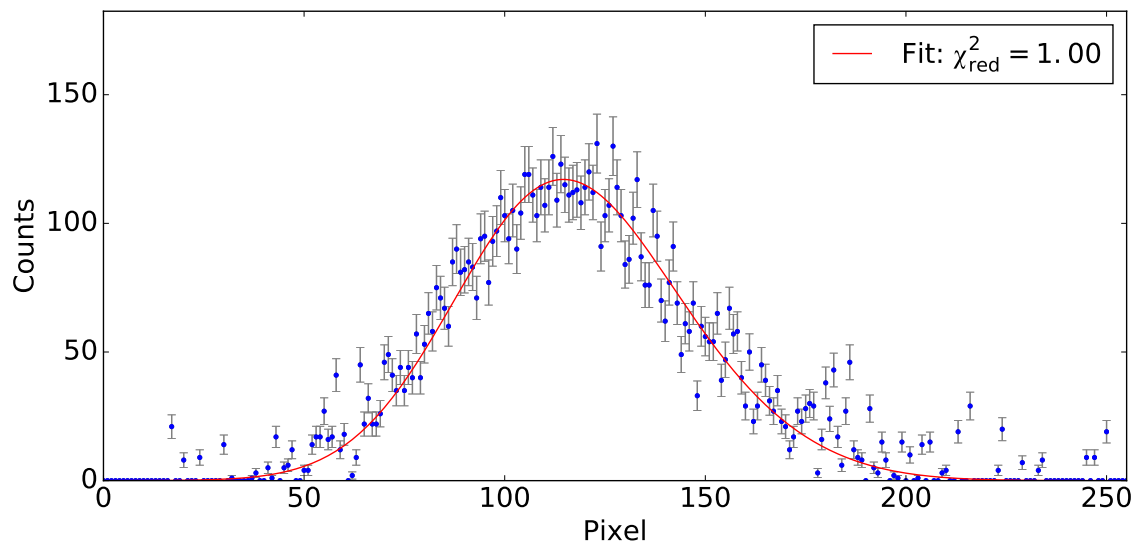


Figure 5.19.: Background subtracted horizontal bunch profile recorded using the KALYPSO system and the corresponding fit to the data. As the imaging process induces a distortion of the profiles from a Gaussian shape, the FBSF is taken into account for the fit as well.

The value for the reduced chi-squared indicates a reasonably good agreement of the fit model and the errors with the measurement data. An example picture recorded with the system is plotted in Fig. 5.20.

The top panel shows the background corrected raw image for 10^5 consecutive turns. Each column corresponds to one horizontal bunch profile and fits are applied to each of these columns. The resulting positions and sizes of the bunch are plotted in the center and bottom panel, respectively. The horizontal bunch position in the middle panel shows a synchrotron oscillation with varying amplitude including a strong rise in amplitude at 23.2 ms. This abrupt onset is used as timing reference for the synchronisation with other detector systems. The horizontal bunch size in the bottom panel shows significant superimposed noise. Therefore, profile histograms are applied to the data which are shown as blue dots with the corresponding standard deviation as vertical error bars.

To benchmark this data analysis scheme, the determined horizontal bunch size can be compared to the ones measured using the FGC for identical machine settings and a comparable bunch current ($I_b = 0.8$ mA). Such a benchmark is shown in Fig. 5.21.

The two curves have approximately the same magnitude and modulation period length. As they are from two completely different fills, they are manually aligned along the time axis to enhance the visibility.

As it is the case for the KAPTURE system, KALYPSO allows a quasi-instantaneous

start of the recording and does not need a certain preparation time as discussed in Sec. 6.2. Therefore, it is a very promising tool, also due to its long acquisition time with single turn resolution, as it is further discussed in Sec. 8.1.3.

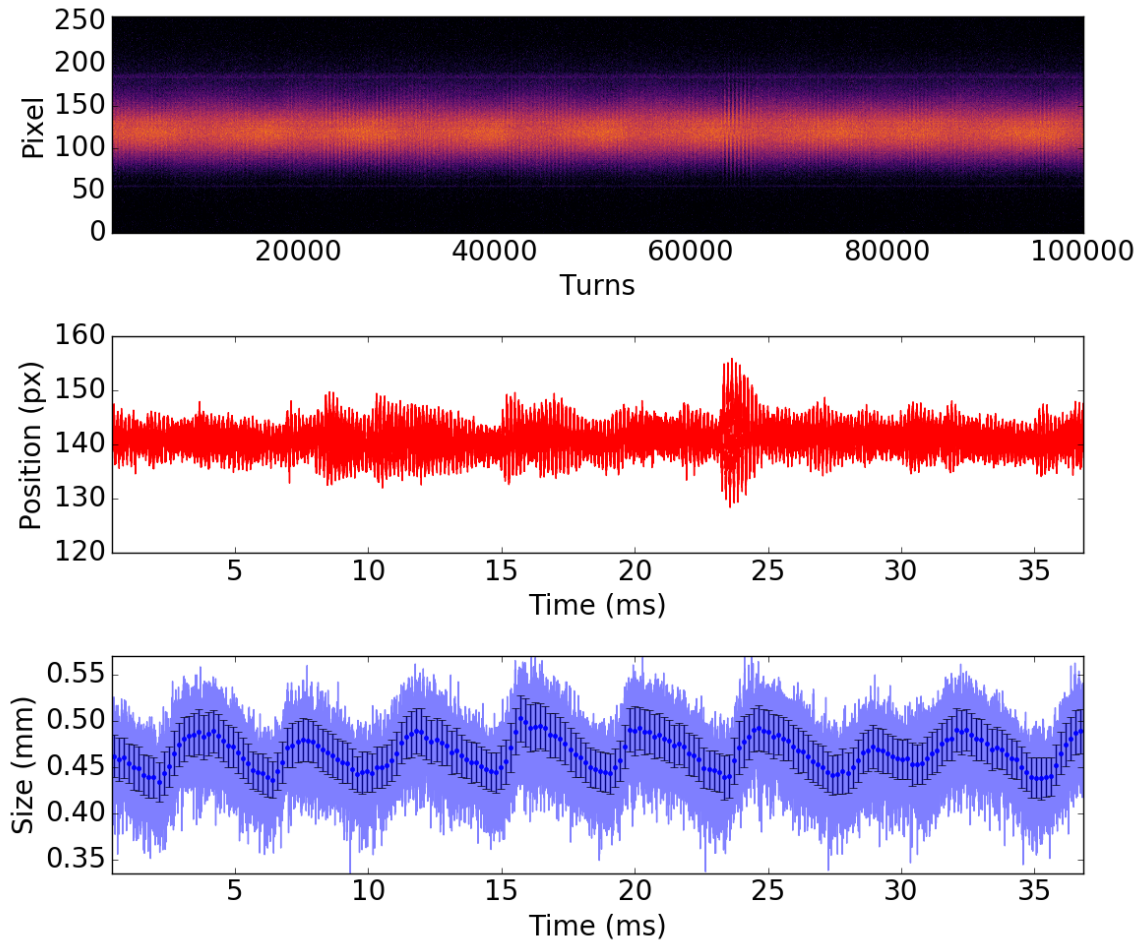


Figure 5.20.: Image recorded using the KALYPSO system. The top panel shows the background corrected raw image while the center and bottom panel show the corresponding bunch position and sizes. To overcome the noisy structure of the signal, a profile histogram was applied to the bunch size. The horizontal bunch position in the middle panel shows a synchrotron oscillation with varying amplitude, including an abrupt onset at 23.2 ms.

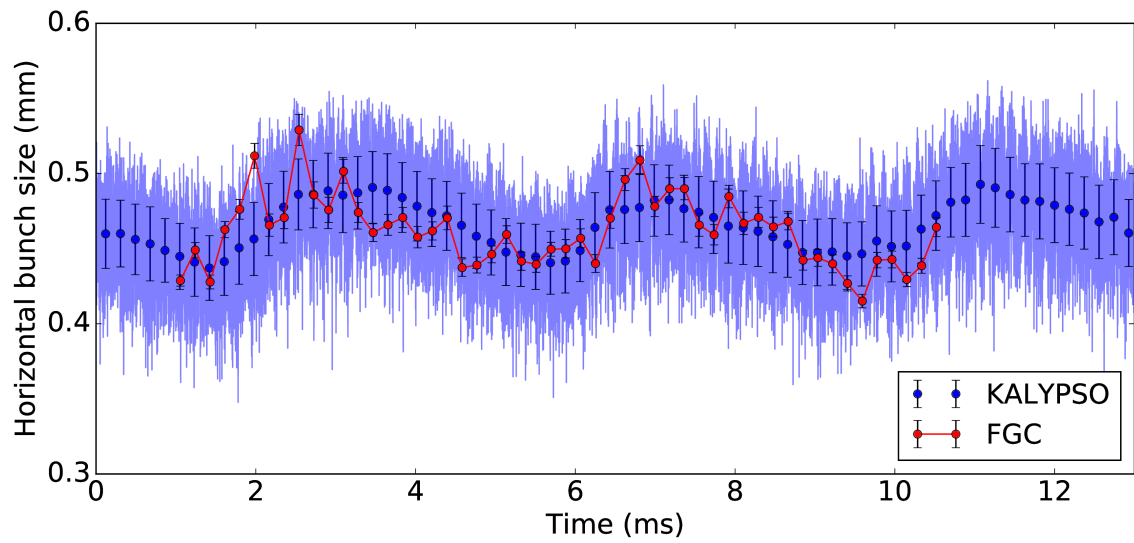


Figure 5.21.: Horizontal bunch size measured using KALYPSO with a profile histogram applied to the data (blue) and the FGC (red) for identical machine settings and bunch currents. For better visibility, the two curves were aligned along the time axis. As a guide to the eye, the data points from the FGC are connected by lines.

6. Synchronisation of the FGC setup

To get insight into the dynamics of the bursting behaviour of a bunch, it is crucial to measure its different parameters synchronously with a single-turn precision. To achieve this, a hardware based synchronisation scheme was set up and tested. In this chapter the system will be presented and the integration of the fast-gated intensified camera (FGC) into this scheme will be discussed as there are setup-intrinsic delays to be taken into account.

6.1. Overview

The simplest way to measure simultaneously several bunch parameters would be to feed the signals from the different detector systems into one common data acquisition (DAQ) system, e.g. an oscilloscope. This is suitable if all devices are located close to each other or if the storage ring has a quite compact design (e.g. SURF [5]). In case of KARA, this is not directly possible due to several reasons:

1. The systems for optical and coherent synchrotron radiation (CSR) detection are located at different positions around the storage ring:
 - The FGC setup and a KALYPSO system [82, 83] at the visible light diagnostics (VLD) port.
 - KAPTURE [52, 53] in combination with fast THz detectors for CSR studies at the IR2 beamline.
 - An oscilloscope using the segmented mode with fast THz detectors for CSR studies at the IR1 beamline.
2. At all these systems, a dedicated post-processing of the data is required, as e.g. the FGC delivers 2D images, while the KAPTURE system provides – in the multi-detector mode – for each detector one data point per bunch and turn.

Thus, the acquisitions of the systems have to be aligned temporally to enable later on correlation studies between the derived parameters like CSR intensity and energy spread. To get such a common time-axis for all experiments, a precise synchronisation of the systems is required. To achieve this, a dedicated hardware synchronisation scheme

is used that provides a set of triggers starting the acquisition of all systems at the same time. Therefore, the different setups have to be investigated with regard to their intrinsic delays occurring between the triggering and the first measurement.

KAPTURE and KALYPSO use a hardware technology with continuous sampling, independent of the coupled detectors. Thus, the acquisition trigger starts the storage of the data into the memory and therefore a quasi-instantaneous start of the recording is achieved. For the FGC setup, this is different: Due to the measurement controls and the inertia of the mechanical components, a certain time is needed for the first sample to be recorded.

6.2. FGC setup hardware delays

Due to its layout consisting of the camera and the fast rotating mirror, the FGC setup has some intrinsic mechanical and electrical delays. The mechanical ones are due to the inertia of the rotating mirror, while the electrical delays are induced by the amplifier of the mirror voltage driver. The process diagram is illustrated in the appendix, see Fig. A.4.

When a measurement process is started, the setup is going through the following steps:

1. Depending on the set value for the measurement time range, a linear voltage ramp with a certain slope for the mirror is calculated by the waveform generator [84].
2. When this linear voltage ramp starts, the mirror voltage driver induces a delay between the input signal and the resulting mirror position that can be measured using an oscilloscope, in case of the setup used here it was determined to be 130 μs .
3. To protect the sensor from overexposure, the mirror has a holding position in which the light passes the sensor and thus the light spot has to be driven first onto the sensor to be recorded. At a certain point of the voltage ramp, the light spot reaches the sensor. This point is defined by a threshold voltage and when this voltage is reached, a logical signal is sent by the second output of the waveform generator to the trigger logic unit (TLU). This unit acts as a gate for the incoming trigger pulses that are now sent to the camera to trigger the gating of the image intensifier.

These delays can be determined by measurements, an example for such a measurement is illustrated in Fig. 6.1. By compensating for these delays, the setup can be integrated into the hardware synchronisation scheme.

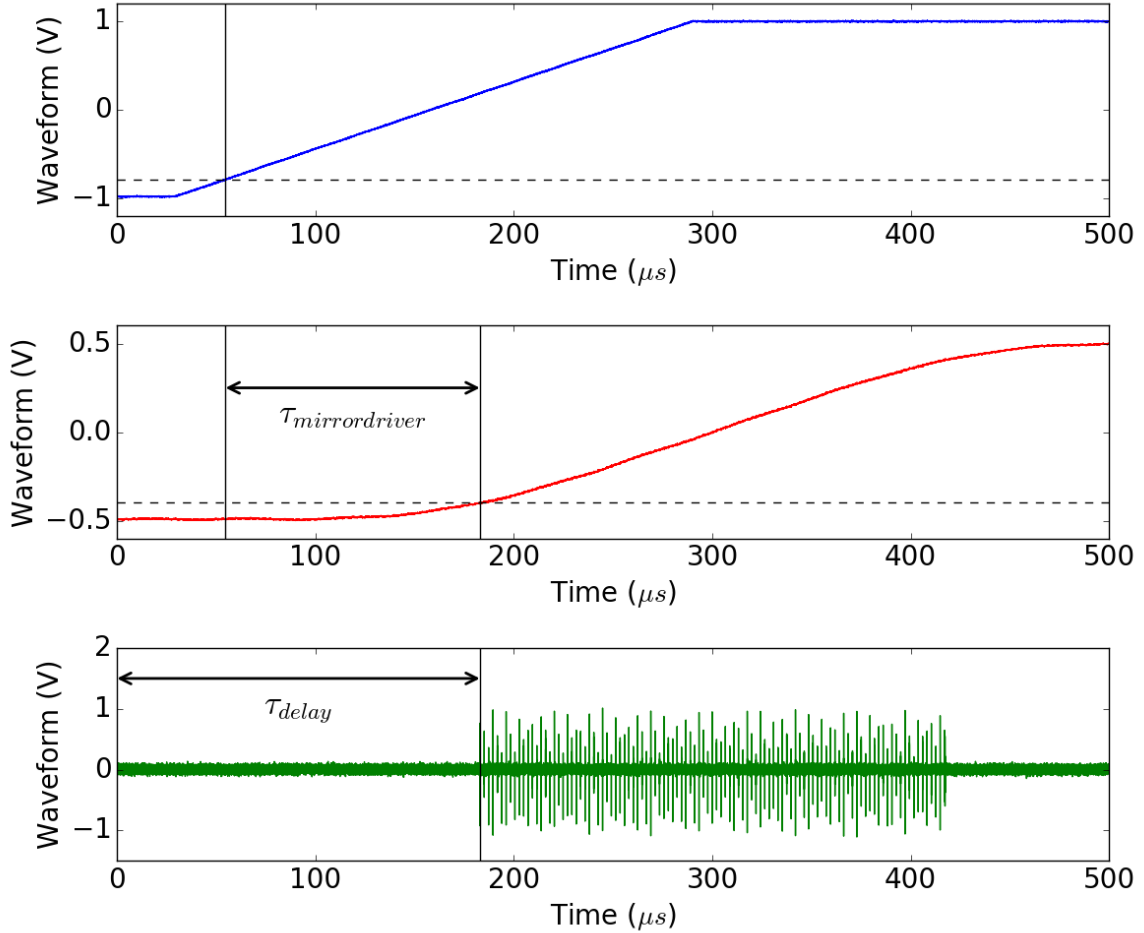


Figure 6.1.: Delay measurements on the FGC. The top panel shows the signal from the waveform generator that feeds the mirror driver. The resulting mirror position voltage is shown in the middle panel. A delay relative to the waveform generator signal ($\tau_{\text{mirrodriver}} \approx 130 \mu\text{s}$), as well as the non-linear start and end of the ramp can be seen. The bottom panel shows the corresponding pickup signal from the camera gate. Opening the gate leads to a sharp spike in the pickup signal. In this particular case, the first gate used for measurements comes approx. $180 \mu\text{s}$ after the starting trigger of the measurement at $t=0 \mu\text{s}$.

6.3. Hardware synchronisation scheme

The hardware synchronisation scheme allows simultaneous measurements of the different bunch properties on a single turn base [85]. This scheme uses as commercial timing system that is based on one event generator (EVG) and several event receivers (EVRs) [86]. It provides a common measurement trigger (referred as *physics trigger*) that is sent to all measurement stations. It is a so-called *arm trigger*, that does not start the measurement directly as this is done with the next incoming trigger pulse from the KARA revolution clock. This trigger defines the starting point of a common time-axis for all experiments. A principle schematic is illustrated in Fig. 6.2.

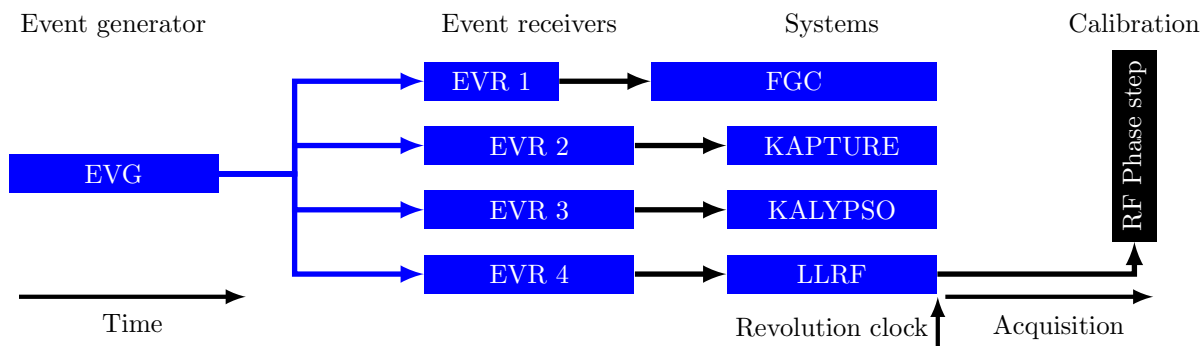


Figure 6.2.: Schematic of the synchronisation principle based on the KARA timing system consisting of one EVG and several EVRs located at the different measurement systems. The intrinsic delay times of the system are illustrated by the different widths of the boxes and are compensated by the timing of the individual EVRs. The synchronisation is calibrated by applying a triggered RF phase step using the low-level RF (LLRF) system (schematic published in [85, Fig. 2]).

The intrinsic delays of the setups are indicated by the different widths and positions of the corresponding boxes. As discussed before, this is especially the case for the FGC. It is compensated by triggering the preparation process a certain time in advance of the other measurement setups included in the synchronisation scheme.

6.4. Calibration of the synchronisation

The studies of the setup intrinsic delays at the FGC setup and the corresponding compensation in the synchronisation scheme allows a coarse synchronisation of the FGC with respect to KAPTURE and KALYPSO. For a fine calibration of the synchronisation, an additional reference signal is required. This is achieved by triggering a sudden step in the radio frequency (RF) phase using the LLRF system. This sudden step leads to the onset of a strong synchrotron oscillation and the signature of this oscillation

can be detected by the different detector systems. With respect to the synchronous measurement discussed later in Chapter 8.1, here the focus is set to the synchronisation between the FGC and the KAPTURE system.

For these calibration measurements, KAPTURE was used to sample the signal from a fast avalanche photo diode (APD) that is sensitive in the visible range. The longitudinal synchrotron motion of the bunch induced by the RF phase step leads also to an energy oscillation with the same frequency. This energy oscillation is transferred by dispersion into a horizontal oscillation around the imaging source point of the beam line. Therefore, the intensity of the detected incoherent synchrotron radiation is modulated with the same frequency and phase.

On the FGC, this energy oscillation is visible as well, as the source point is also in a dispersive section of the storage ring. This oscillation has the same phase as the oscillation on the incoherent synchrotron radiation sampled by the APD.

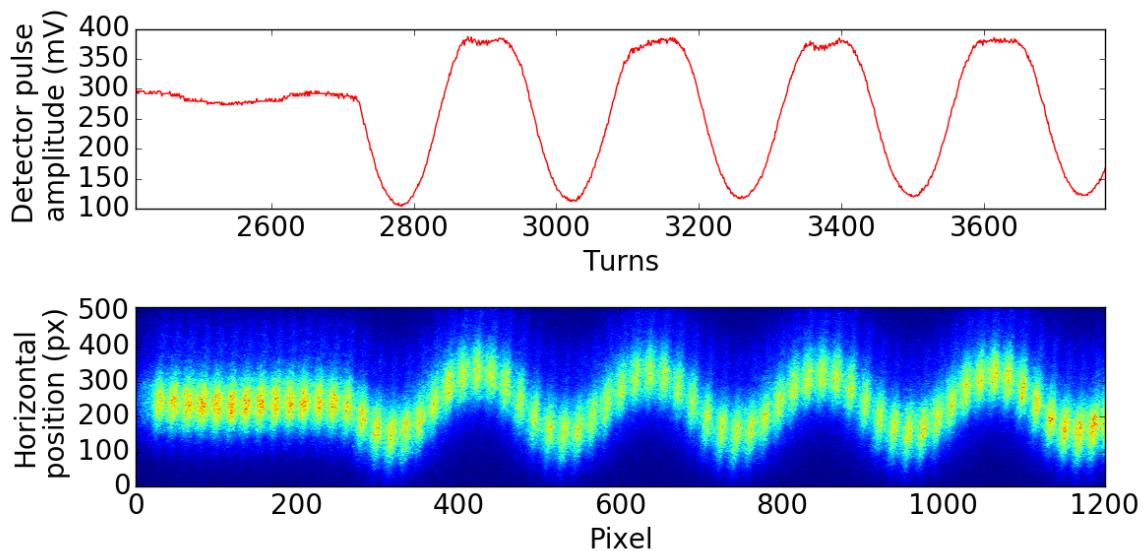


Figure 6.3.: FGC raw image (top panel) and the APD signal recorded with KAPTURE (bottom panel). The abrupt onset of a synchrotron oscillation on both panels is due to the triggered RF phase step.

An FGC raw image and the corresponding KAPTURE signal are illustrated in Fig. 6.3. Here, the signal from the APD shows deviations from an ideal sinusoidal curve with some flat tops around the upper turning points of the oscillation. It is assumed that this is an aperture effect of the optical beam path leading to spatial cut-off effects. Nevertheless, the most important feature of this measurement, the strong synchrotron oscillation, is clearly visible and can be used for the calibration.

This fine calibration consists of the following steps:

1. Fitting a sinusoidal curve to the KAPTURE data.
2. Phase shifting the FGC spot position in steps of one turn and calculating for each step the correlation between the spot size and the sinusoidal curve for the corresponding turns.
3. Determination of the maximum value of this correlation, the corresponding phase shift value is used for the calibration.
4. Averaging over 20 consecutive triggers gives the average phase shift being included into the data analysis as additional delay time with the corresponding error given by the standard deviation.

Finally, this leads to a fine calibration with the uncertainty of 2 turns which is also illustrated in Fig. 6.4. There, the synchrotron oscillation due to the RF phase step is plotted that is recorded with the FGC as well as the KAPTURE system sampling the signal from an APD.

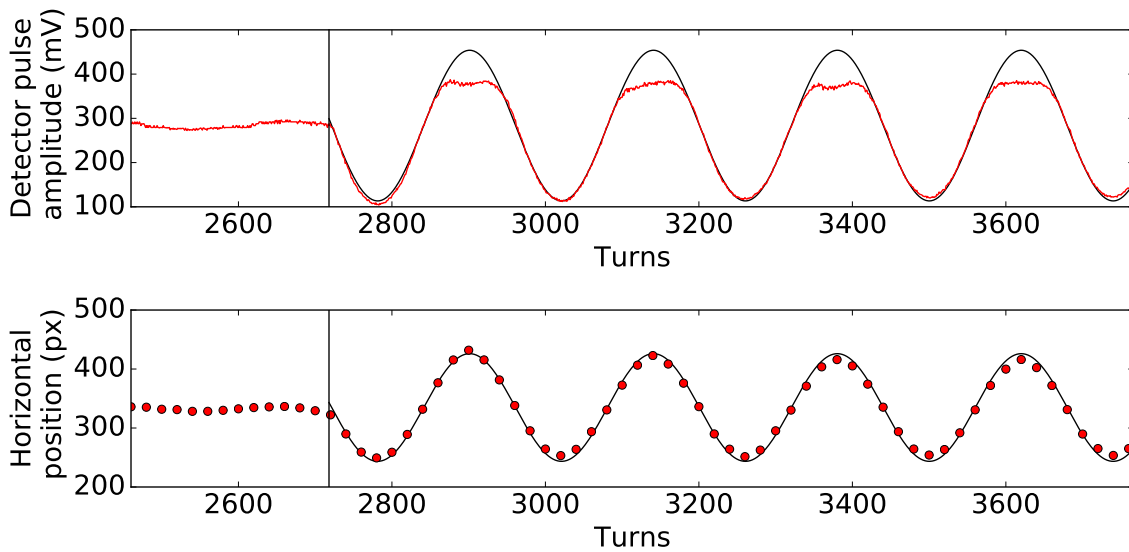


Figure 6.4.: Intensity of the incoherent synchrotron radiation recorded with KAPTURE and an APD (top panel) and the corresponding horizontal bunch position recorded with the FGC. The vertical black line depicts the RF phase step occurring 1 ms (≈ 2720 turns) after the physics trigger. The frequency and the phase of the black sinusoidal curve are determined by a fit to the KAPTURE data. The FGC time axis is calibrated with respect to this curve.

7. Modeling the short-bunch mode accelerator optics

To study the beam dynamics, a proper simulation model of the accelerator is required. Within the scope of this thesis, the Accelerator Toolbox for MATLAB has been used. In this chapter, the simulation model is introduced and the method to determine the quadrupole strengths is discussed. Afterwards, two aspects of the tracking studies are presented: studies of the transverse beam profile and the damping of the horizontal bunch size. Finally, the simulation model is benchmarked against measurements of the equilibrium horizontal bunch size.

7.1. The AT model

The various beam dynamics effects in an accelerator can be studied using a dedicated simulation software. For these studies, many different programs are available. In the scope of this thesis, the Accelerator Toolbox for MATLAB (AT) was chosen [87]. It has the advantage of being integrated into the MATLAB Middle Layer [88], which is also operational at KARA [89]. This integration simplifies the combination of measurements and simulations. In addition, AT recently underwent a major upgrade [26].

The core of these simulations is the machine model. In such a model, each relevant hardware component of the accelerator has its equivalent that is characterised by some geometrical (e.g. length) and beam dynamics parameters (e.g. quadrupole strength). The lattice model used here is based on the previous works of Marit Klein [90] and Max Streichert [91]. It takes into account the measured tilts of the quadrupole and sextupole magnets as well as the multipole components and fringe fields for the dipole magnets. One important task for the simulation is the determination of the magnet strengths. While in a real accelerator, the magnetic strengths are controlled by setting an electric current through the coils via the power supplies, the simulation program directly uses the magnetic strengths. As a direct conversion from the current through the coils to the magnet strength is usually not possible, the magnet strengths have to be determined numerically. For the quadrupole strengths, this can be achieved using LOCO.

7.2. LOCO fits

Linear Optics for Closed Orbits (LOCO) is a software code that – amongst others – allows the determination of the quadrupole strengths by fitting them to measurement data of the horizontal dispersion D_x and the orbit response matrix (ORM) [92].

The horizontal dispersion is determined by measurements of the horizontal shift of the orbit when the RF frequency is varied. For highly relativistic electrons, a change Δf_{RF} of the RF frequency leads to an orbit shift Δx that is proportional to the dispersion D and the momentum compaction factor α_c (see Sec. 2.4). Thus, the dispersion D_x can be determined by [93, Eq. (83)]

$$D_x(s) = -\alpha_c \Delta x(s) \frac{f_{\text{RF}}}{\Delta f_{\text{RF}}}. \quad (7.1)$$

To determine the ORM, the response of the individual beam position monitors (BPMs) to changes of the corrector magnets are measured. Such an ORM contains information on the machine optics in a highly entangled form, from which the beta function β_x can be determined [94]. For the short-bunch mode operation with a low momentum compaction factor α_c , the measurements of the dispersion as well as the ORM are very delicate, especially if a sufficiently high resolution is intended. For such a machine optics, the magnitude of the dispersion is increased locally (see Fig. 3.3). Thus, already a small deviation of the RF frequency leads to a relatively large orbit drift and – in the worst case – to a loss of the electron beam.

The experimental studies discussed in Chapter 8 were conducted for several accelerator optics, which are characterised by different values of the momentum compaction factor α_c . For these optics, LOCO fits are performed to determine the quadrupole strengths. With these quadrupole strengths, it is possible to determine the optics functions and thus the equilibrium bunch size at the imaging source point of the visible light diagnostics (VLD) port. Therefore, the dipole magnets are split into a sequence of short dipole magnets using the *atdivelem* function of AT.

The results of these studies are summarized in Table 7.1. $\alpha_{c,\text{sim}}$ depicts the momentum compaction factor calculated from the simulation model according to Eq. (2.22).

The results of the LOCO fits show that the dispersion at the VLD port is nearly constant for the different optics. For the machine optics A, the resulting dispersion and beta function are plotted in Fig. 7.1.

For the equilibrium state, the horizontal bunch size σ_x can be calculated from the simulation results by

$$\sigma_x = \sqrt{(D \cdot \sigma_\delta)^2 + \beta_x \cdot \epsilon_x}. \quad (7.2)$$

The two summands below the square have a similar magnitude for the optics considered here. Thus, the calculation of the horizontal bunch size is sensitive to large systematic

Table 7.1.: Equilibrium bunch parameters at the VLD imaging source point for different accelerator optics determined from the AT model of KARA using LOCO.

Optics	$\alpha_{c,sim}$	β_x (m)	D (m)	ϵ_x (nm rad)	$\sigma_{x,0}$ (mm)	$\sigma_{t,0}$ (ps)
A	$8.6 \cdot 10^{-4}$	0.76	0.29	79.3	0.28	4.44
B	$5.6 \cdot 10^{-4}$	0.84	0.28	78.5	0.29	3.60
C	$4.4 \cdot 10^{-4}$	0.80	0.29	78.8	0.29	3.23
D	$2.8 \cdot 10^{-4}$	0.74	0.28	78.8	0.27	2.69
E	$2.5 \cdot 10^{-4}$	1.05	0.29	81.76	0.32	2.38

errors [95]. For the case here, the relative error on β_x , D and ϵ_x is estimated to be 5 %. This leads to the error band shown in Fig. 7.2, where the horizontal bunch size is plotted for the optics shown in Fig. 7.1.

It can be seen that the bunch changes its size along one turn and also inside of the dipole magnets.

7.3. Tracking studies

Beyond the determination of the machine optics, the model can be used for tracking studies. Tracking means, that a set of particles – which are individually described by a set of 6D phase space vectors \vec{T} – is sent through the lattice model for a certain number of turns. This allows e.g. to study the shape of the beam at different positions along the trajectory. While for the LOCO fits only the quadrupole magnets were taken into account, these studies also require proper settings of the sextupole magnets. This can be achieved using the *atmatch* function of AT [96]. It fits the sextupole strengths of the lattice model to measured values of the chromaticities. The chromaticities itself can be determined from measurements of the horizontal and vertical betatron tune shift for momentum changes. As for the dispersion, these momentum changes are achieved by changing the RF frequency.

The *classical* approach for tracking is to model the lattice as a sequence of n 6x6 matrices where each matrix represents one element in the accelerator. To track one particle through this lattice for one turn, its 6D phase space vector \vec{T} is multiplied with this matrix sequence:

$$\vec{T}_n = M_1 \cdot M_2 \cdot \dots \cdot M_{n-1} \cdot M_n \cdot \vec{T}_{n-1}. \quad (7.3)$$

Especially for a large number of particles and a *long* lattice (the model used here consists of 424 elements), such computations are very time-consuming. To speed this

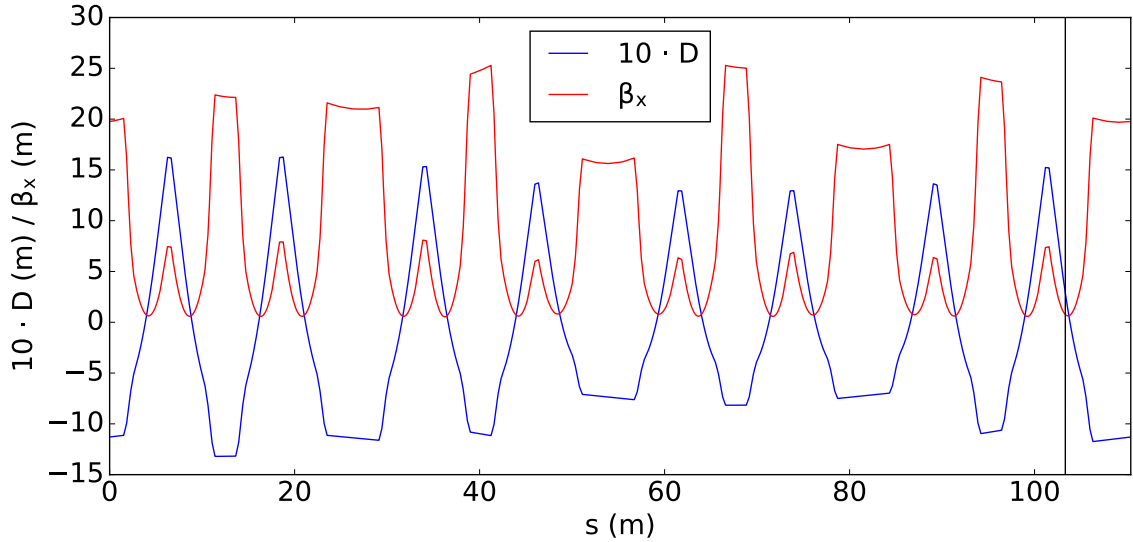


Figure 7.1.: Machine optics (Optics A, see Table 7.1) for KARA determined using LOCO fits. The vertical black line depicts the position of the VLD port. To enhance the visibility, the dispersion is scaled by a factor of 10 to achieve a similar magnitude as for the horizontal beta function β_x .

up, an additional abstraction can be applied using the *atfastring* function [26]. It combines all linear elements (dipole and quadrupole magnets) in one element and all non-linear elements (e.g. sextupole magnets) in another element. Together with the four RF cavities, such an abstracted lattice has only 6 components. To take the quantum excitation due to the emission of synchrotron radiation into account, an additional quantum diffusion element $M_{\text{Quant. diff.}}$ is added [97]

$$\vec{T}_n = M_{\text{Linear}} \cdot M_{\text{Non-linear}} \cdot M_{\text{RF 1}} \cdot \dots \cdot M_{\text{RF 4}} \cdot M_{\text{Quant. diff.}} \cdot \vec{T}_{n-1}. \quad (7.4)$$

This method speeds up tracking a lot, but has the drawback that the particle distribution can only be investigated at the entrance point of the lattice. Thus, this entrance point has to be chosen in a way that it is as close as possible before the observation point. The missing section between the entrance and the observation point is then handled by a linear transfer represented by an additional transport matrix M . Combined with the various functions of AT, such an accelerator model allows to investigate some beam dynamics related effects.

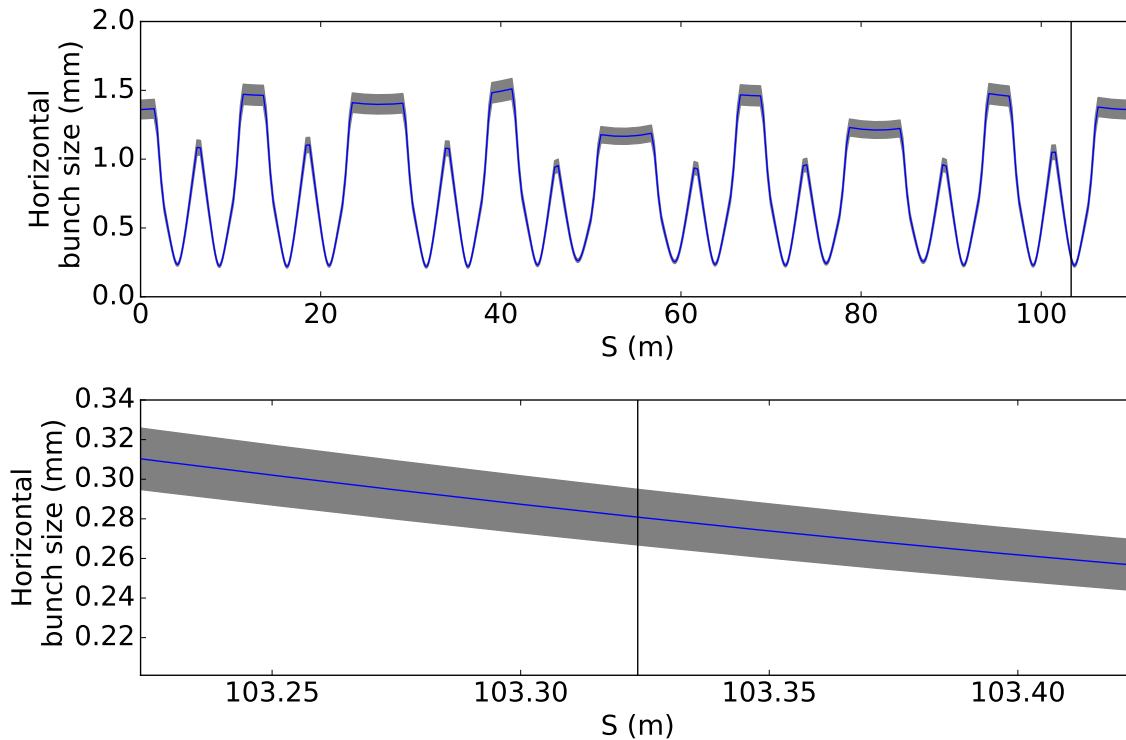


Figure 7.2.: Horizontal bunch size (Optics A, see Table 7.1) for KARA determined using LOCO fits, the vertical black line indicates the position of the VLD port. The error band is calculated assuming a 5% error on the optics functions and the emittance. The bottom panel shows a zoom around the imaging source point of the VLD port.

7.3.1. Imaging the transverse bunch profile

To monitor the transverse bunch profile at a certain position along the ring, two approaches can be used: For the **multi-particle** approach, a bunch of particles is tracked through the lattice for a sufficient number of turns to reach an equilibrium state between radiation damping and quantum excitation. Then, the horizontal and vertical positions of the particles can be mapped when the bunch passes the monitor. For a sufficient resolution, a large number of particles ($> 10^6$) is required. This leads to very long computational times due to the tracking of the transient process. A more memory-efficient way is the **single-particle** approach. Here, a single particle is tracked for a very large number of turns and for each turn, its transverse position is mapped. After a sufficient number of turns, this particle has sampled the whole phase space and thus the histogramming of the positions allows the imaging of the transverse bunch profile. This approach is valid as long as there is no interaction between the particles.

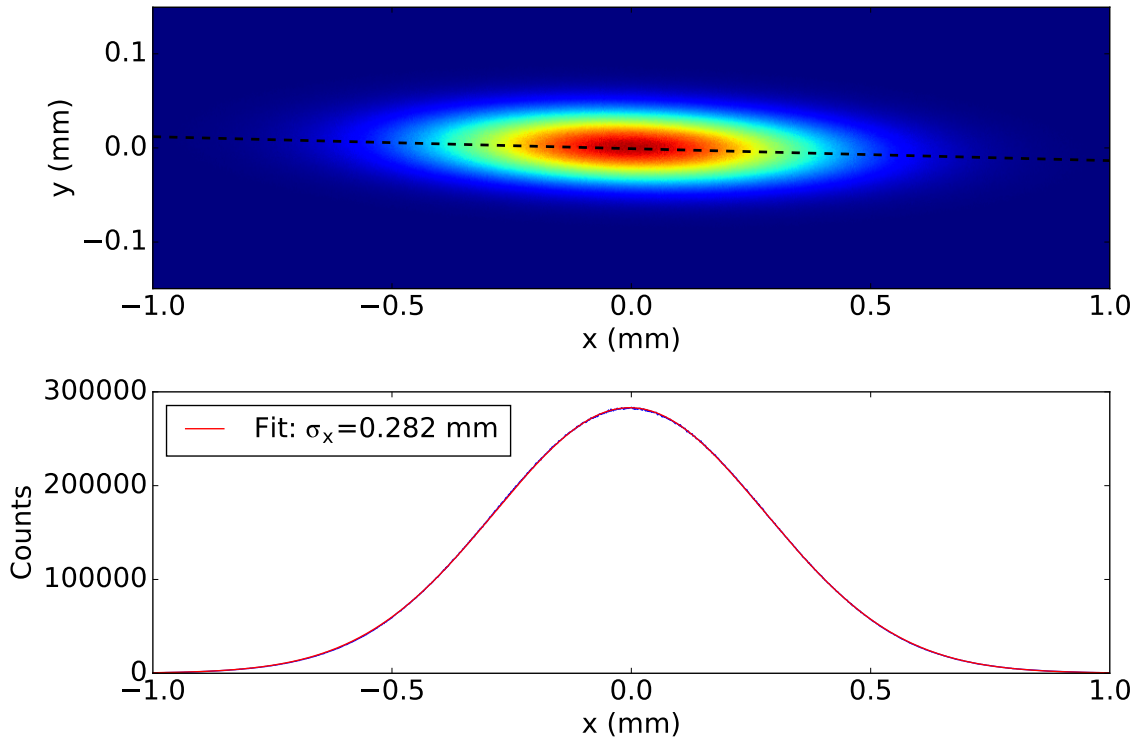


Figure 7.3.: Simulated electron beam at the VLD port source point. For the simulation, a single particle was tracked for $2 \cdot 10^8$ consecutive turns and for each turn the horizontal and vertical positions are histogrammed. The dashed line illustrates the slight tilt of the ellipse (tilt angle: 0.7°). The bottom panel shows the projection onto the x-axis with a Gaussian fit applied to it.

In Fig. 7.3, such a single particle image is illustrated. It shows a simulated bunch profile at the VLD imaging source point and is acquired by mapping $2 \cdot 10^8$ turns using machine optics A (see Table 7.1).

The resulting image can be seen as an equivalent for the image of a bunch consisting of $2 \cdot 10^8$ particles, in case of KARA this corresponds to a bunch current of 0.09 mA. The tilts of the magnets induce an additional coupling between the horizontal and vertical direction and lead to a tilt of the beam ellipse as it is illustrated by the dashed line. As this angle is relatively small (0.7°), the deviation of the size of the horizontal projection and the size of the ellipse are below the measurement uncertainties. Thus, this tilt is neglected and the horizontal bunch size is determined from the horizontal projection.

Fitting a Gaussian to the horizontal projection gives an equilibrium bunch size of 0.282 mm which agrees well with the value calculated from the optics functions and the equilibrium emittance (0.281 mm).

7.3.2. Diffusion blow-up

The energy loss of the particles due to the emission of synchrotron radiation leads to damping effects. This damping reduces the amplitude of the synchrotron oscillation, but also leads to a shrinking of the bunch size. As the emission of the radiation also leads to a quantum excitation that counteracts the damping, an equilibrium state is reached after a certain amount of time (Sec. 2.5).

For the understanding and investigation of the micro-bunching instability – which is coupled to a variation of the energy spread – the determination of the damping times is crucial. One possibility to measure the longitudinal damping time is the damping of the coherent motion of the bunch, e.g. a strong synchrotron oscillation triggered by a sudden step in the RF phase. This approach has the drawback, that it is sensitive to decoherence effects and Landau-Damping due to the chromaticity [98]. Alternatively, the damping times can be accessed by investigations of the bunch size as well.

While a proper simulation of collective effects using tracking programs usually requires a large number of particles ($\sim 1 \cdot 10^9$) and thus a high computational power, the damping of the bunch that follows a coherent synchrotron radiation (CSR) burst can be studied also with a lower number of particles. The micro-bunching instability leads to a blow-up of the longitudinal phase space. In the simulation, this can be approximated by manipulating the quantum diffusion element. This element is described by a 6x6 matrix L^T and affects the bunch as [97, Eq. (12)]

$$\vec{T}_1 = \vec{T}_0 + L^T \cdot \vec{r}. \quad (7.5)$$

\vec{r} is as a set of random numbers with $\sigma = 1$ and $\mu = 1$. For the blow-up of the longitudinal phase space, this matrix is multiplied by a blow-up matrix B :

$$\tilde{L}^T = L^T \cdot B = L^T \cdot \begin{pmatrix} 1 & 0 & 0 & 0 & 0 & 0 \\ 0 & 1 & 0 & 0 & 0 & 0 \\ 0 & 0 & 1 & 0 & 0 & 0 \\ 0 & 0 & 0 & 1 & 0 & 0 \\ 0 & 0 & 0 & 0 & b & 0 \\ 0 & 0 & 0 & 0 & 0 & b \end{pmatrix} \quad (7.6)$$

that is characterised by a scaling parameter b ($b > 1$). This blow-up holds on for a certain number of turns (here: 2000) before b is set to 1 and the damping start to dominate. For the analysis, the horizontal bunch size σ_x is calculated by the standard deviation of the horizontal particle position for each simulation step.

According to Eq. (2.38), the emission of synchrotron radiation leads to different damping times in the horizontal and longitudinal plane. Therefore, the longitudinal component (the energy spread σ_δ) and the horizontal component (emittance ϵ_x) of the horizontal bunch size are damped with different damping times.

After an excitation, which increases the energy spread by the amount A and that stops at $t = 0$, the energy spread is damped with the longitudinal damping time τ_z towards the natural energy spread δ_0 . This can be written as [31, solving Eq. (116)]:

$$\sigma_\delta(t) = \sqrt{A \cdot e^{-2t/\tau_z} + \delta_0^2}. \quad (7.7)$$

The horizontal emittance is damped with the horizontal damping time τ_x towards its equilibrium value $\epsilon_{x,0}$ [31, Eq. (120)]:

$$\begin{aligned} \epsilon_x(t) &= \epsilon_x(t=0) \cdot e^{-2t/\tau_x} + \epsilon_{x,0} \cdot [1 - e^{-2t/\tau_x}] \\ &= B \cdot e^{-2t/\tau_x} + \epsilon_{x,0}. \end{aligned} \quad (7.8)$$

Combining equations (7.7) and (7.8) leads to

$$\begin{aligned} \sigma_x(t) &= \sqrt{D^2 \cdot \sigma_\delta(t)^2 + \beta_x \cdot \epsilon_x(t)} \\ &= \sqrt{D^2 \cdot [A \cdot e^{-2t/\tau_z} + \delta_0^2] + \beta_x \cdot [B \cdot e^{-2t/\tau_x} + \epsilon_{x,0}]} \end{aligned} \quad (7.9)$$

$$\approx \sqrt{C \cdot e^{-2t/\tau_{x,eff}} + \sigma_{x,0}^2}. \quad (7.10)$$

Thus, the horizontal bunch size is damped with an *effective* horizontal damping time $\tau_{x,eff}$ towards its equilibrium value $\sigma_{x,0}$. The effective damping time $\tau_{x,eff}$ is a function of two amplitudes A and B and the damping times:

$$\tau_{x,eff} = \tau_{x,eff}(A, B, \tau_x, \tau_z) \text{ with } \tau_z \leq \tau_{x,eff} \leq \tau_x.$$

Figure 7.4 shows the damping of the various bunch parameters for a simulated diffusion blow-up of the longitudinal phase space. Here, the bunch was blown up longitudinally for a certain time period which is marked as grey bar followed by a decay due to radiation damping.

Even if only the longitudinal phase space has been blown-up here, the horizontal emittance increases as well. Fitting Eq. (7.7) to the energy spread (top panel) leads to $\tau_z = 10.3$ ms, while the fit according to Eq. (7.8) to the horizontal emittance (center panel) gives $\tau_x = 18.4$ ms. Both values are in reasonably good agreement with the values determined from the synchrotron radiation integrals (see Eq. (2.38)), which are 10.4 ms and 20.4 ms, respectively. The horizontal emittance was calculated using [24, Eq. (8.39)]. The effective horizontal damping time $\tau_{x,eff}$ is determined by fitting Eq. (7.10) to the horizontal root mean square (RMS) bunch size which gives a value of $\tau_{x,eff} = 14.0$ ms.

As the horizontal emittance cannot be determined experimentally at KARA yet (at least not time-resolved), a quantitative measurement of the energy spread is not possible. Therefore, only the horizontal bunch size is used in the following as a qualitative measure for the energy spread during the micro-bunching instability. To overcome this limitation, a second time-resolved measurement of the horizontal bunch size would be required at a position with a different horizontal beta function β_x .

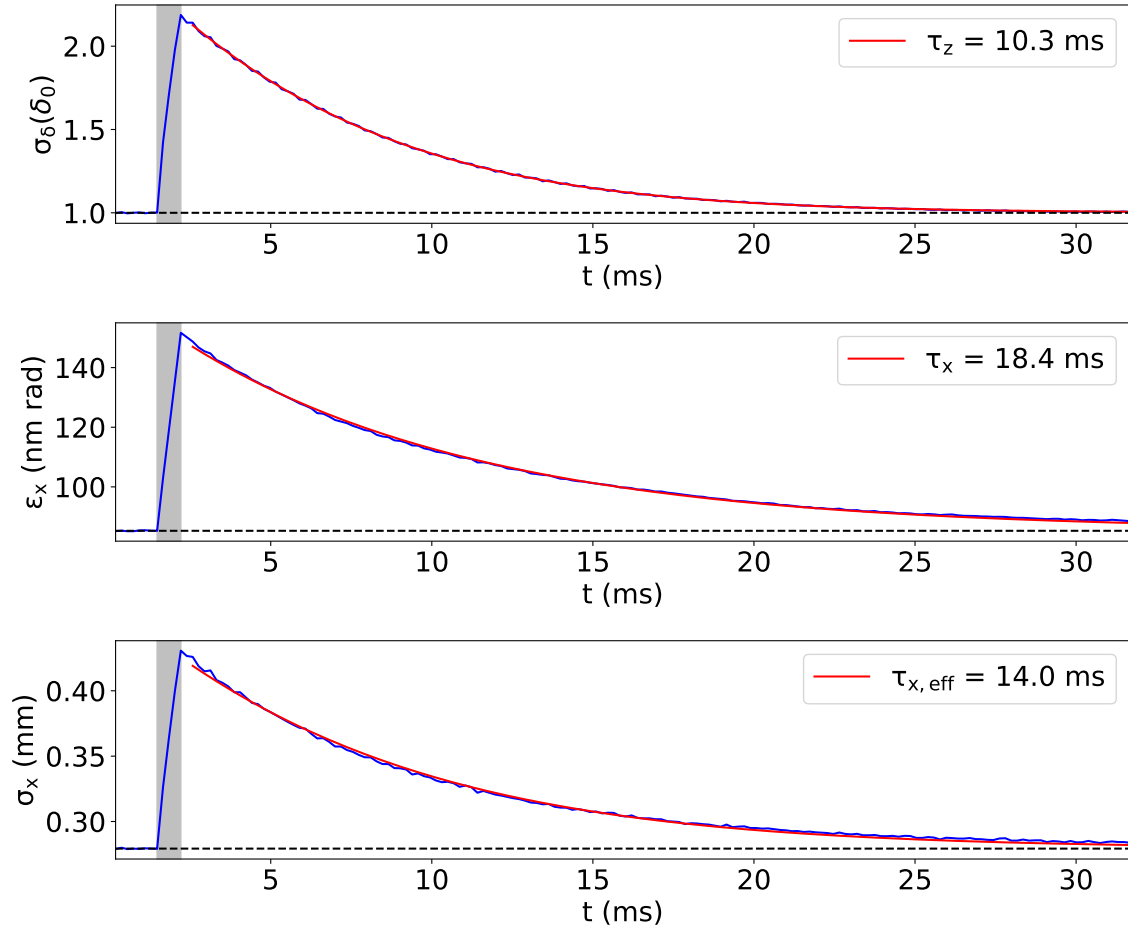


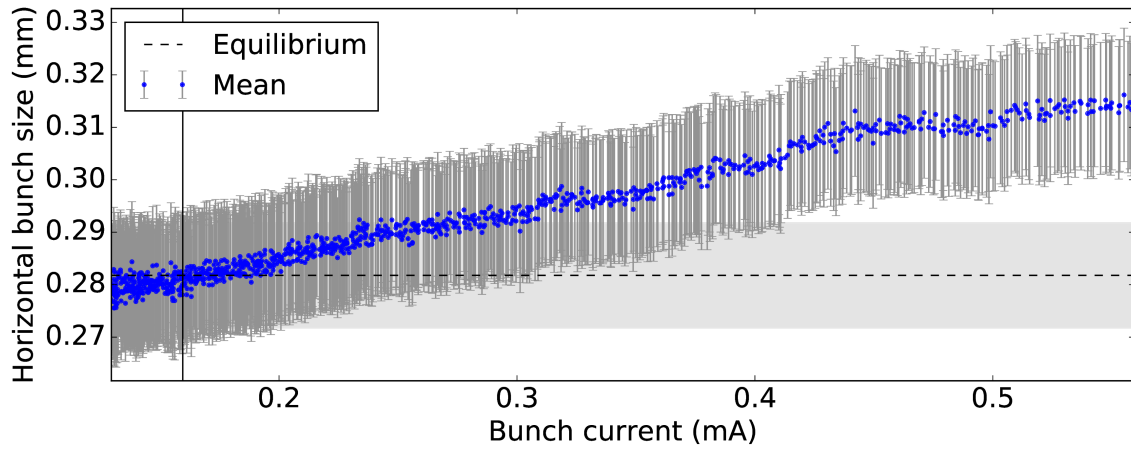
Figure 7.4.: Damping of various parameters followed by blow-up of the longitudinal phase space. The top panel shows the energy spread σ_δ in units of the natural energy spread δ_0 , the center panel the horizontal emittance ϵ_x and the bottom panel the horizontal bunch size σ_x . The grey bar indicates the time range of this blow-up (see also Sec. 7.3.2).

Simulation parameters: Machine optics A (see Table 7.1), 100.000 particles

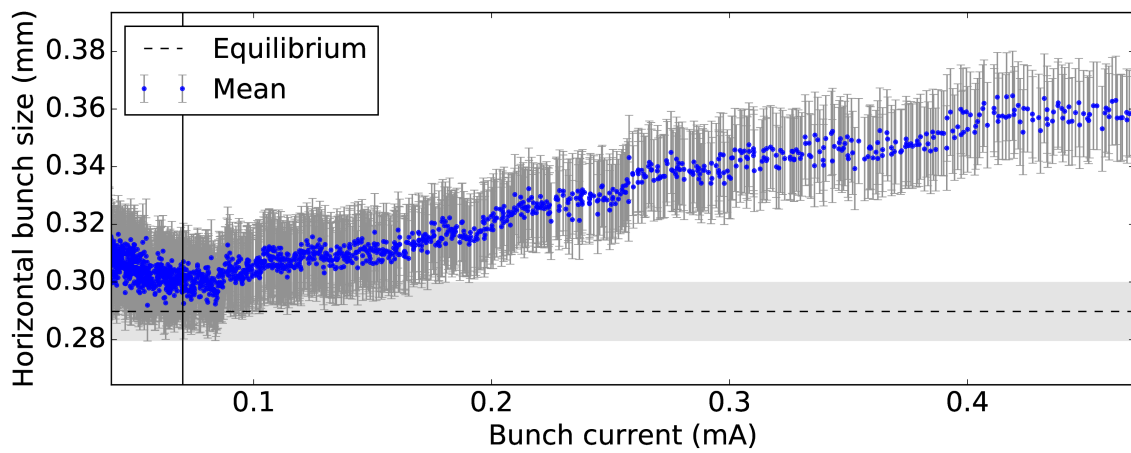
7.4. Benchmarking the AT model

When the bunch current exceeds the bursting threshold, the micro-bunching instability leads to an increase of the energy spread [13], which can be detected as an increase of the horizontal bunch size. Below the bursting threshold, the horizontal bunch size is constant due to the equilibrium between quantum excitation and radiation damping. This allows a benchmarking of the simulation model and the underlying LOCO fits against fast-gated intensified camera (FGC) measurements. Therefore, the average horizontal bunch size from FGC images is compared to the calculated values from the simulation model. For three optics from Table 7.1, this is illustrated in Fig. 7.5, where the measured horizontal bunch size is plotted above and below the bursting threshold. In addition to the errors on the horizontal bunch size from the optics functions, another contribution is taken into account as well. At the VLD port, not only one point but a certain part of the beam trajectory is imaged. Along this part of the trajectory, the horizontal bunch size is expected to change as well (see Fig. 7.2) As the exact part of the trajectory is not known, this induces an additional error on the equilibrium horizontal bunch size. Therefore, the total error on the equilibrium horizontal bunch size is – based on a Monte-Carlo error propagation – estimated to be $\pm 10 \mu\text{m}$, which is plotted as an error band.

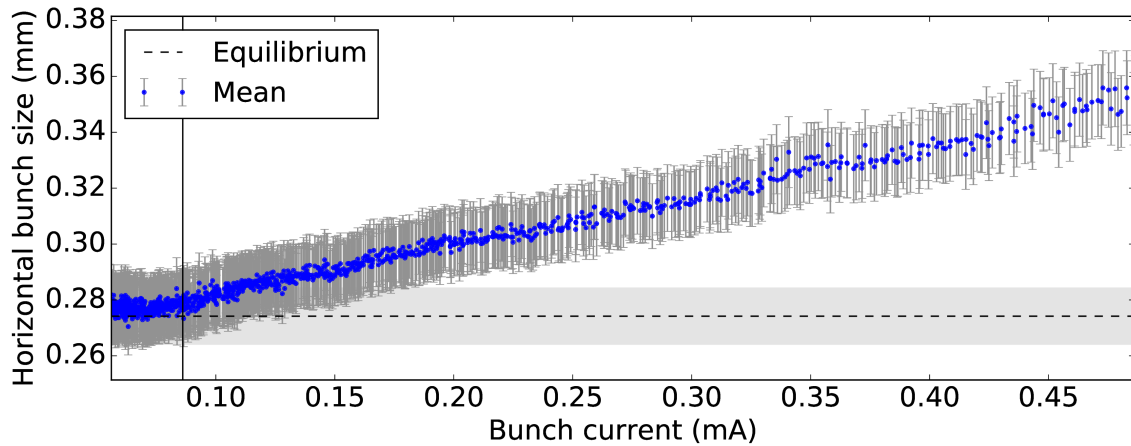
While the horizontal bunch size is roughly constant below the bursting threshold, it starts to increase when the bunch current exceeds this threshold. In general, the plots show a good agreement between the measured bunch size and the calculated value for the equilibrium case below the bursting threshold. This means that the parametrisation of the filament beam spread function (FBSF) with only one parameter (angular deviation β between electron orbit and optical axis) is reasonable. For the case shown in Figure 7.5a, the measured values are slightly below the theoretical ones. This mismatch can be due to the relatively large systematic errors that can occur at these studies [95]. Nevertheless, these results show that the the data analysis scheme for the FGC with its handling of the FBSF on one hand and the machine model based on LOCO fits on the other hand agree quite well.



(a) Optics A:



(b) Optics C



(c) Optics D

Figure 7.5.: Mean horizontal bunch size over four different bunch current decays using different machine optics. The dashed line and its grey error bar depict the equilibrium bunch size range at the VLD source point, while the vertical black line illustrates the bursting threshold. The vertical axes are zero-suppressed.

8. Potential for studies of horizontal bunch size and arrival time

The micro-bunching instability leads to a modulation of the longitudinal phase space. For a certain bunch current range, this instability is coupled to a bursting behaviour of the bunch and a sawtooth-like modulation of the energy spread. To study this instability in more detail with the long-term perspective to control this instability, the measurement systems described in the previous chapter have been used: the FGC and KALYPSO for time-resolved horizontal bunch size measurements and the TCSPC system for bunch arrival time studies. In the first part, the synchronous studies of energy spread and CSR intensity are presented, while in the second part, studies of the damping time and the bursting frequency are discussed. The third part covers the impedance measurements, before the first experimental observation of the short bunch-length bursting on the energy spread is presented at the end.

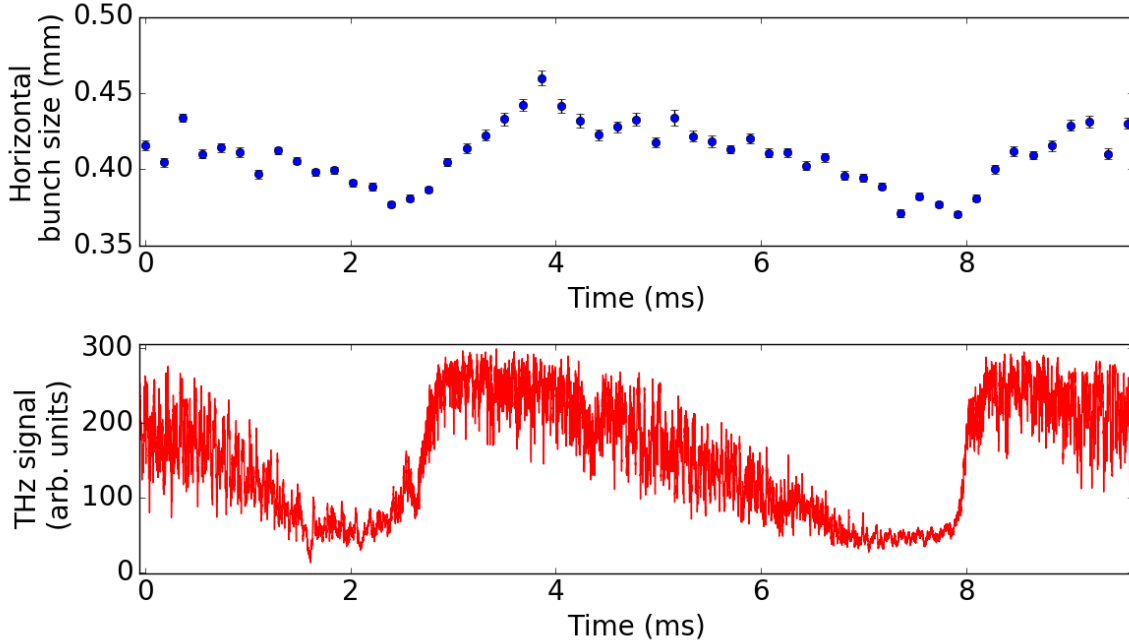
8.1. Synchronous studies of energy spread and CSR

As discussed in Chapter 4, the micro-bunching instability is coupled to the emission of coherent synchrotron radiation (CSR). Previous studies showed a sawtooth-like modulation of the bunch size (bunch length and energy spread) with the same modulation period length as the CSR [5, 15, 18]. It is noteworthy that the measurements discussed there did not have a single-turn resolution as it became possible at KARA with the fast-gated intensified camera (FGC) setup. In addition, the FGC setup is synchronised to other detector systems, especially to those for the CSR detection.

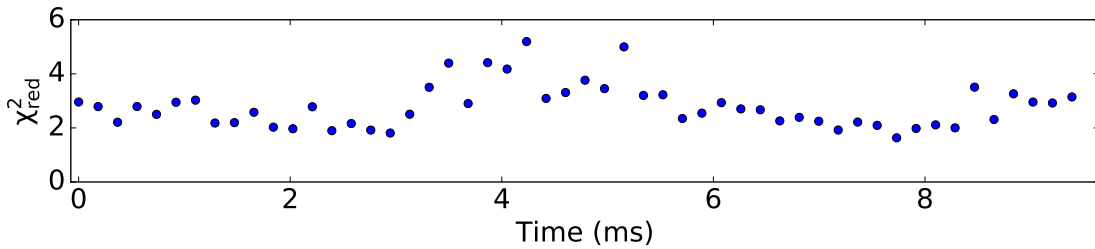
The measurements discussed in this section show time-resolved studies using the FGC (see Sec. 5.2) and the KAPTURE system. After applying the data analysis to the individual FGC images, the resulting horizontal bunch size as measure for the energy spread are set into context with the CSR intensity taken simultaneously.

8.1.1. Bursting behaviour of energy spread and CSR

The first example for such a synchronised measurement is illustrated in Fig. 8.1a. The top panel shows the horizontal bunch size (and thus the energy spread), while the bottom panel shows the CSR intensity measured using a broadband Schottky diode read out by the KAPTURE system [52, 53]. The used diode has a sensitivity range from 50 GHz up to 1 THz [99].



(a)



(b)

Figure 8.1.: (a) Horizontal bunch size as measure for the energy spread recorded with a gate separation of 500 turns (top) and the synchronously measured CSR signal sampled using a Schottky diode (bottom). The energy spread shows the same modulation pattern as the CSR (data published in [100, Fig. 7], CSR data: courtesy Miriam Brosi).

(b) Reduced chi-squared for the fits to determine the horizontal bunch size.

Beam parameters: $f_s = 8.1$ kHz, $V_{\text{RF}} = 1500$ kV, $I_{\text{bunch}} = 0.88$ mA

One can see that the energy spread shows the same modulation period length as the CSR. At the onset of the burst, the bunch is blown up until it reaches a certain upper limit where damping effects start to become dominant and the size as well as the CSR intensity start to decrease. This shrinking holds on until a certain lower limit is reached being coupled to the onset of the next burst. This behaviour was already experimentally observed at SURF III in 2001 [5]. The occurrence of the micro-bunching instability is due to a deformation of the longitudinal phase space. Besides the periodic occurrence of sub-structures on the bunch profile, there is also global distortion of the charge distribution which has also been observed experimentally on the longitudinal bunch profile at KARA [39]. Due to its ability to resolve single turns, the FGC can be used to study the deformation of the energy profile during the bursting behaviour. To quantify the deformation of the horizontal bunch profile, the reduced chi-squared χ_{red} for the fits to determine the horizontal bunch size (see Sec. 5.2.3) is investigated. For the case plotted in Fig. 8.1a, this is shown in Fig. 8.1b.

There, the data show the same periodic behaviour as the horizontal bunch size and the CSR intensity. As closer the value of χ_{red}^2 is to 1, the more Gaussian the bunch shape is. This shows, that during the damping-induced shrinking, the bunch becomes more and more Gaussian before it is distorted again when the instability triggers the onset of the next burst. This distortion can either be due to a global deformation e.g. the bunch is leaning sideways or due to sub-structures on the profile itself.

The second example discussed here is taken for a lower value of α_c and also at a lower bunch current. The horizontal bunch size and the corresponding CSR signal are shown in Fig. 8.2.

Again, the energy spread as well as the CSR intensity have the same modulation period length. Compared to Fig. 8.1a, the CSR intensity is no longer constant between two bursts, but shows an increase while the energy spread is still decreasing. This can be explained by the fact, that the bunch becomes shorter and this shortening leads to the emission of CSR for higher frequencies. The broadband Schottky diode used here is sensitive to these bunch length fluctuations and thus this decrease of the bunch length leads to higher intensities in the frequency band of the diode. This shrinking holds on until a certain lower limit is reached. At this point, the charge density inside the bunch is high enough to trigger a new burst. Numerical simulations using the Vlasov-Fokker-Planck solver Inovesa [49] showed, that at this point the amplitude of the sub-structures starts to grow rapidly as well [101].

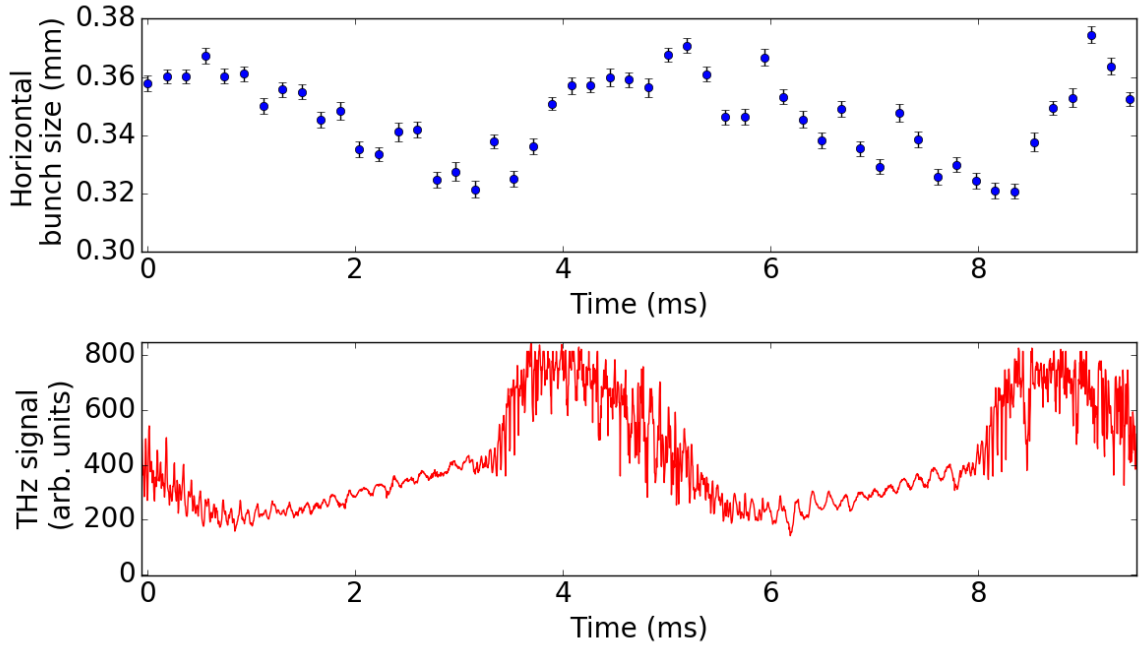


Figure 8.2.: Horizontal bunch size as measure for the energy spread recorded with a gate separation of 504 turns (top) and the synchronously measured CSR signal recorded using a Schottky diode (bottom). The two curves have the same modulation period length, but here the CSR intensity starts to increase again while the bunch is still shrinking (data published in [100, Fig. 8], CSR data: courtesy Miriam Brosi).

Beam parameters: $f_s = 6.7$ kHz, $V_{\text{RF}} = 1500$ kV, $I_{\text{bunch}} = 0.25$ mA.

8.1.2. Onset of a CSR burst

To study the onset of a CSR burst in more detail, the FGC is configured to record shorter time scales.

For the example discussed here, the gate separation was set to 24 turns and a time range of 500 μs was used. In this case also a second – narrow-band – Schottky diode was used (sensitivity range: 220-330 GHz [102]). The result is illustrated in Fig. 8.3.

At the beginning, the horizontal bunch size and thus the energy spread is slightly decreasing due to damping effects. At the same time, the CSR intensity on both Schottky diodes is constant. Around $t=0.1$ ms, the first changes can be seen when the CSR intensity on the broadband Schottky diode starts to increase, while for the narrow-band this increase starts approximately 0.1 ms later. This earlier increase on the broadband Schottky diode is due to their lower frequency limit [55]. The increase of the CSR intensity seen by the narrow-band Schottky diode is due to sub-structures occurring on the bunch profile. At this early stage, they are too small to substantially increase the overall bunch size, so it stays roughly constant with some fluctuations.

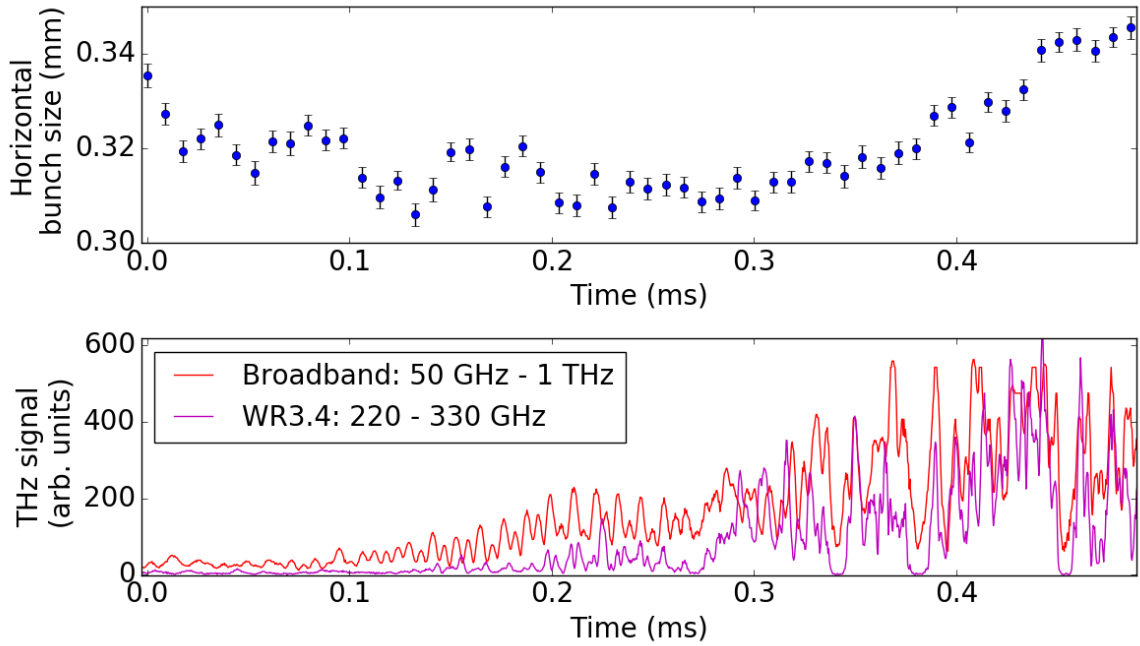


Figure 8.3.: Horizontal bunch size as measure for the energy spread recorded with a gate separation of 24 turns to achieve a good timing resolution (top) and the corresponding CSR intensity (bottom) sampled with two Schottky diodes with different bandwidths (data published in [100, Fig. 9], CSR data: courtesy Miriam Brosi).

Beam parameters: $f_s = 13.35$ kHz, $V_{\text{RF}} = 1500$ kV, $I_{\text{bunch}} = 1.57$ mA

At a certain point the horizontal bunch size as well as the CSR intensity starts to increase rapidly. Invesa simulations showed that this onset is due to rapid changes of the amplitude of the sub-structures on the bunch profile [101].

These single image based examples already clearly demonstrate the ability of the FGC to study the energy spread dynamics during the micro-bunching instability. The synchronous measurement of the CSR intensity shows that the energy spread and the CSR intensity undergo fluctuations with the same period length. Nevertheless, they can show different behaviours between the bursts, depending on the range of the bunch length fluctuations defining the lower frequency limit of the emitted CSR.

8.1.3. Turn-by-turn studies of the bursting behaviour

As previously discussed, the FGC setup has an intrinsic limit as it can only handle a limited number of data points. Thus, a trade-off between a good temporal resolution and a long time range is required beforehand of a measurement. To overcome this limitation, a KALYPSO system is used. In combination with the data analysis discussed in Sec. 5.3, such a system allows a turn-by-turn investigation of the energy spread by recording the horizontal bunch size. This allows to study the onset of a CSR bursts and to investigate the phase offset between the energy spread and the CSR intensity in more detail. KALYPSO is based on the same hardware architecture as the KAPTURE system and thus also overcomes the intrinsic mechanical and electrical delays of the FGC setup. This enables an instantaneous start of the sampling and therefore simplifies the synchronisation with other detector systems, e.g. for CSR measurements. For the measurements discussed in the following, an oscilloscope in the segmented mode is used to sample a Schottky detector for the CSR as well as an avalanche photo diode (APD) for the incoherent synchrotron radiation.

To check if the two detector systems measure synchronously, abrupt onsets of the synchrotron oscillation are used. These onsets can be induced by triggered steps in the RF phase, but they also happen randomly from time to time. The latter case is used here. Fig. 8.4 shows the horizontal bunch position recorded using KALYPSO and the corresponding signal from an APD sensitive in the visible range in the IR1 beam line at KARA.

The abrupt onset of the synchrotron oscillation at 23.2 ms occurs on both curves at the same time. Thus, the two detector systems can be used for synchronous studies. This allows to study the horizontal bunch size and the CSR intensity recorded using a broadband Schottky diode [99]. Such a measurement – covering a time range of 27 ms – is plotted in Fig. 8.5.

It can be seen, that the horizontal bunch size (and thus the energy spread) shows the same modulation pattern as the bursting CSR. The turn-by-turn ability of KALYPSO allows to study this in more detail. To illustrate this, the time range between 13.1 ms and 20.7 ms is investigated in the following, that is also illustrated by the gray area in Fig. 8.5. It is plotted in Fig. 8.6.

There, it can be seen that the minimum horizontal bunch size does not exactly coincide with the onset of the CSR burst in the signal from the Schottky diode, as the latter one starts to increase approximately 0.58 ms earlier. At this early stage of a CSR burst, the amplitudes of the sub-structures on the longitudinal bunch profile are too small to lead to an overall increase of the bunch size as damping effects are still dominant. At a certain point, the instability driven blow-up starts to dominate and the bunch is blown up.

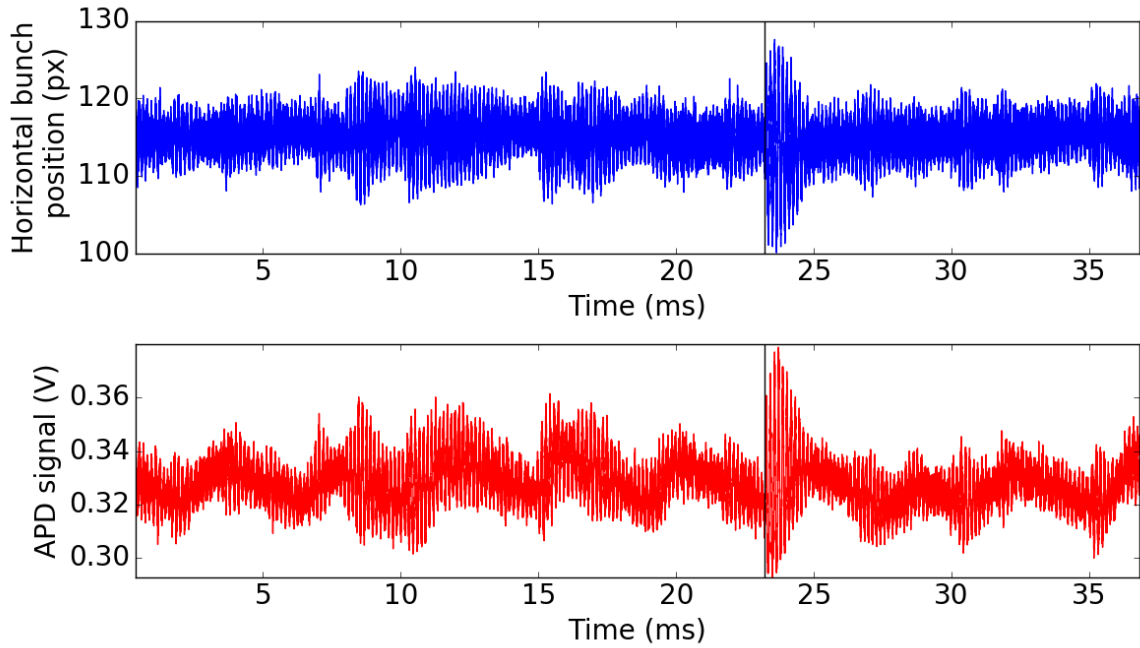


Figure 8.4.: Horizontal bunch position from KALYPSO at the visible light diagnostics (VLD) port (top) and the corresponding signal from an APD sampling the incoherent synchrotron radiation using an oscilloscope in the segmented mode (bottom). The vertical black lines depict the onset of a synchrotron oscillation acting as a timing reference for the synchronisation (APD data: courtesy Johannes L. Steinmann).

Already this one data set shows the potential of KALYPSO for energy spread studies. At the FGC, the observation of the onset of a burst with a good temporal resolution has to be seen as a *lucky punch* as it is required to exactly hit the relevant time range which spans only approximately half a millisecond (see e.g. Fig. 8.3). The main drawback of the current version, that has been tested here, is the limited dynamic range and a quite high noise level. This will be improved by a future version of the system. Thus, KALYPSO will allow time-resolved energy spread studies in unprecedented detail.

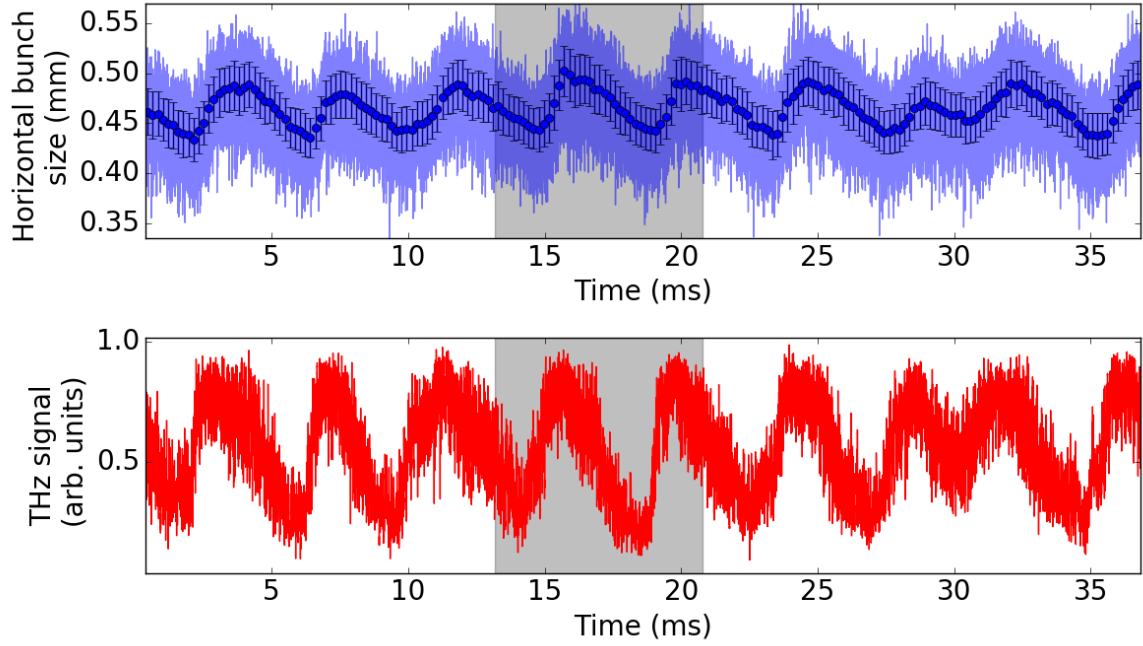


Figure 8.5.: Top: Horizontal bunch size recorded using KALYPSO. To overcome the noisy structure of the bunch size signal, profile histograms have been applied to the data.

Bottom: Corresponding CSR intensity sampled using an oscilloscope in the segmented mode. The data set is the same as in Fig. 8.4 (CSR data: courtesy Johannes L. Steinmann).

Beam parameters: $f_s = 6.8$ kHz, $V_{\text{RF}} = 1500$ kV, $I_{\text{bunch}} = 0.80$ mA.

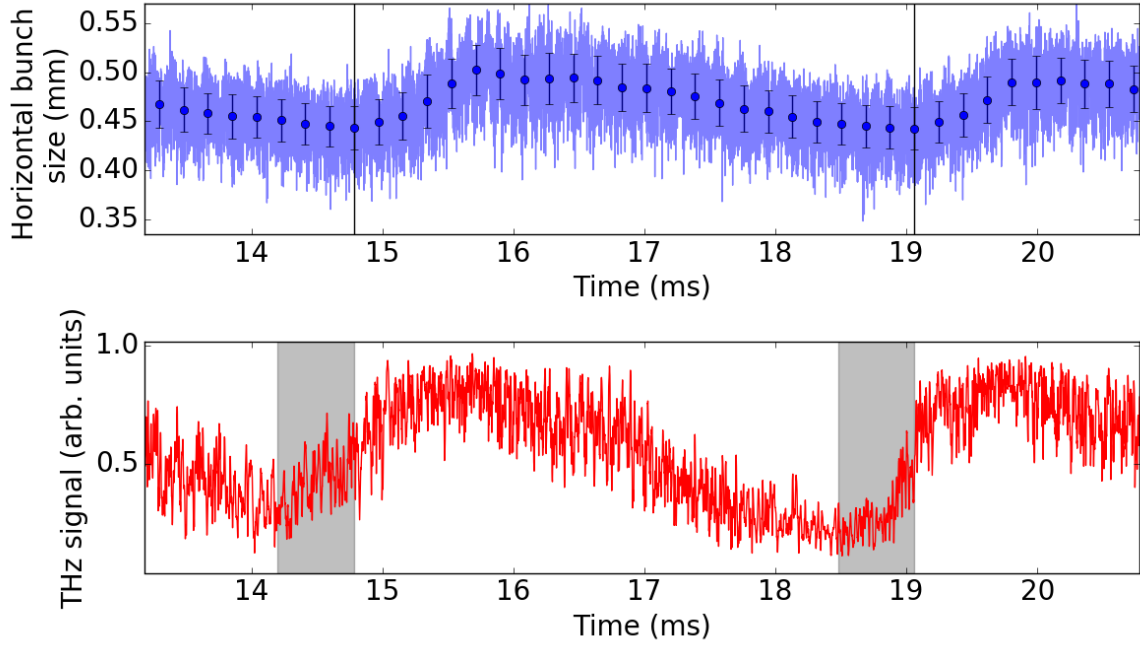


Figure 8.6.: Zoom into the data set shown in Fig. 8.5 with the horizontal bunch size in the top and the CSR intensity in the bottom panel. The vertical black lines depict the times, where the horizontal bunch size is minimum, while the grey bar in the top panel illustrates the time range, where the CSR intensity already starts to increase beforehand of the energy spread increase (CSR data: courtesy Johannes L. Steinmann).

8.2. Radiation damping and bursting frequency

As the bursting behaviour of the bunch due to the micro-bunching instability is an interplay between excitation and radiation damping, studies of the damping behaviour are required to achieve a deeper insight into the physics of these processes. Using the FGC for time-resolved horizontal bunch size measurements allows to study this in more detail.

The damping of the horizontal bunch size depends on the horizontal as well as the longitudinal damping time. As the longitudinal and horizontal contributions can not be distinguished, an *effective* damping time is used as a measure for the horizontal bunch size damping (see Eq. (7.10)). For two FGC images taken at identical machine settings (corresponding to optics A in Table 7.1), measurements of this effective damping time are shown in Fig. 8.7.

There, it can be seen that the horizontal bunch size is undergoing a sawtooth-like modulation due to the micro-bunching instability which is coupled to a bursting behaviour of the bunch. While the bunch currents are approximately the same, the duty cycle and the period length of the sawtooth as well as the effective damping times scatter. While for the case in Fig. 8.7a, the period length is 5.7 ms with effective damping times of 11.2 ms and 9.7 ms, the period length in Fig. 8.7b is 6.4 ms with effective horizontal damping times of 15.6 ms and 15.3 ms, respectively.

In this case, the lower damping – depicted by a larger damping time – leads to an increase of the bursting period. There, it takes more time until the instability threshold is hit again resulting in triggering the onset of the next burst. For the case in Fig. 8.7b, the decay of the bunch size – where the fit is applied to the data – is not as smooth as for the cases shown in Fig. 8.7a. This is a hint that in this case the micro-bunching instability continued to blow-up the bunch even if radiation damping is dominant leading to a shrinking of the bunch size. Already these two examples clearly show the high degree of randomness in the individual bursts.

For the accelerator optics used here, the Accelerator Toolbox for MATLAB (AT) simulations predicted an effective horizontal damping time of 14.0 ms (see Fig. 7.4).

Extending the damping time studies over a certain bunch current range shows, that the determined effective damping times $\tau_{x,\text{eff}}$ scatter around a mean value which is close to the value predicted by AT simulations as it is shown in Fig. 8.8.

This is a first hint, that the bursting frequency is mostly determined by the radiation damping due to the emission of incoherent synchrotron radiation. Therefore, the relation between the horizontal bunch size, its damping and the repetition rate of the CSR bursts can be studied as it will be discussed in the following.

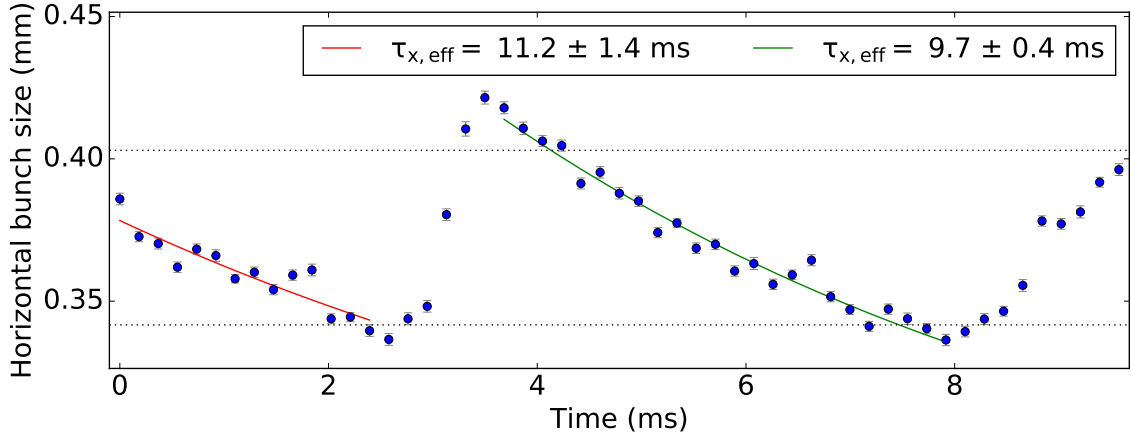
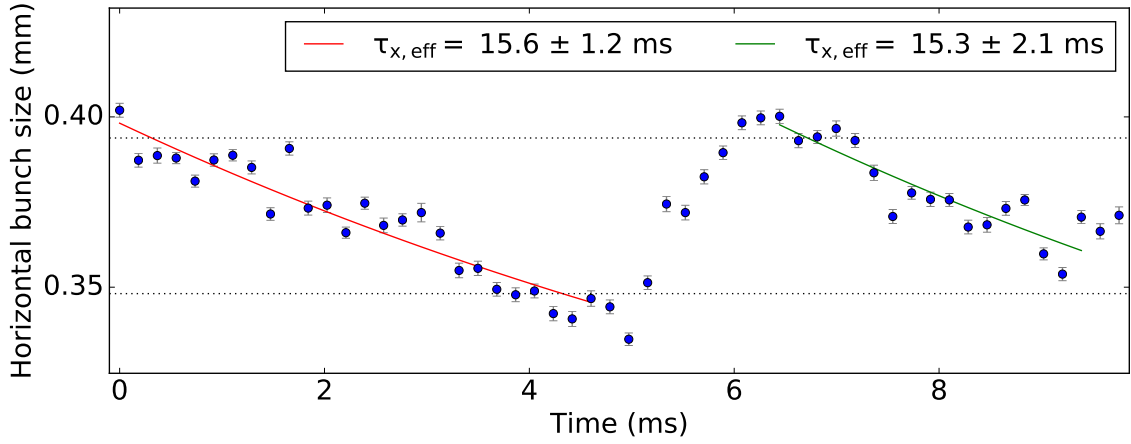

 (a) $I_{\text{bunch}}: 1.29 \text{ mA}$

 (b) $I_{\text{bunch}}: 1.28 \text{ mA}$

Figure 8.7.: Horizontal bunch size measured using the FGC in the short-bunch mode during the bursting behaviour of the bunch. To determine the effective damping time, an exponential fit is applied to the falling edges. The dotted lines depict the 10th and 90th percentile of the horizontal bunch size, respectively.

Beam parameters: $f_s = 11.2 \text{ kHz}$, $V_{\text{RF}} = 1500 \text{ kV}$, $\alpha_c = 4.8 \cdot 10^{-4}$

A simple model to describe the sawtooth behaviour of the horizontal bunch size σ_x is given by Eq. (8.1)

$$\sigma_x(t) = \begin{cases} \sqrt{Ce^{-2t/\tau_{x,\text{eff}}} + \sigma_{x,0}^2}, & \text{for } 0 \leq t \leq t_{\text{decay}} \\ mt + \sigma_{x,\text{min}}, & \text{for } t_{\text{decay}} \leq t \leq 1/f_{\text{burst}} \end{cases} \quad (8.1)$$

which describes the behaviour as a sequence of an exponential decay holding on for a time period t_{decay} followed by a linear rise with the duration $t_{\text{rise}} = 1/f_{\text{burst}} - t_{\text{decay}}$.

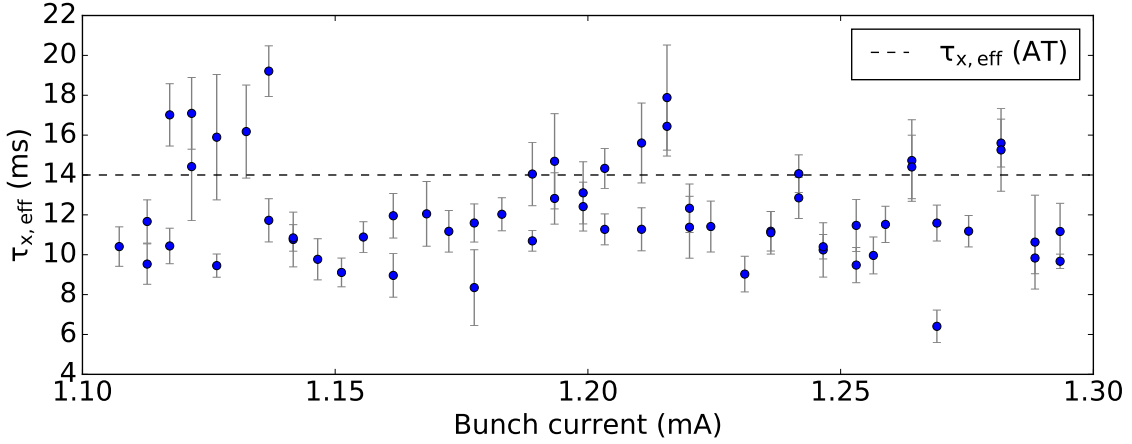


Figure 8.8.: Effective horizontal damping times over bunch current. The dashed line depicts the effective horizontal damping time determined by AT simulations.

As for a sawtooth signal, a *duty cycle* d can be defined as

$$d = t_{\text{rise}} \cdot f_{\text{burst}} = (1/f_{\text{burst}} - t_{\text{decay}}) \cdot f_{\text{burst}} = 1 - t_{\text{decay}} \cdot f_{\text{burst}}. \quad (8.2)$$

Taking the measured values of the maximum and minimum horizontal bunch sizes $\sigma_{x,max}$ and $\sigma_{x,min}$ and the effective damping time $\tau_{x,eff}$ from AT simulations, this leads to

$$\sigma_{x,max}^2 = C + \sigma_{x,0}^2 \quad (8.3a)$$

$$\sigma_{x,min}^2 = C \cdot e^{-2t_{\text{decay}}/\tau_{x,eff}} + \sigma_{x,0}^2. \quad (8.3b)$$

From these equations, the bursting frequency f_{burst} can be calculated as

$$f_{\text{burst}} = -\frac{2}{\tau_{x,eff}(d+1) \ln \left[\frac{\sigma_{x,min}^2 - \sigma_{x,0}^2}{\sigma_{x,max}^2 - \sigma_{x,0}^2} \right]}. \quad (8.4)$$

To study this relation, the bursting frequency f_{burst} is calculated from measured bunch sizes and compared to the dominant frequency from the horizontal bunch size spectrogram. This spectrogram is calculated using Lomb periodograms [103]. For three different fills, this is shown in Fig. 8.9.

For the maximum and minimum bunch sizes, the 10th and 90th percentile are taken as a measure due to their robustness against outliers and noise. They are shown in the left column with the corresponding horizontal bunch size spectrograms shown in the right column. There, the black dots depict the bursting frequency calculated using Eq. (8.4). In general, the calculated frequency agrees reasonably well with the measured ones. An overestimation of f_{burst} , which occurs for higher bunch currents, can be due to an underestimation of the radiation damping because of an instability driven blow up

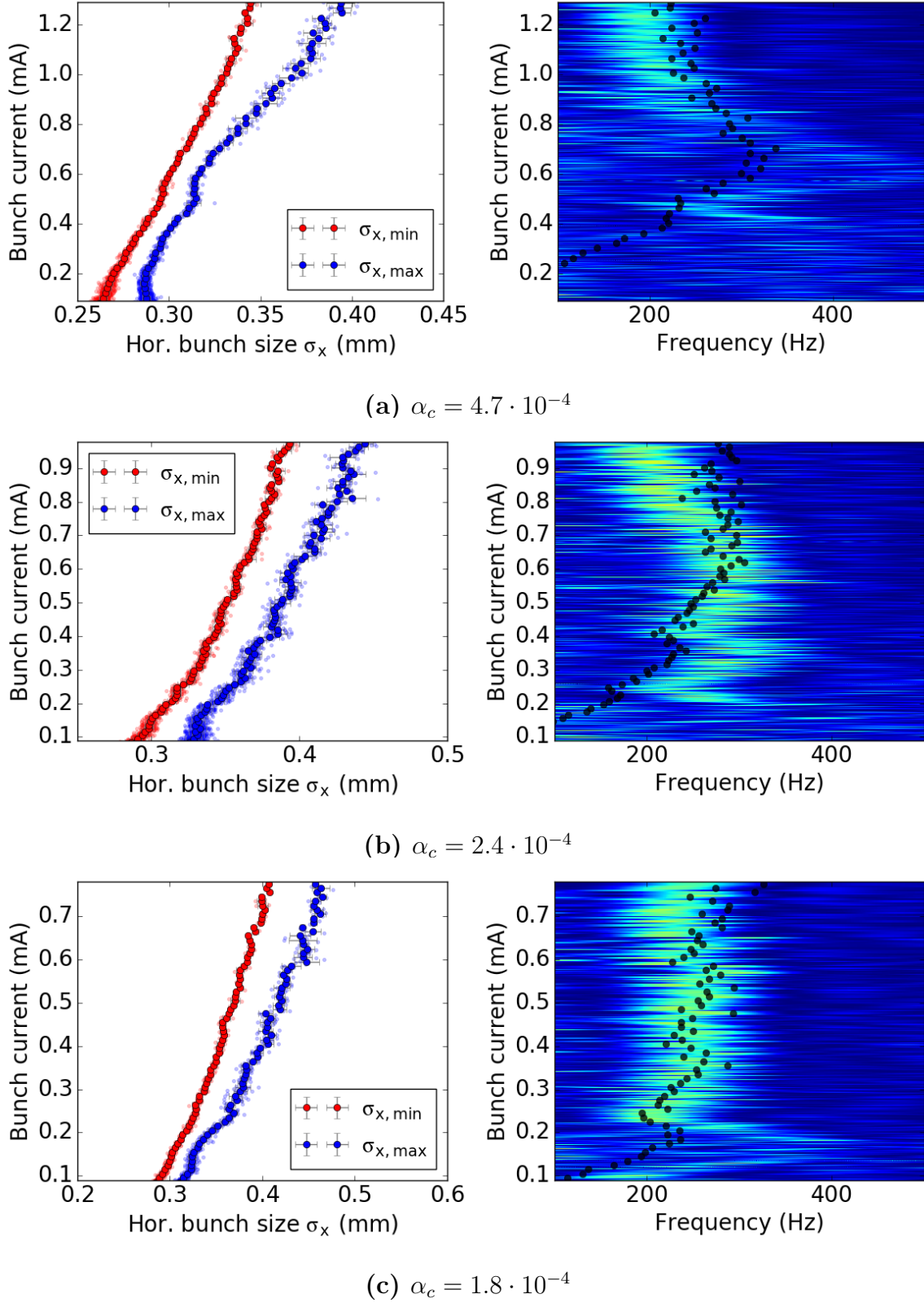


Figure 8.9.: Left column: Minimum and maximum horizontal bunch size plotted over three different bunch current decays depicted by the values for α_c . The individual data points are faded out and profile histogram applied to them. Right column: Color-coded horizontal bunch size spectrogram and bursting frequency f_{burst} calculated using Eq. (8.4).

working against the damping. For low bunch currents, the intensity of the bunch size fluctuation in the spectrogram tends to vanish.

In Fig. 8.9a, the bump of the dominant frequency in the spectrogram between 0.8 mA and 0.6 mA is not fully covered by the calculated bursting frequency which only reaches values of approx. 350 Hz, while the spectrogram show peaks above 400 Hz. In this case it is noteworthy, that the bunch size measurements was quite noisy which makes the determination of the maximum and minimum horizontal bunch size difficult as they suffer from the low signal-to-noise ratio (SNR) as well. Nevertheless, the bump can be at least described qualitatively by the calculated frequencies. For the other two cases, this smearing out of the spectrogram coupled to a disagreement with the calculated frequencies appears for bunch currents which are below 0.2 mA.

This is a hint, that the bursting frequency is mostly determined by the bunch current dependency of the horizontal bunch size (and thus the energy spread) for a constant damping time $\tau_{x,eff}$ or at least a constant product of $\tau_{x,eff} \cdot (d + 1) = \tilde{\tau}_{x,eff}$.

The bunch current dependency of the bunch size is defined by the impedance which describes the interaction of the bunch with its environment. Due to a current-dependent bunch lengthening, which was previously measured at KARA [40], the bunch spectrum changes with bunch current and thus also the overlap of this spectrum with the impedance changes.

To study this impedance in more detail, the impedance-related effects on the bunch size as well as the arrival time have been measured. They are discussed in the following.

8.3. Impedance studies

8.3.1. Incoherent synchrotron frequency shift

The synchrotron frequency given by Eq. (2.32) describes the coherent motion of the center of mass of an electron bunch. Apart from this coherent motion, there are also incoherent motions of the single electrons. This incoherent frequency shifts with bunch current and this frequency shift depends on the imaginary part of the storage ring impedance, see Sec. 4.2.2. While the coherent synchrotron oscillation is visible as a dipole motion of the bunch, the incoherent synchrotron frequencies of the particles within a bunch lead to higher order modes like e.g. the quadrupole mode which is depicted in Fig. 8.10.

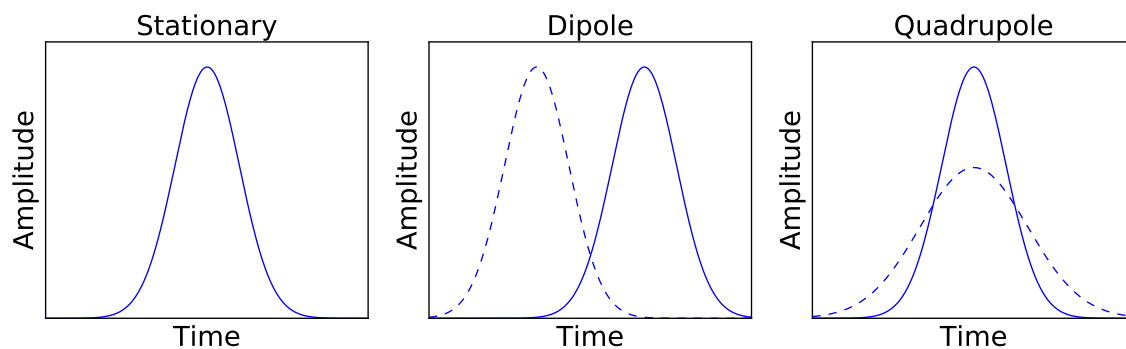


Figure 8.10.: Illustration of the first two eigenmodes of the synchrotron oscillation. While for the dipole mode the bunch length and energy spread are constant, both oscillate for the quadrupole mode.

As such a quadrupole oscillation is coupled to an oscillation of the bunch size, the incoherent synchrotron frequency can be determined from the horizontal bunch size measured by the FGC. Such a measurement is illustrated in Fig. 8.11. There, the machine settings ($\alpha_c = 2.9 \cdot 10^{-4}$ in combination with a low RF voltage V_{RF} : 250 kV) led to a strong synchrotron oscillation.

The top panel shows the time-domain data of the horizontal bunch position and size. While the horizontal bunch position oscillates with the coherent synchrotron frequency, the horizontal bunch size shows an oscillation with twice the incoherent synchrotron frequency. By comparing the two curves, it can be seen that the size does not oscillate with exactly twice the frequency of the position but with a slightly smaller frequency. To study this frequencies in more detail, Lomb periodograms are applied to the data, they are shown in the bottom panel. In addition to the FGC data, the corresponding FFT spectrum of the CSR recorded using a broadband Schottky detector is plotted. The position periodogram as well as the FFT of the CSR both have a peak at the

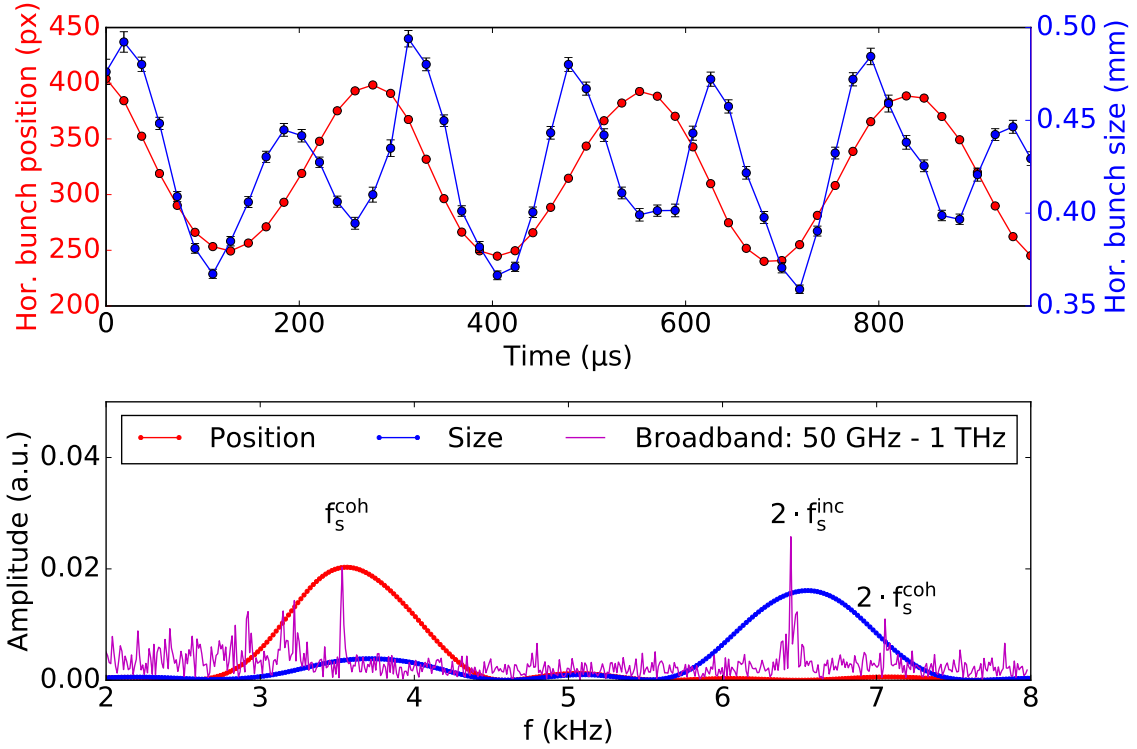


Figure 8.11.: Top panel: Horizontal bunch position and size in the time domain. The data points are connected by lines to guide the eye. Bottom panel: Lomb periodograms of the FGC data from the top panel and the corresponding fast Fourier transformation (FFT) of the CSR recorded with a broadband Schottky detector (CSR data: courtesy Miriam Brosi).

Beam parameters: $f_s = 3.5$ kHz, $V_{\text{RF}} = 250$ kV, $I_{\text{bunch}} = 1.63$ mA

coherent synchrotron frequency $f_s^{\text{coh}} = 3.5$ kHz. The second harmonic of the incoherent synchrotron oscillation is visible as peak on the bunch size periodogram as well as the CSR at a frequency of 6.6 kHz. This is significantly below $2 \cdot f_s^{\text{coh}}$. As discussed in Sec. 4.2.2, the difference Δf_s between the coherent and the incoherent synchrotron frequency depends on the imaginary part of the impedance and the bunch spectrum.

In this case, the incoherent synchrotron frequency is below the coherent one and thus $\Delta f_s < 0$. As $\cos(\phi_s) < 0$, this means that the inductive part of the impedance ($\text{Im}[Z(\omega)] > 0$) dominates, which leads to a bunch lengthening with current.

Mapping the incoherent synchrotron frequency over a bunch current range leads to the spectrograms of the horizontal bunch size as well as the CSR which are plotted in Fig. 8.12. The black dots in the horizontal bunch size periodogram (left panel) depict the frequencies with the highest amplitude as a measure for $2 \cdot f_s^{\text{inc}}$. Even if only a relatively small bunch current range is shown here, it can be seen that the incoherent synchrotron frequency is shifting towards higher values during the bunch current decay.

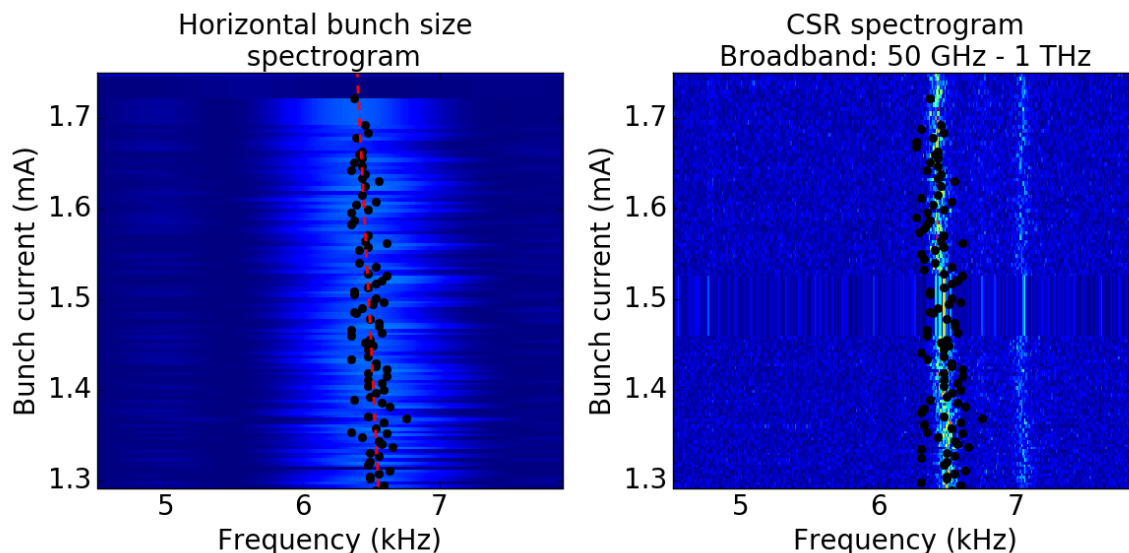


Figure 8.12.: Left panel: Spectrogram of the horizontal bunch size calculated using Lomb periodograms. The black dots illustrate the frequency for the maximum amplitude and the red dashed line depicts a fit according to Eq. (8.5). Right panel: corresponding CSR spectrogram recorded by a broadband Schottky detector, the black dots are the same as in the left panel (CSR data taken by Miriam Brosi).

The black dots coincide well with the corresponding line in the CSR spectrogram shown in the right panel.

A simple relation between the coherent and the incoherent synchrotron frequency is given by [104, Eq. (5)]

$$f_s^{\text{inc}} = f_s^{\text{coh}} \cdot \frac{1}{(1 - \lambda I_b)} \quad (8.5)$$

with λ as *bunch lengthening factor*. This function is fitted to the black dots in the left panel, the dashed red line illustrates this fit which leads to a value for λ of $-0.057 \pm 0.001 \text{ mA}^{-1}$.

Using the horizontal bunch size oscillation is one method to access the incoherent synchrotron frequency. Previous studies at KARA used either the method of resonant spin depolarisation [105] or the turn-by-turn beam position monitor (BPM) readout. The latter measurement were also conducted during the short-bunch operation, but with a higher synchrotron frequency of $f_s^{\text{coh}} = 9.6 \text{ kHz}$ and led to $\lambda = -0.024 \pm 0.001 \text{ mA}^{-1}$ [71]. This is significantly above the value for the FGC measurements and thus coupled to a weaker bunch lengthening. An even weaker – or almost no bunch lengthening – was seen, when the incoherent tune shift was studied at a beam energy of 2.5 GeV with *unsqueezed* and thus relatively long bunches using the resonant spin depolarisation method. This led to $\lambda = -0.0057 \pm 0.014 \text{ mA}^{-1}$ [104].

These results give a clear hint to a lengthening and widening of the bunch with bunch current, which is a signature for an inductive impedance of the storage ring ($\text{Im}[Z] > 0$). This agrees with previous measurements of the bunch lengthening at KARA using a Streak Camera [40].

To investigate the real part of the impedance, the shift of the synchronous phase of the electron bunch can be determined as it is discussed in the following.

8.3.2. Synchronous phase shift

As discussed in Sec. 5.1.3, the time-correlated single photon counting (TCSPC) system can be used for the measurement of the synchronous phase shift. This shift is a measure for the real or resistive part of the longitudinal impedance of a storage ring (see Sec. 4.2.1).

A very common method to study the synchronous phase shift is to use a streak camera (SC) and a filling pattern with one main bunch and – at least – one reference bunch with a very small current. The idea is, that the reference bunch current decays much slower and thus its phase does not change. Especially for the CSR impedance, this eventual drift of the reference bunch can be an issue. Simulations of this shift at KARA showed, that the shift of the reference bunch due to the parallel plates CSR impedance is very small for the cases discussed here [70].

Therefore, the measurements using the TCSPC were conducted using the reference bunch method to determine the arrival time difference $\Delta\tau$ as a measure for the synchronous phase, this is illustrated in Fig. 8.13.

Using the relation $\Delta\phi_\tau = \Delta\tau - T_{\text{RF}}$ allows to track the phase shift $\Delta\phi_\tau$ over bunch current. Previous measurements at KARA using a streak camera (SC) (See [40, Fig. 3.1] for schematics) are discussed in [67] and [33]. There, the method with the reference bunch was chosen as the timing stability of the SC can be insufficient for precise measurements of the bunch arrival times.

The technique of TCSPC allows to study the synchronous phase shift as well. As it measures the arrival time of all bunches in parallel, it allows to compare the relative timing (time difference $\Delta\tau$ between main and reference bunch) as well as the overall arrival time drift for the bunches. To check the consistency of the TCSPC data with previous SC measurements, several fills with a reference and a main bunch were studied. There, for each measured raw data histogram, the arrival time difference $\Delta\tau$ between the two bunches is determined. For one fill the arrival time difference $\Delta\tau$ is plotted over bunch current difference in Fig. 8.14.

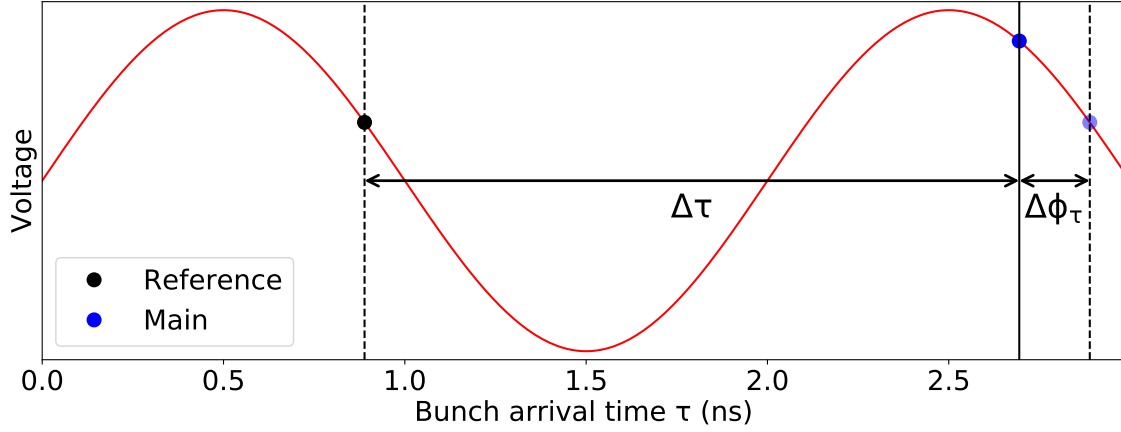


Figure 8.13.: Shift of the main bunch (blue) with respect to a reference bunch (black). To compensate the additional resistive energy losses, the main bunch passes the cavities at a higher voltage and is thus phase shifted by $\Delta\phi$ relative to the nominal phase, indicated by the shaded blue dot. To determine this phase shift, the time difference $\Delta\tau$ between the two bunches is measured.

As discussed in [67], a linear curve can be fitted to the data to get an – averaged – value for the loss factor k from the slope $\frac{d\tau}{dI}$ of the curve:

$$k = \frac{2\pi \cdot V_{\text{RF}} \cdot 184}{T_{\text{rev}}^2} \cos(\phi_s) \cdot \frac{d\tau}{dI}. \quad (8.6)$$

A different approach is conducted in [33]. There, the impedance of a broadband resonator and Gaussian bunches are assumed and the resulting loss factor is determined from fits. While the model of a broadband resonator was found to be not perfectly suitable to describe the impedance of KARA during the micro-bunching instability, it is nevertheless possible to fit a linear curve to the measurement data [33, Fig. 6.8]. Therefore, the data have been analysed again (see Sec. A.3 in the appendix for the SC data analysis).

The case with $f_s = 6.8 \text{ kHz}$ is illustrated in Fig. 8.15. Here, the linear fit leads to $\chi_{\text{red}}^2 = 0.95$. It is noteworthy that the values on the y-axis do not tend towards zero for a bunch current difference of 0 mA. This is due to the additional offset c in Eq. (A.2). As only the slope is relevant, this does not play a role.

Both measurement techniques give hint to a relatively linear shift of the synchronous phase with bunch current (see Fig. 8.14 for TCSPC and Fig. 8.15 for the SC). Only for low bunch currents, this behavior changes. In addition, the linear shift can be observed for different machine settings. The TCSPC as well as the (previous) SC measurements are summarized in Table 8.1.

Both techniques show an increase of the loss factor for a decreasing value of α_c which

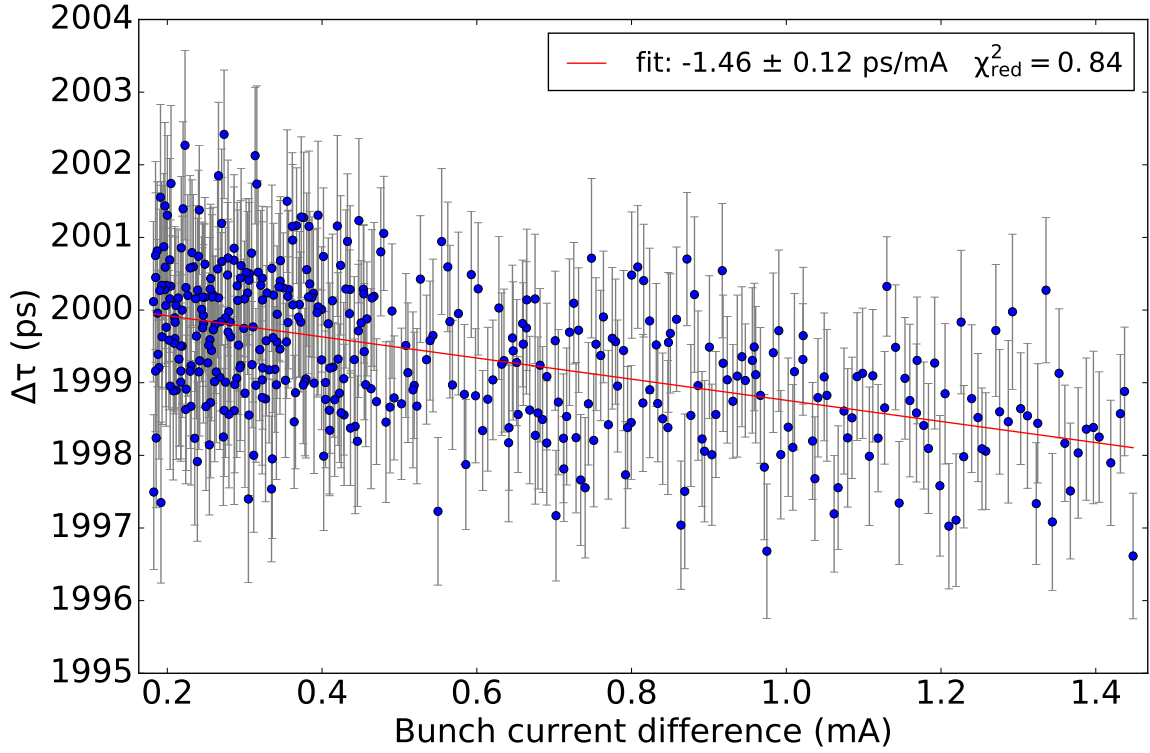


Figure 8.14.: Shift of the synchronous phase given by the arrival time difference $\Delta\tau$ over the bunch current difference between main and reference bunch. To determine the slope of the shift, a linear fit is applied to the data for bunch currents above the bursting threshold (Fill 6112 (see Table 8.1), $I_{\text{bthr}} = 0.19 \text{ mA}$).

is in agreement with the theory. For lower values of α_c , the bunches get shorter and thus sample a broader part of the impedance leading to an increase of the integral in Eq. (4.17).

For the SC measurements, the value for the RF voltage can only be estimated as these measurements have been done with a non-calibrated RF system. Therefore, the uncertainty of the RF voltage is assumed to be 50 kV.

The fills 6110 and 6111 have been taken with identical machine settings and also their loss factor coincides within the uncertainties. For the fills 6106 and 6112 this is not the case. While for both fills the loss factors are below the ones for fills 6110 and 6111, which had *shorter* bunches, they differ by more than $\pm 1\sigma$. In addition it is noteworthy that for fill 6106, the main and the reference bunch were separated by 3 RF buckets ($\approx 6 \text{ ns}$), while for the other fills a separation of one RF bucket was used.

The SC data also shows an increase of the loss factor for shorter bunches, except for fill 3431. There, the loss factor is 35.0 mV/ps, which is a factor 2 or 3 times larger than the value to be expected with regard to the other measurements.

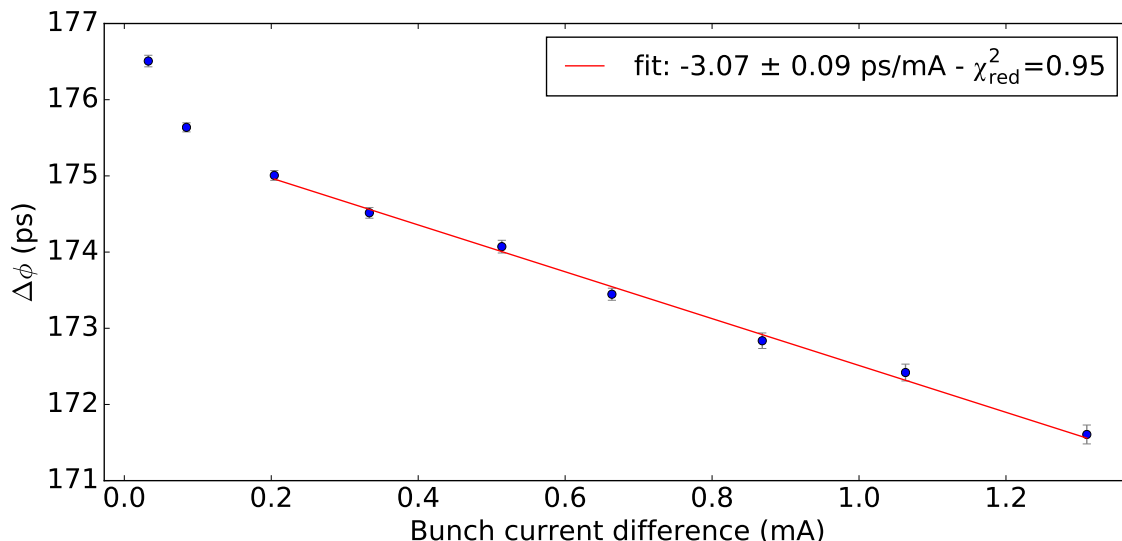


Figure 8.15.: Shift of the synchronous phase with bunch current measured with a SC [33]. To determine the slope of the shift, a linear fit is applied to the data for bunch currents above the bursting threshold (Fill 3430, $I_{\text{bthr}} = 0.26$ mA).

Possible reasons for the outliers are:

- The storage ring impedance was changed between the fills, e.g. by inserting a scraper into the beam pipe or by changes in the RF cavities that lead to a drastic increase of the energy loss due to the excitation of higher order modes. While the fills 6110 - 6112 were done consecutively, fill 6106 was done 24 hours before. During this period, small long-term temperature drifts can occur.
- While TCSPC also allows a precise measurement of the filling pattern, at the SC this is not possible as the relative distribution of the beam current on the main and the reference bunches can only be estimated from the longitudinal profile data. If this leads to an overestimation of the bunch current difference between main and reference bunch, this increases the slope and thus the loss factor.

In general, the error on the loss factor is larger for the TCSPC measurements than for the ones with the SC. This is assumed to be due to the better temporal resolution of the latter device. While at the streak camera, the temporal sampling interval is 0.7 ps (256 pixel cover 190 ps), the minimum bin width of the PicoHarp is 8 ps, which is one order of magnitude larger. Nevertheless, the precision for the TCSPC loss factor determination is remarkably good as e.g. the time range covered by the y-axis in Fig. 8.14 is only slightly above the width of one bin. In addition, the value of χ_{red}^2 implies an overestimation of the error on the arrival time difference $\Delta\tau$.

Table 8.1.: Machine parameters and corresponding loss factors for different fills.

Fill	E (GeV)	V_{RF} (kV)	ϕ_s ($^\circ$)	f_s (kHz)	α_c	k (V/pC)	Technique
6110	1.3	1500	178.3	7.0	$1.9 \cdot 10^{-4}$	33.1 ± 8.4	TCSPC
6111	1.3	1500	178.3	7.0	$1.9 \cdot 10^{-4}$	30.4 ± 5.6	TCSPC
6106	1.3	1500	178.3	11.3	$5.1 \cdot 10^{-4}$	26.9 ± 3.6	TCSPC
6112	1.3	1500	178.3	11.5	$5.3 \cdot 10^{-4}$	18.6 ± 1.6	TCSPC
3430	1.3	~ 800	~ 176.7	6.8	$\sim 3.5 \cdot 10^{-4}$	20.9 ± 1.5	SC [33]
3429	1.3	~ 800	~ 176.7	8.4	$\sim 5.3 \cdot 10^{-4}$	17.2 ± 1.4	SC [33]
3431	1.3	~ 800	~ 176.7	15.4	$\sim 1.8 \cdot 10^{-3}$	35.0 ± 2.6	SC [33]
3428	1.3	~ 800	~ 176.7	31.5	$\sim 7.5 \cdot 10^{-3}$	9.2 ± 0.9	SC [33]

Nevertheless, the measurements discussed above show, that the loss factor k is increasing with decreasing bunch length. In addition, it can be assumed to be constant as the synchronous phase shifts linearly with bunch current. This is a signature for an energy loss – given by $\int_0^\infty \text{Re} [Z(\omega)] \mathcal{F}(\omega) d\omega$ – which is proportional to the bunch current.

8.4. Short bunch-length bursting

In Sec. 7.4 it was shown that the energy spread remains constant below the bursting threshold. For KARA, this is only the case if the machine settings lead to a momentum compaction factor $\alpha_c > 2.64 \cdot 10^{-4}$ [106]. If α_c is below this value, the occurrence of another instability below the *main* bursting threshold can be observed. During this instability the energy spread is expected to increase again.

This weak instability – referred to as *short bunch-length bursting* – was predicted by numerical simulations [56] and experimentally studied at KARA using CSR measurements [106]. Using the FGC now allowed first experimental studies of the energy spread during this instability.

The low currents for which the short bunch-length bursting occurs are challenging due to the corresponding low intensities of the measured synchrotron radiation. Therefore, studies with a single-turn resolution are not yet feasible, but by taking the average horizontal bunch size for each FGC image as a measure for the overall energy spread increase, this re-increase of the energy spread can be confirmed as is shown in Fig. 8.16.

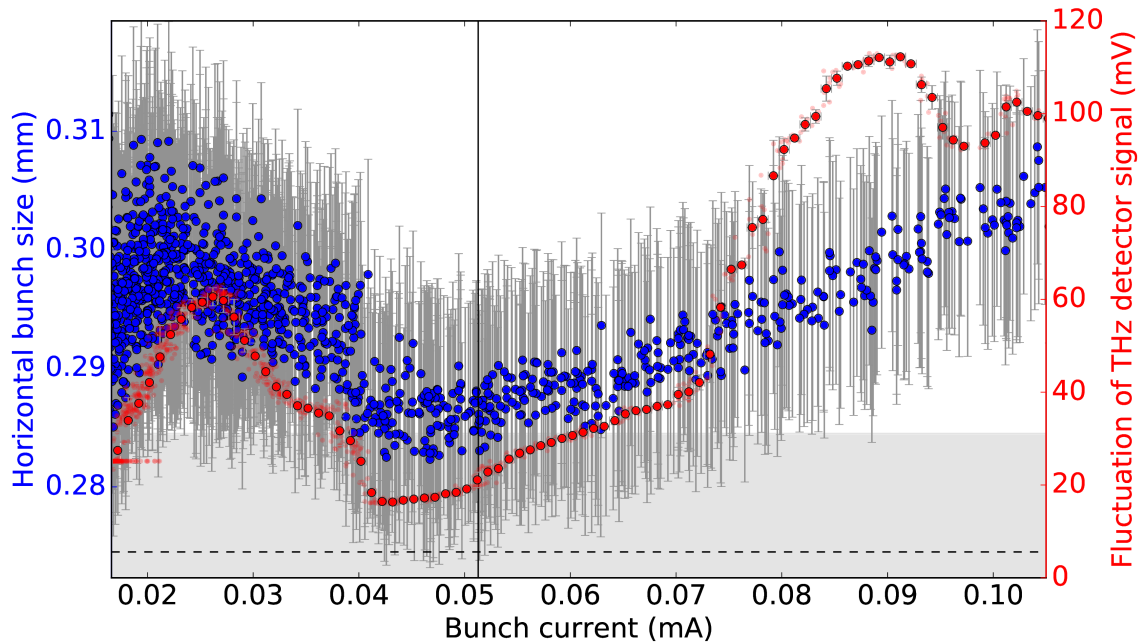


Figure 8.16.: Mean horizontal bunch size (blue) and corresponding CSR fluctuation (red) as bursting strength plotted over beam current. The vertical black line depicts the *main* bursting threshold while the horizontal dashed line and the grey bar depicts the equilibrium horizontal bunch size and the corresponding error, respectively. For bunch currents below 0.04 mA, the bursting strength increases again, the same holds for the horizontal bunch size (CSR data: courtesy Miriam Brosi).

Beam parameters: $f_s = 6.88$ kHz, $V_{RF} = 1500$ kV, $\alpha_c = 1.8 \cdot 10^{-4}$

Here, the machine settings led to $\alpha_c \sim 1.8 \cdot 10^{-4}$. Below the bursting threshold, the horizontal bunch size (and thus the energy spread) remains constant, but for bunch currents below 0.004 mA it increases again. This increase coincides with the increase of the CSR bursting strength. This strength is determined by the fluctuation of the CSR intensity in a certain frequency range [47]. If no CSR is emitted, this fluctuation should be approximately zero. This parallel increase of the energy spread as well as the bursting strength is a signature of the short bunch-length bursting.

8.5. Outlook

The promising results discussed in Sec. 8.1.3 already showed the direction towards the future: Using a KALYPSO based system for measurements of the horizontal bunch profile to study the energy spread dynamics. This will allow to overcome the limitations of the existing setup and in addition, this system is quasi-identical to the one used for electro-optical spectral decoding (EOSD). This simplifies the synchronisation a lot as the rotating mirror is no longer required.

Future versions of KALYPSO will use a new silicon sensor which has smaller pixels to increase the readout speed and to reduce the pixel noise to provide a higher sensitivity. In addition, the usage of anti-reflective coatings is foreseen [82].

In combination with the KAPTURE system, it will be possible to study energy spread, bunch length and CSR emission for long time scales with a single turn resolution. This will allow studies of the longitudinal beam parameters in unprecedented detail and is an important step towards tomographical studies of the longitudinal phase space.

9. Summary

If the momentum compaction factor α_c is reduced by changes of the quadrupole and sextupole magnets, the micro-bunching instability can occur in the KIT storage ring KARA. There, the bunch emits coherent synchrotron radiation (CSR) and interacts with its previously emitted CSR, which leads to the formation of sub-structures on the bunch profile. As the wavelength of the emitted radiation depends on the time-scale of the emitting structure, this coherent radiation is in the frequency range of Terahertz. Due to the dynamics of the instability, radiation is not emitted constantly, but fluctuates with period lengths in the range of milliseconds. This is referred to as *bursting*. The micro-bunching instability is coupled to a modulation of the energy spread and thus the energy spread is an important parameter to investigate and map the dynamics of the instability.

One requirement for experimental studies of the micro-bunching instability is a precise knowledge of the bunch current. Therefore, a setup based on time-correlated single photon counting was installed. To compensate for eventual dead-time effects which distort the time-correlated single photon counting (TCSPC) measurements, a dedicated dead-time correction scheme was developed and successfully tested. In addition, TCSPC also allows measurements of the synchronous phase shift. To achieve this, exponentially modified Gaussians are fitted to the peaks in the raw data histogram. They take the detector characteristics into account and lead to better results compared to fitting purely Gaussian curves.

In the scope of this thesis, time-resolved studies of the micro-bunching instability have been done with special focus on the energy spread. The energy spread cannot be measured directly, but can be accessed by studies of the horizontal bunch size in a dispersive section of the storage ring. To allow time-resolved studies of the horizontal bunch size, a setup based on a fast-gated intensified camera (FGC) and a fast rotating mirror was designed and commissioned. The camera has an image intensifier that can be switched on and off within 2 ns. Therefore, the image intensifier acts as a pulse picker for one bunch in a multi-bunch fill. The combination of this *gating* with the fast rotating mirror allows to record single-turn images of one bunch. This enables to track the horizontal bunch profile for a selected number of turns. In case of KARA, the minimum gate separation is 6 turns. Another limitation of the setup is the number of spots that can be placed on the camera sensor. Thus, there is a trade-off between a

good temporal resolution and long time-ranges required beforehand of a measurement. To get the horizontal bunch profile from the raw data, a dedicated data analysis scheme was developed. As the bunch is moving during the image acquisition in the same plane as its profile is intended to be measured, the filament beam spread function (FBSF) has to be taken into account. It is determined from simulations of the optical setup and the imaging process. For sake of efficiency and robustness, the horizontal bunch size is determined by fitting a convolution of a Gaussian with the FBSF to the data.

In addition to the determination of the horizontal bunch size, also a timing calibration with respect to other detector systems was done. As the FGC setup has some intrinsic mechanical and electrical delays, these delays have to be compensated for synchronous measurements. This synchronisation is done using a dedicated hardware synchronisation scheme based on the timing system. To calibrate the synchronisation, the low-level RF (LLRF) system was used to trigger steps in the RF phase. Those steps lead to the onset of a strong synchrotron oscillation that can be detected by the various detector systems.

A very important tool for beam dynamics studies are simulations of the accelerator. In the scope of this thesis, the Accelerator Toolbox for MATLAB (AT) was used. Combined with Linear Optics for Closed Orbits (LOCO) fits to determine the quadrupole strengths, this enabled tracking studies for the short-bunch operation mode of KARA. The simulations include the ability to study the equilibrium beam size at the imaging source point of the FGC setup and to benchmark this size against measured values. It could be shown that the calculated horizontal bunch sizes agree well with the measured values.

With the fully synchronised setups, it is possible to qualitatively study the energy spread synchronously to the emission of CSR. It could be shown that the energy spread as well as the CSR have the same modulation period length. These energy spread fluctuations are due to the interplay of the instability which leads to a blow up of the energy spread at the onset of the burst. Radiation damping then leads to a shrinking of the energy spread and if the energy spread reaches the instability threshold again, the bunch becomes unstable and the onset of the next burst is triggered. Using KALYPSO allows more detailed studies of the onsets of the individual CSR bursts as it enables turn-by-turn studies of the horizontal bunch size.

The temporal pattern of this bursting behaviour is determined by the radiation damping and the instability induced blow-up. By studying the damping of the horizontal bunch size using a FGC it was shown that this damping is mostly determined by the *classical* radiation damping which does not take any coherent radiation effects into account. The impedance characteristics have been studied using the FGC as well as the TCSPC system. With the FGC it is possible to map the incoherent synchrotron frequency and its shift with bunch current, which allows to draw conclusions on the imaginary

part of the impedance. These studies showed, that the impedance is mostly inductive ($\text{Im} [Z(\omega)] > 0$). For the real or resistive part of the impedance, the synchronous phase shift has been investigated. It could be shown that the energy loss due to the resistive part of the impedance increases with decreasing bunch lengths.

Thanks to its high dynamic range, the FGC finally allowed a first experimental observation of the short bunch-length bursting on the energy spread. This weak instability was observed as increase of the horizontal bunch size for the same bunch current range, where also the CSR fluctuation intensity showed an additional increase.

Acronyms

APD avalanche photo diode.

AT Accelerator Toolbox for MATLAB.

BPM beam position monitor.

CSR coherent synchrotron radiation.

DAQ data acquisition.

DCCT DC current transformer.

EOSD electro-optical spectral decoding.

EVG event generator.

EVR event receiver.

FBSF filament beam spread function.

FFT fast Fourier transformation.

FGC fast-gated intensified camera.

FWHM full width at half maximum.

IR infrared.

KALYPSO Karlsruhe line array for linear spectroscopy.

KAPTURE Karlsruhe pulse taking ultra-fast readout electronics.

KARA Karlsruhe research accelerator.

KIT Karlsruhe Institute of Technology.

Linac linear accelerator.

LLRF low-level RF.

LOCO Linear Optics for Closed Orbits.

MCP micro-channel plate.

ND neutral density.

ORM orbit response matrix.

PDF probability density function.

PSF point spread function.

RF radio frequency.

RMS root mean square.

SC streak camera.

SNR signal-to-noise ratio.

SPAD single photon avalanche diode.

TCSPC time-correlated single photon counting.

TLU trigger logic unit.

VLD visible light diagnostics.

Bibliography

- [1] F. R. Elder et al. “Radiation from Electrons in a Synchrotron”. In: *Phys. Rev.* 71 (11 1947), pp. 829–830. DOI: 10.1103/PhysRev.71.829.5.
- [2] E. M. Rowe and F. E. Mills. “Tantalus. 1. A Dedicated Storage Ring Synchrotron Radiation source”. In: *Part. Accel.* 4 (1973), pp. 211–227. URL: <http://cds.cern.ch/record/1107919>.
- [3] J. S. Nodvick and D. S. Saxon. “Suppression of Coherent Radiation by Electrons in a Synchrotron”. In: *Phys. Rev.* 96 (1 1954), pp. 180–184. DOI: 10.1103/PhysRev.96.180.
- [4] G. Carr et al. “Observation of coherent synchrotron radiation from the NSLS VUV ring”. In: *Nuclear Instruments and Methods in Physics Research Section A: Accelerators, Spectrometers, Detectors and Associated Equipment* 463.1 (2001), pp. 387–392. DOI: 10.1016/S0168-9002(01)00521-6.
- [5] U. Arp et al. “Spontaneous coherent microwave emission and the sawtooth instability in a compact storage ring”. In: *Phys. Rev. ST Accel. Beams* 4 (5 2001), p. 054401. DOI: 10.1103/PhysRevSTAB.4.054401.
- [6] J. M. Byrd et al. “Observation of Broadband Self-Amplified Spontaneous Coherent Terahertz Synchrotron Radiation in a Storage Ring”. In: *Phys. Rev. Lett.* 89 (22 2002), p. 224801. DOI: 10.1103/PhysRevLett.89.224801.
- [7] M. Abo-Bakr et al. “Coherent Emission of Synchrotron Radiation and Longitudinal Instabilities”. In: *Proceedings of PAC’03*. Vol. 5. IEEE. 2003, pp. 3023–3025. DOI: 10.1109/PAC.2003.1289801.
- [8] A.-S. Müller et al. “Far infrared coherent synchrotron edge radiation at ANKA”. In: *Proceedings of PAC’05*. IEEE. 2005, pp. 2518–2520. DOI: 10.1109/PAC.2005.1591164.
- [9] W. Shields et al. “Microbunch Instability Observations from a THz Detector at Diamond Light Source”. In: *Journal of Physics: Conference Series* 357.1 (2012), p. 012037. DOI: 10.1088/1742-6596/357/1/012037.
- [10] C. Evain et al. “Spatio-temporal dynamics of relativistic electron bunches during the micro-bunching instability in storage rings”. In: *EPL (Europhysics Letters)* 98.4 (2012), p. 40006. DOI: 10.1209/0295-5075/98/40006.

- [11] G. Stupakov and S. Heifets. “Beam instability and microbunching due to coherent synchrotron radiation”. In: *Phys. Rev. ST Accel. Beams* 5 (5 2002), p. 054402. DOI: 10.1103/PhysRevSTAB.5.054402.
- [12] M. Venturini and R. Warnock. “Bursts of Coherent Synchrotron Radiation in Electron Storage Rings: A Dynamical Model”. In: *Phys. Rev. Lett.* 89 (22 2002), p. 224802. DOI: 10.1103/PhysRevLett.89.224802.
- [13] K. L. F. Bane, K. Oide, and M. Zobov. “Impedance calculation and verification in storage rings”. In: *1st CARE-HHH-APD Workshop on Beam Dynamics in Future Hadron Colliders and Rapidly Cycling High-Intensity Synchrotrons*. CERN, 2005. DOI: 10.5170/CERN-2005-006.143.
- [14] U. Arp et al. “Spontaneous coherent microwave emission and the sawtooth instability in a compact storage ring”. In: *Phys. Rev. ST Accel. Beams* 4 (5 2001), p. 054401. DOI: 10.1103/PhysRevSTAB.4.054401.
- [15] J. Corbett et al. “Bunch Length and Impedance Measurements at SPEAR3”. In: *Proceedings of EPAC’08*. 2011, pp. 1595–1597.
- [16] M. Minty et al. “Using a fast-gated camera for measurements of transverse beam distributions and damping times”. In: *AIP Conference Proceedings*. Vol. 281. 1. AIP. 1992, pp. 158–167.
- [17] J. Flanagan et al. “High-speed gated camera observations of transverse beam size along bunch train at the KEKB B-factory”. In: *Proceedings of EPAC’00*. 2000, pp. 1119–1121.
- [18] R. Warnock. “Study of bunch instabilities by the nonlinear Vlasov-Fokker-Planck equation”. In: *Nucl. Instrum. Meth.* A561 (2006), pp. 186–194. DOI: 10.1016/j.nima.2006.01.041.
- [19] A. Fisher et al. “Turn-by-Turn Imaging of the Transverse Beam Profile in PEP-II”. In: *AIP Conference Proceedings*. Vol. 868. 1. AIP. 2006, pp. 303–312. DOI: 10.1063/1.2401418.
- [20] W. Cheng et al. “Fast-gated camera measurements in SPEAR3”. In: *Proceedings of PAC’09*. 2009, pp. 4015–4017.
- [21] M. Tanabashi et al. “Review of Particle Physics”. English (US). In: *Physical Review D* 98.3 (2018). DOI: 10.1103/PhysRevD.98.030001.
- [22] K. Wille. *Physik der Teilchenbeschleuniger und Synchrotronstrahlungsquellen*. Teubner Studienbücher, 1996.
- [23] P. J. Mohr, D. B. Newell, and B. N. Taylor. “CODATA recommended values of the fundamental physical constants: 2014”. In: *Journal of Physical and Chemical Reference Data* 45.4 (2016), p. 043102. DOI: 10.1063/1.4954402.

-
- [24] H. Wiedemann. *Particle accelerator physics*. Springer, 2015. DOI: 10.1007/978-3-319-18317-6.
- [25] V. Kain. “Beam Dynamics and Beam Losses - Circular Machines”. In: *2014 Joint International Accelerator School: Beam Loss and Accelerator Protection, 5-14 Nov 2014*. License: CC BY 4.0: <https://creativecommons.org/licenses/by/4.0/legalcode>. 2016, pp. 21–38. DOI: 10.5170/CERN-2016-002.21.
- [26] B. Nash et al. “New functionality for beam dynamics in Accelerator Toolbox (AT)”. In: *Proceedings of IPAC’15. JACoW*, 2015, pp. 113–116. DOI: 10.18429/JACoW-IPAC2015-MOPWA014.
- [27] A. Fabris et al. “Low level RF System for the ANKA Storage Ring”. In: *Proceedings of EPAC’98*. 1998, pp. 1761–1763.
- [28] D. Einfeld et al. “Status of the RF System for the ANKA Storage Ring”. In: *Proceedings of PAC’99*. 1999, pp. 809–811.
- [29] A. Hofmann. “Beam instabilities”. In: *CAS - CERN Accelerator School : Course on Synchrotron Radiation and Free-Electron Lasers*. CERN, 2005, pp. 139–185. DOI: 10.5170/CERN-2005-012.139.
- [30] K. W. Robinson. “Radiation effects in circular electron accelerators”. In: *Physical Review* 111.2 (1958), p. 373.
- [31] A. Wolski. “Low-emittance Storage Rings”. In: *CAS - CERN Accelerator School: Advanced Accelerator Physics, 18-29 Aug 2013*. 2014, pp. 254–294. DOI: 10.5170/CERN-2014-009.245.
- [32] *ANKA instrumentation book 2012*. [Online; accessed 2019-06-27]. ANKA synchrotron radiation facility, 2012. URL: https://www.anka.kit.edu/downloads_anka/instrumentation_books/Instrumentationbook-2012.pdf.
- [33] A. Hofmann. “Implementierung eines Single- und Multibunchbetriebes am ANKA Speicherring”. Ph. D. thesis. Karlsruhe Institute of Technology, 2011.
- [34] D. Einfeld et al. “Status of the injector system for the synchrotron light source ANKA”. In: *Proceedings of PAC’99*. 1999, pp. 2427–2429.
- [35] KIT IBPT construction department. 2015.
- [36] A.-S. Müller et al. “Experimental Aspects of CSR in the ANKA Storage Ring”. In: *ICFA Beam Dynamics Newsletter* 57 (2012), pp. 154–165. URL: https://icfa-usa.jlab.org/archive/newsletter/icfa_bd_nl_57.pdf.
- [37] S. Kramer and J. Murphy. “Variable momentum compaction lattice studies”. In: *Particle Accelerator Conference, 1999. Proceedings of the 1999*. Vol. 1. IEEE. 1999, pp. 140–142. DOI: 10.1109/PAC.1999.795646.

- [38] B. Kehrer et al. “Visible Light Diagnostics at the ANKA Storage Ring”. In: *Proceedings of IPAC’15*. JACoW, 2015, pp. 866–868. DOI: 10.18429/JACoW-IPAC2015-MOPHA037.
- [39] N. Hiller et al. “Status of Bunch Deformation and Lengthening Studies at the ANKA Storage Ring”. In: *Proceedings of IPAC’11*. 2011, pp. 2951–2953. URL: <http://accelconf.web.cern.ch/AccelConf/IPAC2011/papers/thpc021.pdf>.
- [40] N. Hiller. “Electro-Optical Bunch Length Measurements at the ANKA Storage Ring”. Ph. D. thesis. Karlsruhe Institute of Technology, 2011. DOI: 10.5445/IR/1000041159.
- [41] K. Y. Ng. *Physics of Intensity Dependent Beam Instabilities*. 2002. URL: http://lss.fnal.gov/cgi-bin/find_paper.pl?fn-0713.
- [42] A. W. Chao and M. Tigner. *Handbook of accelerator physics and engineering*. World Scientific, 1999.
- [43] V. Judin. “Untersuchung von Bunch-Bunch-Wechselwirkungen und des Einflusses der geometrischen Impedanz bei der Erzeugung kohärenter THz-Strahlung”. Ph. D. thesis. Karlsruhe Institute of Technology, 2013.
- [44] E. L. Saldin, E. A. Schneidmiller, and M. Yurkov. “On the coherent radiation of an electron bunch moving in an arc of a circle”. In: *Nuclear Instruments and Methods in Physics Research Section A: Accelerators, Spectrometers, Detectors and Associated Equipment* 398.2-3 (1997), pp. 373–394. DOI: 10.1016/S0168-9002(97)00822-X.
- [45] T. Agoh. “Steady fields of coherent synchrotron radiation in a rectangular pipe”. In: *Physical Review Special Topics-Accelerators and Beams* 12.9 (2009), p. 094402. DOI: 10.1103/PhysRevSTAB.12.094402.
- [46] J. Murphy, R. Gluckstern, and S. Krinsky. “Longitudinal wake field for an electron moving on a circular orbit”. In: *Part. Accel.* 57.BNL-63090 (1996), pp. 9–64.
- [47] M. Brosi et al. “Fast mapping of terahertz bursting thresholds and characteristics at synchrotron light sources”. In: *Phys. Rev. Accel. Beams* 19 (11 2016), p. 110701. DOI: 10.1103/PhysRevAccelBeams.19.110701.
- [48] G. Rehm, C. Bloomer, and C. Thomas. “Loss Factor Measurement using Time Correlated Single Photon Counting of Synchrotron Radiation”. In: *Proceedings of DIPAC’11*. 2011, pp. 110–112.

-
- [49] P. Schönfeldt et al. “Parallelized Vlasov-Fokker-Planck solver for desktop personal computers”. In: *Phys. Rev. Accel. Beams* 20 (3 2017), p. 030704. DOI: 10.1103/PhysRevAccelBeams.20.030704.
- [50] P. Krejcik et al. “High intensity bunch length instabilities in the SLC damping rings”. In: *Proceedings of PAC’93*. IEEE. 1993, pp. 3240–3242.
- [51] F. Caspers and P. Kowina. “RF Measurement Concepts”. In: (2014). DOI: 10.5170/CERN-2014-009.101.
- [52] M. Caselle et al. “An ultra-fast digitizer with picosecond sampling time for Coherent Synchrotron Radiation”. In: *Real Time Conference (RT), 2014 19th IEEE-NPSS*. IEEE. 2014, pp. 1–3. DOI: 10.1109/RTC.2014.7097535.
- [53] M. Caselle et al. “KAPTURE-2. A picosecond sampling system for individual THz pulses with high repetition rate”. In: *Journal of Instrumentation* 12.01 (2017), p. C01040. DOI: 10.1088/1748-0221/12/01/C01040.
- [54] A. W. Chao and J. Gareyte. “Scaling law for bunch lengthening in SPEAR II”. In: *Part. Accel.* 25 (1990), pp. 229–234. URL: <http://cds.cern.ch/record/210836>.
- [55] J. L. Steinmann et al. “Continuous bunch-by-bunch spectroscopic investigation of the microbunching instability”. In: *Phys. Rev. Accel. Beams* 21 (11 2018), p. 110705. DOI: 10.1103/PhysRevAccelBeams.21.110705.
- [56] K. Bane, Y. Cai, and G. Stupakov. “Threshold studies of the microwave instability in electron storage rings”. In: *Physical Review Special Topics-Accelerators and Beams* 13.10 (2010), p. 104402. DOI: 10.1103/PhysRevSTAB.13.104402.
- [57] W. Becker. *Advanced time-correlated single photon counting techniques*. Vol. 81. Springer Science & Business Media, 2005. DOI: 10.1007/978-3-319-14929-5.
- [58] ID QUANTIQUE SA. *ID100 Visible Single-Photon Detector*. [Online; accessed 2019-06-27]. URL: <https://www.idquantique.com/single-photon-systems/products/id100/>.
- [59] PicoQuant GmbH. *PicoHarp 300 - Stand Alone TCSPC module with USB interface*. [Online; accessed 2019-06-27]. URL: <https://www.picoquant.com/images/uploads/downloads/picoharp300.pdf>.
- [60] S. Cova, A. Longoni, and A. Andreoni. “Towards picosecond resolution with single photon avalanche diodes”. In: *Review of Scientific Instruments* 52.3 (1981), pp. 408–412. eprint: <http://aip.scitation.org/doi/pdf/10.1063/1.1136594>. DOI: 10.1063/1.1136594.

- [61] M. Ghioni et al. “Progress in silicon single-photon avalanche diodes”. In: *IEEE Journal of selected topics in quantum electronics* 13.4 (2007), pp. 852–862. DOI: 10.1109/JSTQE.2007.902088.
- [62] M. Patting et al. “Dead-time effects in TCSPC data analysis”. In: *International Congress on Optics and Optoelectronics*. International Society for Optics and Photonics. 2007, pp. 658307–658307. DOI: 1117/12.722804.
- [63] B. Kehrer et al. “Filling Pattern Measurements Using Dead-Time Corrected Single Photon Counting”. In: *Proceedings of IPAC’18*. JACoW, 2018, pp. 2219–2222. DOI: 10.18429/JACoW-IPAC2018-WEPAL027.
- [64] M. Brosi et al. “Studies of the micro-bunching instability in multi-bunch operation at the ANKA storage ring”. In: *Proceedings of IPAC’17*. 2017, pp. 3645–3648. DOI: 10.18429/JACoW-IPAC2017-THOBA1.
- [65] BERGOZ Instrumentation. *Parametric current transformer user’s manual*. Rev. 3.1. 1998.
- [66] K. Wittenburg. “Beam halo and bunch purity monitoring”. In: *CAS - CERN Accelerator School: Course on Beam Diagnostics, 28 May - 6 Jun 2008*. CERN, 2009, pp. 557–580. DOI: 10.5170/CERN-2009-005.557.
- [67] P. F. Tavares et al. “Beam coupling impedance measurements at the ANKA electron storage ring”. In: *Proceedings of IPAC’10*. 2010, pp. 1982–1984.
- [68] E. Grushka. “Characterization of exponentially modified Gaussian peaks in chromatography”. In: *Analytical Chemistry* 44.11 (1972), pp. 1733–1738. DOI: 10.1021/ac60319a011.
- [69] W. H. Press et al. *Numerical recipes in C*. Vol. 2. Cambridge university press Cambridge, 1992.
- [70] P. Schönfeldt et al. “Study of the influence of the CSR impedance on the synchronous phase shift at KARA”. In: *Proceedings of IPAC’18*. 2018, pp. 2223–2226. DOI: 10.18429/JACoW-IPAC2018-WEPAL028.
- [71] P. Schütze. *Transversale Strahldynamik bei der Erzeugung kohärenter Synchrotronstrahlung*. BestMasters. Springer, 2017. DOI: 10.1007/978-3-658-20386-3.
- [72] Andor Technology Ltd. [Online; accessed 2019-06-27]. URL: <https://andor.oxinst.com/products/istar-intensified-cameras>.
- [73] P. Schütze et al. “A Fast Gated Intensified Camera Setup for Transversal Beam Diagnostics at the ANKA Storage Ring”. In: *Proceedings of IPAC’15*. License: CC BY 3.0: <https://creativecommons.org/licenses/by/3.0/legalcode>. JACoW, 2015, pp. 872–875. DOI: 10.18429/JACoW-IPAC2015-MOPHA039.

-
- [74] A. Hofmann and F. Méot. “Optical resolution of beam cross-section measurements by means of synchrotron radiation”. In: *Nuclear Instruments and Methods in Physics Research* 203.1-3 (1982), pp. 483–493. DOI: 10.1016/0167-5087(82)90663-9.
- [75] T. Mitsuhashi. “Spatial coherency of the synchrotron radiation at the visible light region and its application for the electron beam profile measurement”. In: *Proceedings of PAC’97*. IEEE, 1997, pp. 766–768.
- [76] Å. Andersson et al. “Electron beam profile measurements with visible and X-Ray synchrotron radiation at the Swiss Light Source”. In: *Proceedings of EPAC’06*. 2006, pp. 1223–1225.
- [77] J. C. Bergstrom and J. M. Vogt. “The optical diagnostic beamline at the Canadian Light Source”. In: *Nuclear Instruments and Methods in Physics Research Section A: Accelerators, Spectrometers, Detectors and Associated Equipment* 562.1 (2006), pp. 495–512. DOI: 10.1016/j.nima.2006.02.200.
- [78] Å. Andersson and J. Tagger. “Beam profile measurements at MAX”. In: *Nuclear Instruments and Methods in Physics Research Section A: Accelerators, Spectrometers, Detectors and Associated Equipment* 364.1 (1995), pp. 4–12. DOI: 10.1016/0168-9002(95)00221-9.
- [79] Optical Engineering Software. *OpTaliX Pro*. 2013. URL: <http://www.optenso.com>.
- [80] W. D. Duncan and G. P. Williams. “Infrared synchrotron radiation from electron storage rings”. In: *Appl. Opt.* 22.18 (1983), pp. 2914–2923. DOI: 10.1364/AO.22.002914.
- [81] P. Young. *Everything you wanted to know about Data Analysis and Fitting but were afraid to ask*. 2012. arXiv: 1210.3781.
- [82] M. Caselle et al. “Single-shot longitudinal beam profile and terahertz diagnostics at MHz-towards GHz-rates with high-throughput electronics”. In: *Proceedings of IBIC’17*. JACoW, 2018, pp. 136–140. DOI: 10.18429/JACoW-IBIC2017-TU2AB3.
- [83] L. Rota. “KALYPSO, a novel detector system for high-repetition rate and real-time beam diagnostics”. Ph. D. thesis. Karlsruhe Institute of Technology, 2017.
- [84] RedPitaya. URL: <http://www.redpitaya.com>.
- [85] B. Kehrer et al. “Simultaneous Detection of Longitudinal and Transverse Bunch Signals at ANKA”. In: *Proceedings of IPAC’16*. JACoW, 2016, pp. 109–111. DOI: 10.18429/JACoW-IPAC2016-MOPMB014.
- [86] A. Hofmann et al. “Single bunch operation at ANKA: Gun performance, timing and first results”. In: *Proceedings of IPAC’10*. 2010, pp. 924–926.

- [87] A. Terebilo. “Accelerator Toolbox for MATLAB”. In: *SLAC-PUB-8732* (2001).
- [88] G. Portmann, J. Corbett, and A. Terebilo. “An accelerator control middle layer using MATLAB”. In: *Proceedings of PAC’05*. 2005, pp. 4009–4011.
- [89] S. Marsching et al. “First experience with the MATLAB middle layer at ANKA”. In: *Proceedings of ICALEPS’11*. Vol. 11. 2011, p. 253.
- [90] M. Klein. “Optics Calculations and Simulations of Longitudinal Beam Dynamics for the Low-alpha Mode at ANKA”. PhD thesis. Karlsruhe Institute of Technology, 2012.
- [91] M. Streichert et al. “Simulations of Fringe Fields and Multipoles for the ANKA Storage Ring Bending Magnets”. In: *Proceedings of IPAC’2012*. 2012, pp. 1626–1628.
- [92] J. Safranek et al. “Matlab-based LOCO”. In: *Proceedings of EPAC’02*. Vol. 2. 2002, pp. 1184–1186.
- [93] F. Zimmermann. “Measurement and correction of accelerator optics”. In: *Beam Measurement*. World Scientific, 1999, pp. 21–107.
- [94] J. Wenninger. “Lattice Measurements”. In: *CAS - CERN Accelerator School: Course on Beam Diagnostics, 28 May - 6 Jun 2008*. CERN, 2009, pp. 369–375. DOI: 10.5170/CERN-2009-005.361.
- [95] P. B. Wilson et al. “Bunch lengthening and related effects in SPEAR II”. In: *IEEE Trans. Nucl. Sci.* 24.LBL-6163 (1977), pp. 1211–1214.
- [96] *atmatch function in AT*. [Online; accessed 2018-03-17]. URL: <http://atcollab.sourceforge.net/atdocs/manuals/user/ATMATCH.pdf>.
- [97] B. Nash and N. Carmignani. *Quantum Diffusion Element in AT*. [Online; accessed 2018-02-14]. URL: <http://atcollab.sourceforge.net/atdocs/manuals/physics/qdifElemAT.pdf>.
- [98] W. Herr. “Introduction to Landau Damping”. In: *CAS - CERN Accelerator School: Advanced Accelerator Physics, 18-29 Aug 2013*. 2014, pp. 377–403. DOI: 10.5170/CERN-2014-009.377.
- [99] Advanced Compound Semiconductor Technologies (ACST) GmbH. *UWB Quasi-optical Detectors up to 2 THz*.
- [100] B. Kehrer et al. “Simultaneous detection of longitudinal and transverse bunch signals at a storage ring”. In: *Phys. Rev. Accel. Beams* 21 (10 2018), p. 102803. DOI: 10.1103/PhysRevAccelBeams.21.102803.
- [101] T. Boltz. “Comprehensive Analysis of Micro-Structure Dynamics in Longitudinal Electron Bunch Profiles”. Master thesis. Karlsruhe Institute of Technology, 2017. DOI: 10.5445/IR/1000068253.

-
- [102] Virginia Diodes, Inc.
- [103] J. T. VanderPlas. *Understanding the Lomb-Scargle Periodogram*. 2017. arXiv: 1703.09824.
- [104] A.-S. Müller et al. “Studies of current dependent effects at ANKA”. In: *Proceedings of EPAC’04*. 2004, pp. 2011–2013.
- [105] T. Bückle. “Bestimmung der Strahlenergie des ANKA-Speicherring mittels resonanter Elektron-Spin-Depolarisation”. Diploma thesis. Universität Karlsruhe (TH), 2008. eprint: <http://nbn-resolving.org/urn:nbn:de:swb:90-220441>.
- [106] M. Brosi et al. “Systematic studies of short bunch-length bursting at ANKA”. In: *Proceedings of IPAC’16*. JACoW, 2016. DOI: doi:10.18429/JACoW-IPAC2016-TUPOR006.
- [107] S. Cova et al. “Avalanche photodiodes and quenching circuits for single-photon detection”. In: *Applied optics* 35.12 (1996), pp. 1956–1976. DOI: 10.1364/AO.35.001956.
- [108] *NumPy*. [Online; accessed 2019-06-27]. 2006–. URL: <http://www.numpy.org/>.

Acknowledgements

This chapter is intended just to say Thank You to many people being involved in my work during the last years. At the end, it was me sitting at the computer and writing page by page. But this was the only part I did alone, as all results discussed and presented here would not have been possible without so many people. As they are so many, I grouped this chapter into sections. It is noteworthy that the order of sections has nothing to do with the individual importance. In addition, I will switch back to German at this place.

KIT

Zunächst gilt mein Dank Prof. Anke-Susanne Müller, Prof. Marc Weber und Dr. Erik Bründermann, die in wissenschaftlicher, administrativer, finanzieller und natürlich persönlicher Hinsicht für die guten Randbedingungen in Zusammenspiel mit den hierfür nötigen Freiheitsgraden gesorgt haben, die das Erstellen der nun vorliegenden Arbeit ermöglicht haben.

Ein großes Dankeschön gilt den Kollegen der THz-Gruppe (auch wenn es sie *offiziell* nicht mehr gibt, in unseren Herzen lebt sie weiter...). Ohne die von und mit euch geschaffene Atmosphäre wäre all' dies nicht möglich gewesen. Ganz besonders danken möchte ich Edmund Blomley, Tobias Boltz, Miriam Brosi, Julian Gethmann, Thiemo Schmelzer, Patrik Schönfeldt, Patrick Schreiber und Johannes Steinmann, die nicht nur das Doktorandenschicksal mit mir geteilt haben, sondern die auch stets ein offenes Ohr für die verschiedenen Probleme und Fragestellungen des (wissenschaftlichen) Alltags hatten. Auch wenn sie dem KIT mittlerweile leider den Rücken gekehrt haben, so müssen an dieser Stelle Nicole Hiller, Manuel Schedler und Paul Schütze erwähnt werden. Ohne den unermüdlichen Einsatz von Paul wäre der FGC-Aufbau nie zu dem geworden, was er jetzt ist und auch die Operateurskünste von Manuel Schedler haben das ihrige dazu beigetragen. Darüber hinaus verdanke ich ihm die vielleicht schönsten *Veröffentlichungen* der letzten Jahre^{1,2} und ganz wunderbare Erinnerungen an eine – nicht nur in wissenschaftlicher Hinsicht – ausgesprochen produktive Zeit. Überhaupt gilt ein großes Dankeschön den Operateuren während der Messzeiten. Nicht vergessen möchte ich auch Sebastian Marsching, vor Johannes und Paul mein erster Büronachbar

¹Wilhelm Linac, Peer Review, Igor Pro et al., “Der Beschleuniger”, 2015.

²Wilhelm Linac, Peer Review, Igor Pro et al., “Der Beschleuniger”, 2016.

am KIT. Seither weiß ich: *Komisch, kaum macht man's richtig, schon geht's!* Ebenfalls zu danken habe ich Lorenzo Rota für die hervorragende Zusammenarbeit auf dem kurzen Dienstweg zwischen ANKA, pardon KARA und dem IPE: If I think about our mounting skills with KALYPSO at the visible light diagnostics (VLD) port, we should get a master's degree – or at least a bachelor's degree – in mechanical engineering....

Um am KIT zu bleiben, so muss an dieser Stelle auch einmal allen Mitarbeitern der Kantine des Campus Nord ein Lob und Dank ausgesprochen werden. Sie haben uns jeden Tag auf's Neue mehr als nur satt gemacht und so war der allmorgliche Gang zur Kantine eine feste Instanz im Tagesablauf. Ebenfalls erwähnen möchte ich – stellvertretend für alle Fahrer des KIT-Shuttles – Manfred Blau, der uns bei Wind und Wetter stets sicher zwischen Campus Nord und Süd befördert hat, auch wenn sich die moderne Technik ab und an eine Auszeit genehmigt hat. Manfred, die Fahrten mit dir waren stets ein angenehmer Ausklang eines Arbeitstages, bisweilen aber auch der Auftakt zu einer längeren Nachtschicht!

Familie

Ein riesengroßes Dankeschön gilt meinen Eltern, die mich persönlich und finanziell über manche Untiefe hinweg begleitet haben und mir dadurch nicht zuletzt all' dies ermöglicht haben.

Hier anschließen möchte ich meinen Dank an Maximiliane und Jörg mit Cornelius, Friederike und Henriette. Auch wenn es nicht oft der Fall war, aber bisweilen war das "Garage bauen" mit Duplo-Steinen oder eine Runde "Wimmelbuch-Gucken" (*Wo ist Niko?*) eine willkommene Abwechslung vom Schreiben des nun vorliegenden Werkes.

Juliane Becker

Juliane hat mich – einem Marathonengel gleich – auf der Zielgerade dieser Dissertation begleitet und mir wunderschöne Momente geschenkt. Momente, von denen ich bis dahin nicht zu träumen gewagt hatte und bei denen es mir nach wie vor schwer fällt, sie angemessen in Worte zu fassen.

Juliane, Dich an meiner Seite zu wissen ist ein kostbares Privileg, dessen ich mich glücklich schätze und für das ich tiefe Dankbarkeit empfinde. Es ist wunderschön, Dich als Freundin zu haben und mit Dir durch's Leben zu gehen!

Freunde

Neben den Kollegen und der Familie gibt es eine Gruppe, der ich ebenfalls besonders danken möchte, nämlich meinem Freundeskreis, wobei ich auch hier einige Vertreter dieser Zunft besonders hervorheben möchte:

- Christoph Mauch, der am Telefon und im persönlichen Gespräch stets ein offenes Ohr für mich hatte.
- Marco Röllig, der als Reise- und Joggingpartner für viele schöne Erinnerungen gesorgt hat, mir stets ein offenes Ohr lieh und nie um einen lockeren Spruch verlegen war.
P.S.: Die Idee mit dem Halbmarathon war genial, ebenso die, wieder mit dem Tanzen zu beginnen....
- Brigitte Schwab, für eine wunderbare Begegnung mit einem ebenso wunderbaren Menschen.
- Larissa Obert, die als Tanzpartnerin so manchen tänzerischen Fauxpas meinerseits aushalten musste, aber auch bisweilen als persönliche Trainerin (*Fordern und Fördern*) in Erscheinung trat und eine lange nicht mehr gespürte Leidenschaft in mir geweckt hat. Tanzen :).
- Ursula Kritzler, die als Tanzpartnerin ebenfalls manchen Fauxpas aushalten muss, als gute Seele mir gegenüber dabei nie die Zuversicht verliert und für grandiose Urlaubserinnerungen verantwortlich zeichnet.
- Carolin Geier, Sevilay Kiliç, Eduard Much, Nina Werner und Harald Wiegand, mit denen ich jeden Dienstag auf's Neue bisweilen hirnverknotende Figuren erlernen durfte und die hierbei stets für die nötige entspannte Atmosphäre gesorgt haben.
- Johannes Gesk, Felix Hahl, Florian Hotz und Nicole Röhrig, den besten Mitbewohnern, die man sich vorstellen kann.

Sonstige

In einem letzten Rundumschlag kommen nun all diejenigen zum Zuge, die nicht in o.g. Kategorien fallen und trotzdem einer Erwähnung wert sind. Ein dickes Dankeschön gilt Frau Dr. Estenfelder, den Frauen Feigenbutz, Reginald, Göke, Beeske und Zöllner sowie Herrn Segger, die mir wichtige Impulse gegeben haben, ohne die das vorliegende Werk vermutlich nicht entstanden wäre. Ein großer Dank gebührt auch den Mitarbeitern der Tanzschule Danceworld m/m, allen voran Carl-Heinz Mutschler-Morano mit seiner unvergleichlichen, charmant-witzigen Art. Ebenfalls gilt mein Dank allen Kaffeeröstereien dieser Welt, dem Restaurant Bruno's Pizza, dem Erfinder des Laufschuhs und des Halbmarathons. Ein großes Kompliment geht auch an den Erschaffer des Postillon³. Dieser diente uns als nie versiegender Quell der Heiterkeit und war Vorbild und Inspiration zugleich. Ohne ihn wäre **Der Betstjeniger** nie zustande gekommen. Ein großes Dankeschön geht zudem auch an die Mitarbeiterinnen und Mitarbeiter des "Copyshop an der Uni".

Last but not least danke ich Allen, die nett zu mir waren / sind / sein werden und mich so nehmen, wie ich bin.

³<http://www.der-postillon.com>

A. Appendix

A.1. Time-correlated single photon counting

A.1.1. Dead time determination

PicoHarp

For the determination of the dead time of the PicoHarp 300, the input channel normally used for the single photon avalanche diode (SPAD) is connected to a frequency generator that sends logical pulses with a certain frequency. If this frequency exceeds the inverse dead time $1/\tau_{d, PH}$, the count rate on the input channel drops to the half as half of the incoming trigger pulses now fall into the dead time and thus are not recorded.

In Fig. A.1 this measurement is illustrated by plotting the PicoHarp count rate over the input count rate from the frequency generator. By analysing the position of the two steps in the curve (at 11.5 1/s and 23.1 1/s) the dead time of the PicoHarp is determined to be $\tau_{d, PH}=86.8 \pm 0.2$ ns. This coincides with the data sheet value of <95 ns [59].

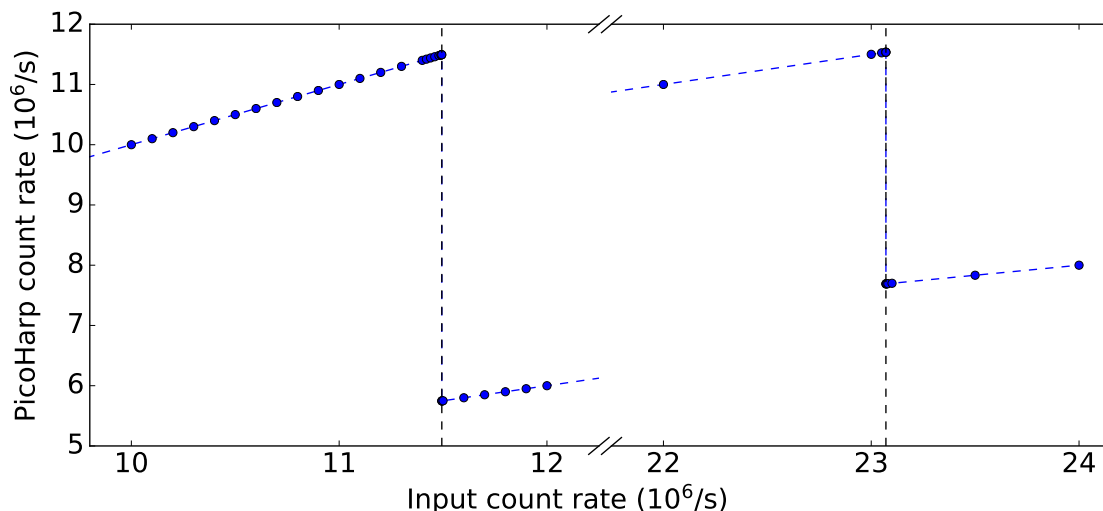


Figure A.1.: PicoHarp count rate over input count rate from a frequency generator. When the input count rate exceeds $1/\tau_{d, PH}$, the count rate drops as events starting to fall into the dead time reducing the measured count rate. The same repeats if the input count rate exceeds twice the inverse dead time.

Single photon avalanche diode

The SPAD used at the TCSPC-setup is an actively-quenched diode: When a single photon has triggered an avalanche process, the diode electronics detects this avalanche and reverts the polarity of the bias voltage to quench the avalanche process [107]. Otherwise, it will not stop and thus damage the diode. After the quench, the voltage is reversed again and the SPAD is able to detect the next incoming photon. This quenching and re-arming of the device takes a certain dead time τ_d , SPAD.

To determine this dead time, the diode is exposed to a high photon flux and the output of the diode (TTL pulses) is sampled by an oscilloscope. Using the infinite persistence mode of the oscilloscope allows an estimation of the dead time, this is illustrated in Fig. A.2. Thus, the dead time of the diode can be determined to 37 ± 1 ns. This is below the typical dead time from the manufacturers specifications [58] of 45 ns.

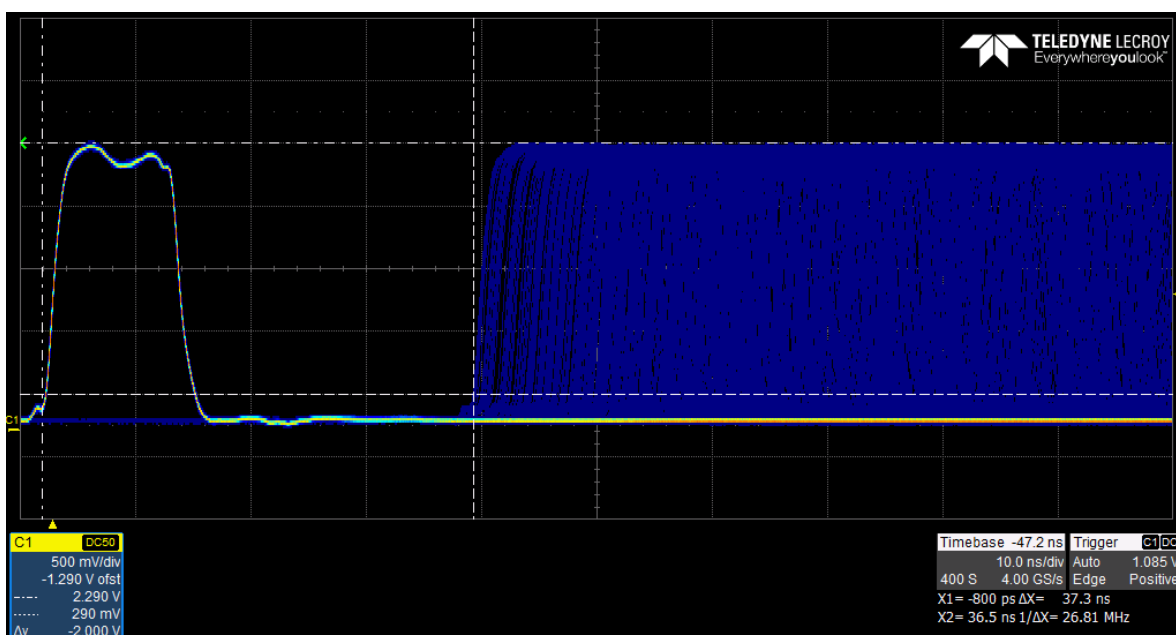


Figure A.2.: Screenshot of the oscilloscope sampling the TTL-pulses from the SPAD in infinite persistence mode. The minimum time between two pulses is determined to be 37 ns.

A.1.2. Estimation of the SPAD dead time effects

Both components of the TCSPC setup – the PicoHarp as well as the SPAD – have a dead time. As the dead time of the PicoHarp is more than a factor 2 above the one of the SPAD (86.8 ns compared to 37 ns), its dead time dominates. The overall dead time of the system is only extended by the SPAD dead time if a photon hits the SPAD during the last 37 ns of the PicoHarp dead time. To estimate the additional effect of this dead time, the histogramming process can be simulated. Therefore, a sequence of photon arrival times is created using pseudo-random numbers using the Python NumPy package [108].

As input, the filling pattern (184 values), the acquisition time T_{Acq} as well as the overall photon count rate are required. From these values, the total number of photons and the number of turns covered by the acquisition N are calculated.

The random sampling then consists of the following steps:

1. For each photon, the corresponding emission turn is determined from a uniform distribution between 0 and N .
2. For each photon, the emitting bunch is determined using a random generator with the filling pattern as underlying probability distribution.
3. Remove all duplicates (photons coming from the same bunch at the same turn).
4. Adding a jitter to each individual photon arrival time based on a normal distribution.

For the analysis, an iteration over all photon arrival times is done and for each photon is tested if it falls into a dead time triggered by the previous events. Events falling into the dead time are tagged and thus ignored for the histogramming. The result of this study is illustrated in Fig. A.3.

In the top panel, the three filling patterns are plotted. The blue curve is the reference filling pattern that also acts as user defined probability distribution for step 2. The red curve is the filling pattern for the case when only the PicoHarp dead time is taken into account while the green curve depicts the case where the SPAD dead time is taken into account as well. The center panel shows the difference between the reference and the filling patterns distorted by the PicoHarp or by both devices' dead times. The bottom panel shows the difference between the two curves from the center panel. While the difference between the reference filling pattern and the filling pattern only distorted by the PicoHarp is up to $\pm 40 \mu A$, the additional effect of the SPAD dead time is below $\pm 1.5 \mu A$ and thus more than one order of magnitude lower.

Therefore, only the PicoHarp dead time is taken into account for the correction.

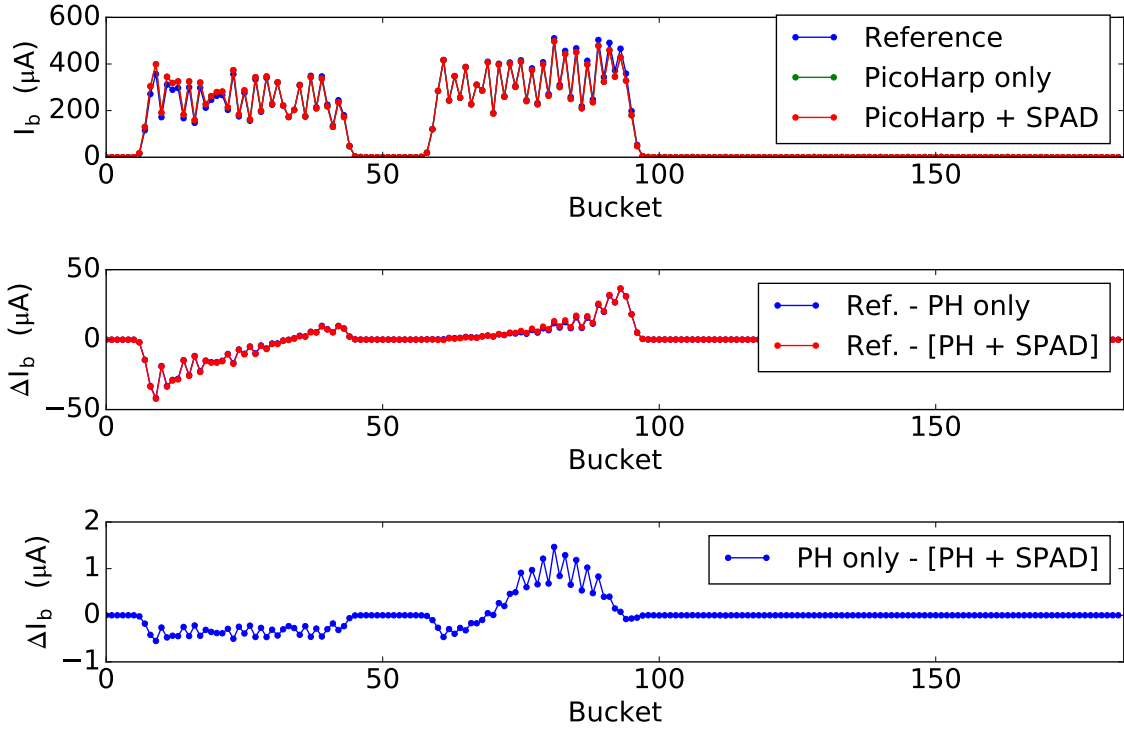


Figure A.3.: Estimation of the additional filling pattern distortion due to the SPAD dead time. The top panel shows the reference filling pattern and the two filling patterns where for the red curve only the PicoHarp dead time was taken into account while for the green curve also the SPAD dead time. The center panel shows the difference between the reference curve and the distorted filling patterns. The difference between the two distorted filling patterns is shown in the bottom panel.

A.2. Fast-gated camera: control and readout

A single FGC measurement consists of different steps. This is illustrated in the diagram in Fig. A.4

1. When a measurement is started from the control computer, the waveform generator calculates the corresponding voltage ramp for the mirror driver.
2. The waveform generator starts the voltage ramp, at the same time the CCD exposure starts.
3. When the mirror has reached the position where the light is reflected onto the sensor, the waveform generator sends a logical signal to the TLU (AND gate) to let the incoming trigger pulses from the EVR pass.
4. The trigger pulses passed by the TLU are sent to the camera to open the gate.

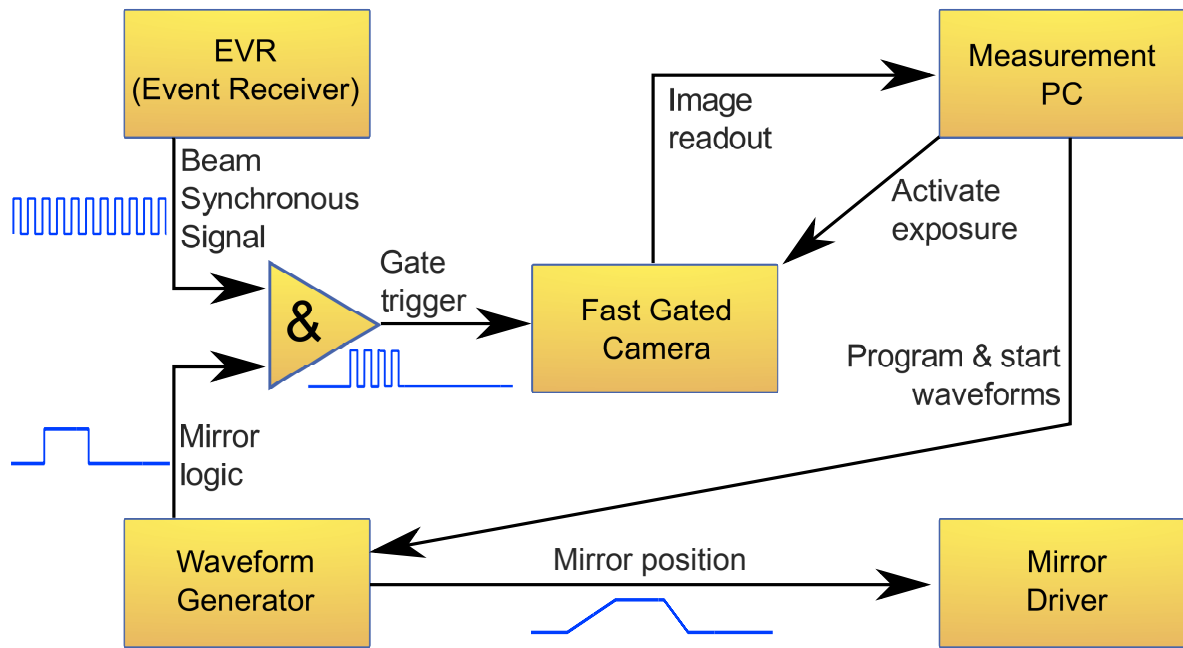


Figure A.4.: Control diagram for the FGC setup. The measurement is controlled using a PC that starts the waveform calculation in the waveform generator. It gives two signals: the first one is the voltage ramp for the mirror driver, the second one is the logical signal for the trigger logic unit (TLU). It is used to let the incoming gate trigger pulses from the event receiver (EVR) pass through (adapted from [71, Fig. 5.5]).

5. After the light has been swept over the sensor, the TLU stops passing the trigger pulses and the exposure stops.
6. The final image is read from the FGC.
7. The waveform generator drives the mirror back to the starting position.

A.3. Streak camera: data analysis

To get a measure for the position relative to the *fast* time axis of the streak camera (SC), a sum of two Gaussian curves – including an offset term to compensate the background level – is fitted to the individual data sets:

$$f(t) = c + A_1 \cdot \exp\left(-\frac{1}{2} \left(\frac{t - \tau_1}{\sigma_1}\right)^2\right) + A_2 \cdot \exp\left(-\frac{1}{2} \left(\frac{t - \tau_2}{\sigma_2}\right)^2\right). \quad (\text{A.1})$$

From the two arrival times τ_1 and τ_2 , the synchronous phase shift can be calculated [33, Eq. (6.9)]:

$$\Delta\phi = \tau_1 + \tau_2 - \tau_0. \quad (\text{A.2})$$

Here, an additional constant τ_0 is subtracted from the sum of the two times τ . This does not play a role for the loss factor studies, as only the slope of the curve is relevant. To determine the distribution of the beam current on the bunches, the offset value c is subtracted from the profile data and the integral over the peak regions is calculated.

This is illustrated in Fig. A.5. There, the top panel shows one SC raw image, where the horizontal and vertical pixel axis has been converted into time values. The bottom panel shows the projection of the image onto the horizontal or *fast* time-axis. For the errors, Poisson's statistics with $\sigma_i = \sqrt{n_i}$ is assumed. In addition, it shows that the shape of the average bunch profile deviates from a Gaussian for the main bunch (left peak).

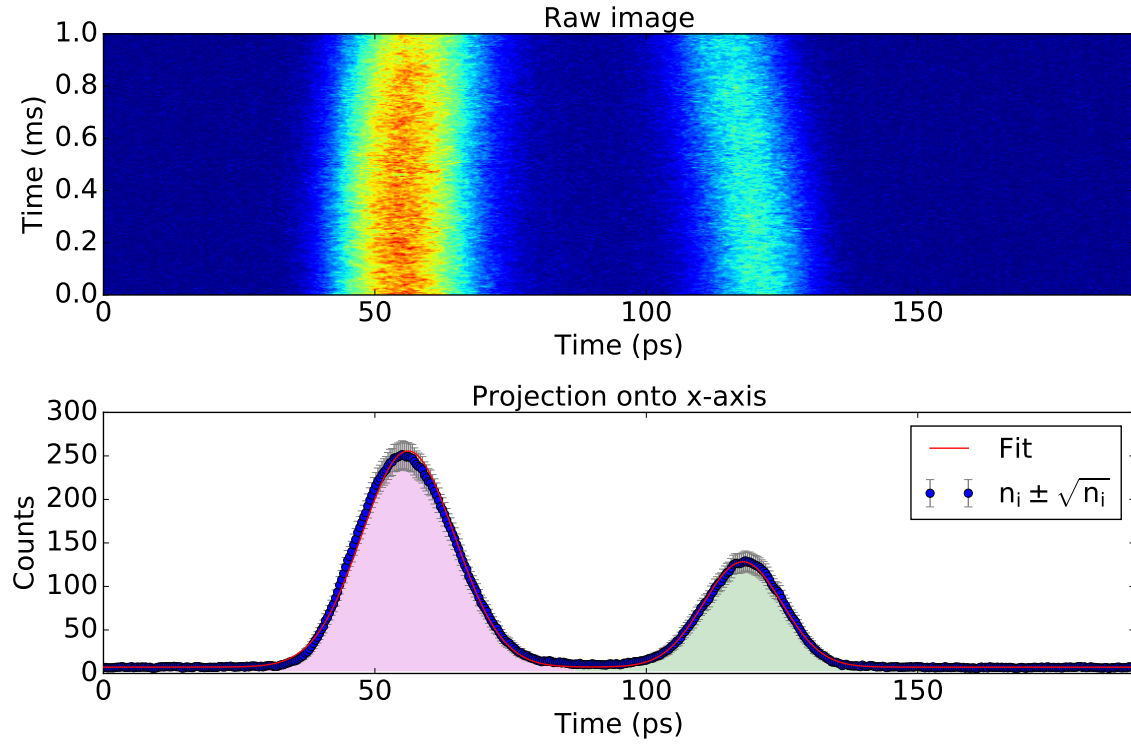


Figure A.5.: Raw image (top) and averaged longitudinal bunch profiles (bottom) recorded using a streak camera (SC). The left peak is the main bunch while the right one is from the reference bunch. The red line is a double Gaussian fit according to Eq. (A.1). The colored areas below the curve depict the integration range used for the determination of the current distribution on the bunches.

Das Leben ist wie eine
Avalanche-Diode:
Alle warten auf den Durchbruch.

*Life is like an avalanche diode:
Everybody is waiting for the
breakthrough.*